LBL-7668

C.2

MICROSTRUCTURE AND MAGNETIC PROPERTIES OF SPINODAL Fe-Cr-Co ALLOYS

Masuo Okada
(Ph. D. thesis)

May, 1978

Prepared for the U.S. Department of Energy
under Contract W-7405-ENG-48

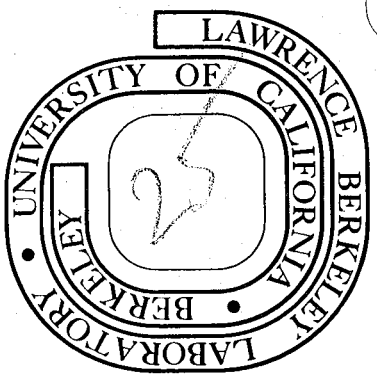

LBL-7668

C.2

Microstructure and Magnetic Properties of Spinodal Fe-Cr-Co Alloys

By

Masuo Okada

B.Eng. (Tohoku University, Sendai, Japan) 1971
M.S. (University of California) 1974
M.Eng. (Tohoku University, Sendai, Japan) 1975

DISSERTATION

Submitted in partial satisfaction of the requirements for the degree of

DOCTOR OF PHILOSOPHY

in

Engineering

in the

GRADUATE DIVISION

of the

UNIVERSITY OF CALIFORNIA, BERKELEY

Approved:

.....

.....

.....

Committee in Charge

.....

MICROSTRUCTURE AND MAGNETIC PROPERTIES OF SPINODAL Fe-Cr-Co ALLOYS

Contents

Work supported by the U. S. Department of Energy.

MICROSTRUCTURE AND MAGNETIC PROPERTIES OF SPINODAL Fe-Cr-Co ALLOYS

Masuo Okada

Materials and Molecular Research Division, Lawrence Berkeley Laboratory,
and Department of Materials Science and Mineral Engineering,
University of California, Berkeley, California 94720

ABSTRACT

The relationship between the microstructure and magnetic properties of spinodally decomposed Fe-Cr-Co ductile permanent magnet alloys has been investigated using transmission electron microscopy, electron diffraction, Lorentz microscopy, and magnetic analysis. Isothermal aging of three alloys (Fe-16 wt% Cr-28 wt% Co, Fe-31 wt% Cr-23 wt% Co, Cr-26 wt% Fe-13 wt% Co) located along the same conjugate tie-line inside a miscribility gap resulted in decomposition into two phases, an Fe-Co rich phase (α_1) and a Cr-rich phase (α_2). The microstructural features of the decomposed products were consistent with those expected from a spinodal reaction and agree with the asymmetry in shape of the reported miscibility gap in the Fe-Cr-Co system. An Fe-31 wt% Cr-23 wt% Co alloy was found to be best among the three alloys as a permanent magnet because of its excellent combination of good ductility and good magnetic properties.

Isothermal aging of this alloy did not lead to any enhancement in magnetic properties, due to its production of an undesirable microstructure. Aging at 640°C develops a magnetic chromium-rich phase, while aging at 600°C produces a non-magnetic chromium-rich phase dispersed within the Fe-Co rich phase. The observed variation of the coercive force during isothermal aging can be explained on the basis of a modified Kersten theory for domain wall pinning. The results

of a Lorentz microscopy study further support the pinning model in isothermally-aged alloys.

A combination of thermomagnetic treatment (TMT) and step-aging was found to improve the magnetic properties of this alloy, giving a desirable microstructure viz, elongated Fe-Co rich phase particles embedded in the paramagnetic phase. The TMT primarily influenced the remanence (Br) by elongating the Fe-Co particles along the direction of the applied magnetic field. An optimum TMT consisted of aging at 640^{o}C for 40 min to 1 hr in a magnetic field of 2 kOe. Alternatively, step-aging was found to principally affect the coercive force (Hc) of the alloy, by increasing the difference in composition between the two phases, while leaving the morphology of the microstructure unchanged. The Cr-rich phase, which is normally magnetic after TMT became non-magnetic after step-aging. The domain walls which were imaged by Lorentz microscopy in the step aged alloy were found to be imaginary walls of the interaction domains.

The experimental data on the step aged alloy was interpreted using fine particles theories (coherent rotation, fanning, or curling models) and the best fit was provided by the fanning model as the lowest magnetization mechanism. This agreement is probably due to the shape of the Fe-Co rich phase particles in the step-aged alloy. Finally, on the basis of these results, further developments of Fe-Cr-Co magnets are discussed.

1. INTRODUCTION

Newly developed Fe-Cr-Co alloys have great technological potential to replace the available ductile magnets (e.g., Fe-Co-V, Cu-Ni-Fe, Fe-Co-Mo alloys) and some of the Alnico alloys in the present permanent magnet market[1] (see Fig. 1). Because of their good ductility, Fe-Cr-Co alloys will provide an expanded application for high performance small magnet circuits, which are difficult to make of Alnico or Ferrite magnets.

The hard magnets can be described by four main parameters: saturation magnetization (4 Is); remanent induction (Br); coercive force (Hc) and energy product ((BH)max). The higher these values, the better are the magnets. Saturation magnetization (4πIs) is not influenced by the structure of a material, but the other three parameters are structure-sensitive properties. Therefore there is strong potential for controlling magnetic properties by controlling the microstructural features.

In general, magnetic materials containing domain boundaries are magnetized by the movement of domain boundaries in response to an applied field. One way to achieve the high coercive force desired in permanent magnets is to impede the motion of domain boundaries with inclusions or strain introduced in the lattice. Another approach, which can lead to much higher values of the coercive force, is to eliminate domain boundaries completely by subdividing the material into "single-domain" particles. These fine ferromagnetic particles can be achieved either by powder techniques or by utilizing phase transformations. The former technique is utilized in ESD (elongated

single domain) materials, Ba-Ferrite and some rare-earth cobalt magnets, while the latter is used for Cu-Ni-Fe, Alnico alloys, Pt-Co magnets, some of rare-earth cobalt magnets containing Cu and others. Among the candidate phase transformations, spinodal decomposition is ideal for developing fine ferromagnetic particles dispersed in a non-magnetic phase. Fortunately, many theoretical and experimental studies of spinodal decomposition have been undertaken,[3-5] and the reaction is fairly well understood. In fact many permanent magnets such as Cu-Ni-Fe,[6-9] Cu-Ni-Co[10-11] and Alnico alloys[12,13] have been shown to undergo spinodal decomposition. Likewise, ductile Fe-Cr-Co magnets have been designed by following the miscibility gap in the Fe-Cr binary system into Fe-Cr-Co ternary system.[1]

It is reported that the magnetic hardening of these Fe-Cr-Co alloys is associated with their modulated structures, consisting of the two phases, a Fe-Co rich (α_1) phase and a Cr-rich (α_2) phase. Therefore, in order to control the magnetic properties of the alloys, it is important to establish the correlations between the microstructures and their magnetic properties. However, a detailed metallographic investigation of the system has not yet been reported. The purpose of the present investigation is to monitor the microstructural changes in Fe-Cr-Co with various heat treatments, and to correlate those changes with magnetic properties. The microstructural features of interest, volume fraction of the two phases and wavelength of the composition variation, are followed by electron microscopy and diffraction. Compositional changes resulting from decomposition are determined by Curie temperature measurements.

In general, the observation of magnetic domains gives important information on the magnetization reversal process in these magnetic materials. For the present investigation, the magnetic domain structures associated with various microstructures have been examined by the powder method and by transmission Lorentz electron microscopy. On the basis of these results, the magnetic hardening mechanism of the alloys are discussed.

2. REVIEW OF Fe-Cr-Co ALLOYS

2.1. Historical Development of Fe-Cr-Co Permanent Magnets

Ductile permanent magnets based on the Fe-Cr-Co system were designed by Kaneko, Homma and Nakamura in 1971.[1] They investigated the magnetic properties of Fe-30~50 wt% Cr-10~30 wt% Co alloys. (Hereafter, all compositions quoted are in wt%.) Using cylindrical samples, 0.5 cm in diameter, the material was solution-treated at 1300°C and quenched into ice brine to retain a single α phase (bcc). After isothermal aging of the alloys, an Fe-40 Cr-23 Co alloy gave the best magnetic properties, viz Br = 7.4 kG, Hc = 650 Oe, (BH)max = 2.1 MGOe. The coercive force increased with increasing cobalt and chromium content. When an Fe-31 Cr-23 Co alloy was aged in a magnetic field of 4 kOe and followed by a step-aging sequence, the magnetic properties reached Br = 11.5 kG, Hc = 660 Oe and (BH)max = 4.1 MGOe. Addition of 3 wt% Mo to an Fe-30 Cr-25 Co alloy further increased the magnetic properties, Br = 11.5 kG, Hc = 780 Oe and (BH)max = 5.0 MGOe. These values are comparable to those of some of Alnico alloys, however, Fe-Cr-Co alloys containing Mo must be quenched from the solution-treatment temperature at a rate of over 250°C/sec in order to avoid the formation of γ or δ phase. Because of this critical cooling rate to obtain a single α phase (100°C/sec for Fe-31 Cr-23 Co alloy), the size of the magnets was also severely limited.

Alternatively, Kaneko, Homma, Nakamura and Miura[2] studied the magnetic properties of Fe-Cr-Co-Si alloys as a function of the additional silicon content. These Si alloys have a lower critical cooling rate, e.g., 10°C/sec for an Fe-28 Cr-23 Co-1 Si alloy, and show superior

magnetic properties, Br = 13 kG, Hc = 580 Oe and (BH)max = 5.3 MGOe. Kaneko, Homma, Nakamura, Hoshi[14] suggested an introduction of swaging between thermomagnetic treatment and step-aging in order to improve the properties. They achieved an energy product of about 7 MGOe with the Fe-28 Cr-23 Co-1 Si alloy swaged to 50% reduction in area. Higuchi, Kamiya and Suzuki[15] reported that the addition of silicon made the fabrication of these alloys easier, reducing the solution-treatment temperature. They found that an Fe-27.5 Cr-17.5 Co-1 Si alloy was most suitable for their manufacturing process, which consisted of: melting, casting, hot forging, softening, cold drawing, solution treating, field treating, swaging, and finishing. The energy product of samples from their products varies between 5.0 and 5.8 MGOe.

Wright and Johnson[16] studied the effect of nitrogen on the properties of Fe-29 32 Cr-23 Co alloys and found that the limiting N content to restore good magnetic properties should be below 0.01%. In particular, Ti additions (up to 0.5%) among the nitride forming elements (e.g., Al, Zr) were found to reduce the N content effectively. Song[17,18] studied the effect of rare earth (Y and Sm) addition to Fe-Cr-Co magnets and concluded that the addition of a small amount of Sm increases the coercive force of the alloys (e.g., Hc 950 Oe after aging at 580°C for 32 hr).

Kaneko, Homma, Fukunaga and Okada[19] furthermore show that the addition of α-forming elements broaden the α-phase region in Fe-Cr-15 Co system. Specifically, the simultaneous addition of 1% Nb and 1% Al to the system was found to extend the α-phase region to just above the miscibility gap. In this condition, the alloys can be solution

treated at any temperatures above the miscibility gap (e.g., at 900°C) and subsequently continuously-cooled to room temperature to produce optimum properties, and as Br = 13 kG, Hc = 520 Oe and (BH)max = 5 MGOe with an Fe-25 Cr-15 Co-1 Nb-1 Al alloy. The development of these alloys also made it possible to fabricate a large ingot during manufacturing; however, they were found to be excessively brittle in the as-cast state.

McCaig[20] studied the stability of Fe-22 31 Cr-22 25 Co alloys including some with additions of Ti, Mo, V or Si. It was shown that in general the coercivity falls slightly with increasing temperatures, but in Fe-30 Cr-23 Co containing Ti and V, the fall does not commence until the temperature has been raised to 100°C or higher. His results indicate that the Fe-Cr-Co magnets behave in similar fashion to those of the Alnico system and can, therefore, be used for applications requiring a low temperature coefficient and good performance at high temperatures. Miyamoto[21,22] investigated the magnetic aftereffect and reversal temperature coefficients of magnetic flux densities at various operating conditions on the demagnetization curves of Fe-Cr-Co alloys in comparison with those of Alnico alloys. He defined the magnitude of the aftereffect by the amount of specific loss in remanent induction during one decade of time (S_{10}), in taking the referece time as 10 sec after magnetizing. He found that the value of S_{10} for Fe-Cr-Co magnets was larger than that of the columnar Alnico 5 magnet. He also reported that the temperature coefficients of Fe-Cr-Co alloys show the strong dependence on their operating points and markedly decrease with decreasing permeance.

Kaneko, Homma and Minowa[23] developed Fe-Cr-Co-V-(Ti) alloys, which are ductile in the as-cast state, as the alternative magnets of Fe-Cr-Co-Nb-Al alloys. They found does addition of V to the Fe-Cr-15 Co system also extends the α-phase region as that of Nb and Al. Fe-Cr-Co-V alloys can be easily manufactured, giving properties such as Br = 13.2 kG, Hc = 540 Oe and (BH)max = 5 MGOe with an Fe-23 Cr-15 Co-5 V alloy. Kaneko, Homma, Okada, Ikuta and Nakamura[24] measured the magnetic properties of ⟨100⟩, ⟨110⟩ and ⟨111⟩ single crystals of an Fe-30 Cr-23 Co-1 Si alloy, and found that these properties were almost independent of the crystal orientation after step-aging. But introducing a swaging step between the thermomagnetic treatment and step-aging, a remarkable improvement in properties was observed. A ⟨100⟩ single crystal swaged to 70% reduction of area yielded the best properties, Br = 13 kG, Hc = 980 Oe and (BH)max ~ 8 MGOe, which are, the best magnetic properties achieved with Fe-Cr-Co magnets up to present. Recently, Chin, Plewes and Wonsiewics[25] in Bell Laboratories succeeded to replace Remalloy (Fe-Co-Mo) with Fe-Cr-Co alloys for telephone receiver applications. They developed two alloys, Fe-28 Cr-15 Co-1 Al-0.25 Zr and Fe-28 Cr-15 Co-1 Nb-0.25 Ti-0.25 Zr, suitable for facilitated fabrication, giving the properties, Br = 9.6 kG, Hc = 460 Oe, (BH)max = 1.9 MGOe and Br = 8.9 kG, Hc = 440 Oe, (BH)max = 1.8 MGOe, respectively.

In summary, Fig. 1 shows the demagnetized curves of Fe-Cr-Co ductile magnets in comparison with those of some of the available ductile magnets.

2.2. Phase Diagram of Fe-Cr-Co System

An investigation of the constitution of the Fe-Cr-Co system has been conducted by Köster,[26] Rideout et al.[27] and Koster and Hofmann.[28] Figure 2(a)-(c) show the isothermal sections at 1200°C, at 700°C and at 600°C, respectively, of an Fe-Cr-Co system according to Rideout et al.[27] and Köster et al.[28] Figure 2(a) exhibits two solid-solution fields, and γ (fcc) phase and γ (bcc) phase, and their relationships to the σ phase field extending from the Co-Cr binary system. The σ phase region further extends to link those in the binary Fe-Cr and Co-Cr systems, at 600°C as shown in Fig. 2(c). It is reported[28] that an invariant peritectoid reaction occurs at about 600°C: $\gamma + \sigma \rightleftharpoons \gamma + \varepsilon$ (ε = hexagonal allotrope of cobalt). Thus below the invariant temperature, there would be two three-phase regions, $\alpha + \gamma + \varepsilon$ and $\alpha + \varepsilon + \sigma$, in contrast to the $\alpha + \gamma + \sigma$ and $\gamma + \varepsilon + \sigma$ areas characteristic of higher temperatures.

However, no equilibrium sections of the diagram below 600°C were presented in the above mentioned work. An obvious omission is the effect of the miscibility gap in the Fe-Cr binary system proposed by Williams.[29]

A number of investigations[29-35] have reported that the binary Fe-Cr system exhibits a miscibility gap, within which a bcc phase (α) decomposes into two isomorphous phases, an iron-rich phase and a chromium rich phase, upon aging. The decomposition in Fe-Cr alloys has been extensively studied in relation to their 475°C embrittlement.[30-32] Imai et al.[33] first suggested that spinodal decomposition was the possible mode of decomposition for the Fe-Cr system, on the basis of magnetization and electromechanical measurements.

The possibility of spinodal decomposition was also suggested in the interpretation of electron microscopic results by Lagneborg,[34] and Vintaikin et al.[35] Mössbauer spectroscopy has also been applied to study the phase separation process in the Fe-Cr system.[36-39] Chandra and Schwartz concluded that spinodal decomposition occurred in an Fe-60 at.% Cr alloy, but nucleation and growth dominated in Fe-(12~30) at.% Cr alloys.

The investigations of the decomposition in Fe-Cr-Co alloys were initiated to follow the hardening response of the alloys in developing high strength maraging steels.[40] Coutsouradis et al.[41] suggested that the hardening of Fe-13 Cr-(10~20) Co alloys was due to the formation of intermediate phases, and that the decomposition sequence of the alloys is formation of chromium-rich zones → intermediate precipitate → stable precipitate (σ phase). Abson and Whiteman[42] found that the precipitate at peak hardness appeared as finely distributed spheroids with a bcc structure in an Fe-20 Cr-15 Co alloy. Kaneko et al.[1] first suggested that the Fe-31 Cr-23 Co alloy shows modulated structures consisting of an Fe-Co rich phase (α_1) and a Cr-rich phase (α_2), which result from spinodal decomposition. However, the nature of the miscibility gap in the Fe-Cr-Co system was not clarified in these early studies.

Recently, Kaneko, Homma, Thomas et al.[43] determined the miscibility gap in an Fe-Cr-Co ternary system, using mechanical hardness and Curie temperature measurements. Their results are illustrated in Fig. 3. Figure 3(a) shows the miscibility gap of an α phase in Fe-Cr-Co system, denoting the decomposed conjugate lines as A, B, C and D. Figure 3(b)

exhibits the vertical sections along these conjugated lines, with the miscibility gap in an Fe-Cr system for comparison. It was concluded that the miscibility gap of the Fe-Cr binary system persisted within the Fe-Cr-Co ternary system, and that the addition of cobalt raised the decomposition temperature, and extended the difference in composition between the Fe-rich phase and the Cr-rich phase. Notably the α phase of the Fe-31 Cr-23 Co alloy decomposes into the Fe-Co rich phase with Fe-32 Co-3 Cr composition and the Cr-rich phase with a Cr-21 Fe-10 Co composition during aging at 600^{o}C.

3. EXPERIMENTAL PROCEDURES

3.1. Materials Fabrication and Treatment

The three alloys chosen for this study have compositions on the same conjugate line denoted by B in Fig. 3(a). These alloys, Fe-31 Cr-23 Co, Fe-16 Cr-28 Co and Cr-26 Fe-13 Co, are indicated in the vertical section of the miscibility gap along the conjugate line B as shown in Fig. 4. The primary interest of the present research was placed on an Fe-31 Cr-23 Co alloy (Alloy B in Fig. 4) because of its excellent combinations of good ductility and good magnetic properties (poor magnetic properties were observed for Fe-16 Cr-28 Co (Alloy A) and brittleness for Cr-26 Fe-13 Co (Alloy C)). Alloys of the nominal composition were prepared from 99.9% electrolytic iron, 99.9% electrolytic chromium and 99.9% cobalt by arc melting in helium atmosphere and were chill cast into a copper mold, 0.75 in. in diameter. They were then sealed in evacuated quartz tubes, back filld with Ar and homogenized for 1 day at 1300°C and quenched into water.

Specimens of ~0.5 mm thickness were cut for metallographic examination. Some of the ingots (Alloys A and B), 0.75 in. in diameter, were swaged to a diameter of 5 6 mm for magnetic measurements. Because of the brittle nature of alloy C, samples for magnetic measurement were prepared by casting into a copper mold, 0.25 in. in diameter. Small pieces, 3 cm long, were cut from these ingots. All these specimens for metallographic and magnetic measurement were further solution-treated at 1300°C for 30 min under argon atmosphere in a vertical resistance furnace. They were then quenched from 1300°C into iced brine at a rate of over 100°C/sec, which was particularly necessary for alloy B to

avoid γ or α phase formation. Chemical analyses done on randomly chosen slices and small pieces of ingots after the solution-treatment are shown in Table I.

The alloys were aged at 580°C 680°C for 3 min for ~100 hr in a neutral salt bath or for ~500 hr in a muffle furnace, and quenched into iced brine. Furnace temperature was monitored with a chromel-alumel thermocouple in the specimen zone; the maximum variation was found to be $\pm$4°C over the entire aging period. Since it is reported[1] that both thermomagnetic treatments and step-aging improve the magnetic properties of the alloys, the alloy B (31 Cr-23 Co) was also aged at 640°C in a magnetic field of 2 kOe, followed by step-aging.

3.2. Magnetic Measurements

The composition amplitudes were deduced by measuring the Curie temperature of the decomposed Cr-rich phase (α_2).[9,43] Since the Curie temperature of the α_1 phase is approximately 900°C,[32] measurements well below 900°C can be directly related to the composition of the α_2 phase. The magnetization as a function of temperature was measured with a magnetic balance (Shimazu) while the specimen, weight of 0.05~0.20 g, was heated at a rate of 10°C/min from room temperature to around 700°C, but at a rate of about 5°C/min from liquid nitrogen temperature to room temperature.

The demagnetization curves of the samples, 5~6 mmϕ x 3 cm, were measured with an automatic fluxmeter. Principles and apparatus of the magnetic measurement are well described in text books.[45-48] In the present investigations, Hc (coercive force), 4πIs (saturation

magnetization), Br (remanent induction) and (BH)max (energy product) were the parameters measured.

3.3. Specimen Preparation--Microscopy

3.3.1. Light Optical Microscopy

Optical metallographic specimens (19 mmϕ x 0.5 mm) were mounted in coldmount and polished, and then swabbed with Kallings etchant of the following composition.

5.0	gm	Cupric Chloride
100	ml	HCl
100	ml	Methyl Alcohol
100	ml	H_2O

All light optical metallographic work was performed on a Zeiss Ultrophot II optical microscope using polarized illumination.

3.3.2. Transmission Electron Microcopy

Specimens for electron microscopy were electro-chemically thinned to 5~7 mils thick in a solution of 23% perchloric acid and 77% acetic acid, followed by light grinding on 600 grit paper. Thickness before electropolishing was 3~5 mils. Disc specimens, 3.0 mm in diameter, were spark eroded from the thinned sheet, followed by thinning in an automatic jet polisher using the electrolytic solution described above. The optimal thinning condition was at 10 V and 38~40 mA. The specimens were examined in a Philips EM 301 electron microscope operated at 100 kV.

The interparticle spacings or wavelengths (λ) of the aged alloys were generally measured directly along a ⟨100⟩ direction on enlarged prints of micrographs taken in ⟨hko⟩ orientation. However, the

interparticle spacings, particle diameters and lengths in the thermomagnetically-treated alloys were measured along or normal to the direction of the applied magnetic field.

In most cases, the values and their standard deviation were calculated from a total of about 50 measurements taken from at least three different areas. Values of wavelength was also obtained from measurement of side band spacings along 100 in the diffraction pattern, using a modified Daniel-Lipson relationship.[49]

$$\lambda = \frac{h \cdot a \cdot r}{(h^2 + k^2 + \ell^2)\ \Delta r}$$

where r and r are distance from the 000 to the hkℓ reflection and satellites. Values for wavelength obtained by this method are most accurate since these results do not depend on knowledge of the magnification. However side bands were only measurable when λ was less than ~300Å.

3.3.3. Scanning Electron Microscopy

The fracture surface was investigated with an AMR 1000 scanning electron microscope operated at 20 kV.

3.4. Laser Optical Diffraction

The optical diffraction method has a number of advantages over normal metallographic examination. It provides easy detection of the presence of symmetries of objects,[50] and also enables a quite accurate determination of their mean spacings. The technique is equally valid for small or large area examination.

Laser-optical diffraction has been used currently to complement high resolution electron micrographs, of biological[51] or metallurgical

materials.[52] The method was extended in the present study to evaluate the wavelength of the decomposed alloys and the degree of elongation of the particles along the direction of the applied magnetic field during thermomagnetic-treatment. Optical diffraction patterns were obtained using a standard optical diffractometer (e.g., see Ref. 53) with a He-Ne laser illumination source ($\lambda \sim 6328$Å). Electron micrograph negatives were directly mounted in the ray path at normal incidence, in the same manner as that for standard optical gratings. The diffraction effects were calibrated by the ones taken from lattice images of evaporated Au films (a = 2.5Å) or of a 12H polytype in magnesium-sialons (a = 16.03Å).

3.5. Observations of Magnetic Domains

3.5.1. Powder Method

In the powder method[54] a drop of colloidal suspension containing fine ferromagnetic particles is applied to the polished surface of the specimen. The fine ferromagnetic particles are attracted to regions of high magnetic field gradient, revealing the pattern of magnetic structures. Careful specimen preparation is required for this investigation since the strains left in the surface after mechanical polishing yields nothing of the true domain structures, so-called "maze pattern."[55] In the present investigation, the surface of the specimen was first mechanically polished and then electrolytically polished in a solution of the 23% perchloric acid, and 77% CH_3COOH, in order to remove the strained layer produced by the mechanical polishing.

The colloidal magnetic suspension was prepared by Chikazumi's method,[55] which involves first dissolving 2 g of $FeCl_2 \cdot 4H_2O$ and 5.4 g of $FeCl_3 \cdot 6H_2O$ in 300 cc of water while maintaining the solution at 30 40°C, then slowly adding a solution of NaOH (5 g in water at 50°C) with vigorous stirring, resulting in precipitation of black magnetite (Fe_3O_4). The precipitate is then filtered out and washed several times with water. The purpose of these procedures is to remove the Na^+ and Cl^- ions completely from the deposition, where any trace of Cl^- ion can be detected by using silver nitrate solution. The final suspension is then made by ultrasonically stirring 1 cc of precipitate in about 30 cc of a 0.3% soap solution which contains no sodium chloride. A drop of the suspension is then placed on the polished strain-free surface of the specimen, and covered with a thin microscope glass to spread out the suspension into a uniform film. The specimen was examined with a Zeiss Ultraphot II optical microscope.

3.5.2. Transmission Lorentz Microscopy

To observe the magnetic domain boundaries by transmission electron microscopy, there are two approaches, both of which aim at reducing the magnetic saturation of specimen. One is switching off the objective lens, the other is raising the position of the specimen by using a special holder. The detail techniques have been treated in articles by Hirsh et al.[56] and Jackubovics.[57]

In the present investigation, a special specimen holder was designed to raise the position of specimen by 3 cm in a Hitachi HU-125. A JEM 7A microscope was also used since it sometimes imaged the domain walls at normal operating conditions.

4. EXPERIMENTAL RESULTS

4.1. Microstructural Characterization

4.1.1. The As-Quenched Alloys

Two types of microstructure have been observed in quenched Fe-Cr-Co alloys; those containing martensite (Alloy A) and those containing a bcc α single phase (Alloys B and C). The difference in quenched structures can be understood from the phase diagram shown in Fig. 2. The solution treatment was done in the γ phase field for Alloy A, and in the α phase field for Alloys B and C.

Figure 5 shows the typical morphology of the martensite in the as-quenched Alloy A. The observed lath martensites are mostly dislocated, which is consistent with that of Fe-13 Cr-10 20 Co alloys reported by Coutsouradis et al.[41] However, the noticable feature of the martensite laths in this alloy is that they are mostly twin-related. (Example: $(1\bar{1}2)$ is twin plane in Fig. 5). Some areas are found to contain the ε (hcp) phase, which is most likely formed martensitically upon quenching. However, no retained γ phase was detected. Transformation temperatures of the Alloy A followed by the dilatometer analysis were: Ms~200°C, Mf~130°C, As~700°C, Af~723°C.

Some of the as-quenched Alloy B specimens were observed to contain a small amount of the σ phase as shown in Fig. 6. The σ phase exhibits different morphologies (e.g., globular in Fig. 6, Widdmanstätten shape etc), formed at gain boundaries or within α grains in the as-quenched state. The various morphologies of the σ phase are reported to arise from the different cooling rate upon quenching.[58] Figure 7 summarizes

their results, showing the phase relations vs cooling rates. A Widmanstätten shape of the σ phase was formed when the alloy was quenched at a rate of 60°C/sec, but at the slower cooling rate which allows more time for diffusion, the globular shape of the σ phase is observed. The critical cooling rate to obtain an α single phase is 100°C/sec. Since the σ phase is an equilibrium constituent of the alloy at temperatures between 600°C~1100°C, it is stable upon aging at above 600°C. Thus in order to examine the intrinsic properties of the alloy, the alloy must be quenched at a rate of over 100°C/sec from 1300°C. This obviously introduces constraints on the size of the specimen for the present investigations.

4.1.2. Isothermally-Aged Alloys

A. Fe-31 Cr-23 Co

A-1. General Features of Microstructure. The series of bright field micrographs shown in Fig. 8 were taken from the alloy aged for 1 hr at 680°C, 670°C, 660°C, and 650°C, respectively. The contrast which allows the two phases microstructure to be distinguished results mainly from the differences in thickness and relative absorption between the Fe-Co rich (α_1) and Cr rich (α_2) phases, in view of the small difference in structure factors between the two phases. The α_1 phase is preferentially thinned during electropolishing and appears as the lighter colored regions (e.g., Figs. 8, 9 and 11 etc). That these are the α_1 regions is confirmed by comparison to Fig. 23 taken from Alloy A in which the α_1 phase is the major one and to Fig. 31 taken from Alloy C in which the α_1 phase is the minor one. These micrographs reveal that the miscibility gap of the alloy is below 680°C,

and also suggest that the morphology of the aged microstructures is very sensitive to the aging temperature, i.e., the α_1 phase has mostly spherical shape after aging at (b) 670°C, rod shape at (c) 660°C and interpenetrating rod shape at (d) 650°C.

The microstructures shown in Fig. 9 were obtained from the alloy aged at 640°C for (a) 3 min, (b) 20 min, (c) 2 hr and (d) 20 hr. The decomposition process of the alloy briefly aged inside the miscibility gap appears to be isotropic (see Fig. 9(a) and (b)), and is associated with halo-type diffuse satellites in the corresponding diffraction pattern as shown in Fig. 10. Figure 10(b), however, exhibits an intensity peak in the form of satellites along ⟨100⟩ directions, implying some tendency for the α_1 phase to be aligned in these directions. Note, however, that it is very difficult to detect this tendency from the corresponding bright field micrograph (Fig. 9(b)) alone. Prolonged aging produces more distinct alignment along ⟨100⟩ directions as shown in Fig. 9(c) and (d), and this causes peaking along ⟨100⟩ in the diffraction pattern of Fig. 10(c) and (d). In addition, Fig. 10 shows that the satellites spacing decreases with aging time as the modulation wavelength increases. This behavior is typical of spinodal coarsening.[9,59]

The micrographs shown in Fig. 11 are taken from the alloy aged at 600°C for (a) 20 min, (b) 2 hr, (c) 100 hr and (d) 500 hr. Figure 11 shows that the early stage of the decomposition process also occurs isotropically, and that a pronounced alignment of the phases occurs after long aging times (see Fig. 11(d)). The main difference in microstructures between Fig. 9 and Fig. 11 is that the

α_2 phase is the major phase in Fig. 9 and the minor one in Fig. 11. This can be understood from the asymmetry in shape of the miscibility gap in the Fe-Cr-Co system as shown in Fig. 4. As the aging temperature is changed, different tie lines are encountered and the volume fractions of the α_1 and α_2 phases change. In the present Alloy B, equal fractions of the two phases would be obtained by aging near 635°C. Thus small changes in aging temperature can produce large changes in microstructural distributions of the α_1 and α_2 phases.

Figure 12(a) shows a high resolution (110) lattice image taken from the alloy aged at 660°C for 1 hr (see Fig. 8(c)). The (110) fringes appear to be continuous across the interface between the α_1 and α_2 phases. The difference in lattice parameters of the two phase was detected by laser optical diffraction as shown in Fig. 12(b).[52] This experiment provides direct evidence that both phases are coherent.

A-2. Formation of the σ Phase. It was found that the formation of the equilibrium σ phase occurred at various stages of aging, inside and/or outside the miscibility gap. In general at higher temperatures the σ phase appears within a shorter time aging. The σ phase is similar to that reported in Fe-Cr or Cr-Co alloys,[60,61] having a tetragonal unit cell containing 30 atoms, with a = 8.75Å, c/a ratio$\simeq$ 0.52. Figure 13 shows examples of the observed diffraction patterns from a well developed σ phase region, in both (100) and (001) zones; the pattern suggests that the σ phase is ordered. The detailed scheme of ordering in the σ phase is presented by Bergman,[60] Dickens[62] and Hall.[63]

The morphology of the σ phase also varies with the aging condition. It was observed that the σ phase precipitated either along grain boundaries or inside grains. Figure 14 shows the formation of the equilibrium σ phase in the alloy after prolonged aging at 640°C for (a) 50 hr and (b) 100 hr. Relatively large plates or needles of the σ phase have precipitated inside the grain in Fig. 14(a). Further aging causes these plates to coalesce, resulting in a great amount of the σ phase with black contrast in Fig. 14(b) (note that the decomposed $\alpha_1 + \alpha_2$ phases are preferentially etched away). At lower temperatures the σ phase required longer aging times to appear. Figure 15 shows an example of the preferential formation of the σ phase along grain boundaries in Alloy B aged at 600°C for 500 hr. Note that colonies of the σ phase starting from the grain boundaries also grow into neighboring grains. This can be seen in the enlarged regions of (a) shown in Fig. 15(b) and (c). The σ phase has precipitated on nearly cubic planes of the matrix and has a tendency for preferential alignment along rows within a grain. These microstructural features were also observed in the alloy aged at higher temperatures for a short time, e.g., at 670°C for 1 hr, as shown in Fig. 16. Figure 16 reveals that the σ phase has aligned in a row inside the grain, with a plate like morphology, the edges of which are nearly parallel to the cubic directions.

Some of the specimens prepared from the 6 mmϕ ingot exhibit a Widmanstätten-type phase as shown in Fig. 17. This is believed to be formed during quenching after solution-treatment since this type of the σ phase was only observed in the specimen from the 6 mmϕ

ingot, some portion of which could not be quenched at a rate of over 100°C/sec. Widmanstätten σ phases are precipitated on cubic and [101] directions of the matrix in Fig. 17.

In the study, the crystallographic relationship between the phase and decomposed $\alpha_1 + \alpha_2$ matrix phases was not definitely determined, since most of the σ phases in the figures gave a few weak spots in the diffraction patterns. The plate-like σ phase appears mostly parallel to ⟨100⟩ or ⟨110⟩ directions of the matrix in early stage of its formation, but sometime grows to acicullar type upon further aging.

A-3. Variation of Wavelength. The kinetics of the growth of the wavelength were measured in the temperature range of 600°C to 640°C. The results are summarized in the logλ vs log$t$ in Fig. 18. The relationship between logλ and log$t$ can be expressed by $\lambda \propto Kt^n$. In the early stage of the growth of the wavelength, the values of n (the slopes of the lines in Fig. 18) vary with aging temperatures, i.e., 1/4, 1/5 and 1/20 at 640°C, 620°C and 600°C, respectively. But prolonged aging resulted in the same values of n = 1/3 at three aging temperatures. The plot of vs $t^{1/3}$ in Fig. 19 suggests that the relationship $\lambda \propto Kt^{1/3}$ is obeyed, and is consistent with the theories of coarsening presented by Lifshitz and Slyozov[64] and Wagner.[65] The rate constant (K) in the Lifshitz-Wagner equation is given by

$$K = \left(\frac{8\gamma D C_o V_m^2}{9RT}\right)^{1/3} \qquad (4.1.1)$$

where γ is the particle-matrix interfacial energy, D coefficient of diffusion of the solute in the matrix, Co solubility of solute in equilibrium with precipitate, Vm is the molar volume of the precipitate and RT has its usual meaning. Hence

$$K^3 \propto D \propto D_o \exp(-Q/RT) \tag{4.1.2}$$

$$\ln K = -\frac{Q}{R}\left(\frac{1}{T}\right) \tag{4.1.3}$$

The rate constant K is listed in Table II. A plot of $\log K^3$ vs 1/T shown in Fig. 20 gives an activation energy for the coarsening of the modulations, ~65 kcal/mole.

A-4. Variation of Composition. The compositional fluctuations were deduced by measuring the Curie temperature of the decomposed α_2 phase.

The magnetization as a function of temperature for the alloy aged at 640°C is illustrated in Fig. 21. The magnetization of the specimens in the as-quenched and aged state decreases with temperature up to approximately 400°C and then increases above 400°C and has a small peak. The magnetization curve is found to be reversible up to 400°C, but irreversible above 400°C, suggesting that the composition of the two phases does not change during heating up to 400°C.

In Fig. 21, the magnetization curve of the specimen B aged at 640°C for 20 min changes slope around 310°C, which is identified as the Curie temperature of the α_2 phase.[43] The longer the aging time, the sharper the discontinuity in the slope of this curve appears. The Curie temperature of the α_2 phase aged at various temperatures

as a function of aging time is summarized in Fig. 22. These results suggest: (1) that the decomposed phases reach their equilibrium composition within almost 2 hr; (2) that the α_2 phase developed during aging at 600°C is nonmagnetic at room temperature, but is magnetic after aging at 640°C. These results illustrate the sensitivity of the properties to aging temperature which suggest a dependence upon precipitate composition and morphology.

B. Fe-16 Cr-28 Co Alloy

B-1. Decomposition Products. Figure 23 shows the micrographs of the Alloy A aged at 640°C for (a) 20 min and (b) 20 hr. Upon aging, fine rod-like particle with black contrast homogeneously formed within martensite laths (diameter of the particle ~60Å in Fig. 23(a)). In the corresponding diffraction pattern, no extra spots due to these particles were observed, which indicates that they could be Cr-rich phase. The dark contrast of the Cr-rich phase is consistent with that observed in Alloy B. Prolonged aging leads to growth of the particles (diameter ~250Å in Fig. 23(b)) without loss of coherency.

Aging the alloy at 600°C also forms the same sort of Cr-rich particles. Figure 24 shows a series of micrographs of the alloy aged at 600°C for (a) 2 min, (b) 20 min, and (c) 200 hr. In Fig. 24(a), after aging only for 2 min the decomposition seemed to already take place homogeneously throughout the specimen, as revealed by the contrast of the modulated-like microstructure. The visibility of the Cr-rich particles is also seen to increase with increasing aging times (see Fig. 24(c)), and the formation of the Cr-rich particles

takes place homogeneously, in spite of the presence of dislocations or lath boundaries.

Similar observations of the Cr-rich phase has been reported in Fe-15 Cr-20 Co and Fe-13 Cr-(10 20) Co alloys by Abson.[42] Abson identified the finely distributed spheroids with a bcc structure and lattice parameter 2.86Å at 500°C and 2.88Å at 550°C.

B-2. Austenite Formation. During isothermal aging of the Alloy A, the phase transformations besides the formation of the Cr-rich phase occurs. Figure 25 shows the microstructures of the alloy aged at 640°C for (a) 40 min, (b) 5 hr, and (c) 20 hr, indicating that the volume fraction of the phase with dark contrast increases with increasing aging time. The dark phase is identified as the bcc lath martensite as shown in Figs. 16. Figures 26-27 are the transmission electron micrographs obtained from the Alloy A aged at 640°C for 20 hr, showing the heavily dislocated martensite surrounded by the decomposed matrix. The dark field images obtained by using a martensite reflection in selected area diffraction reversed the martensite contrast (Fig. 26(b)) The observed martensite laths are heavily dislocated and do not contain any products of decomposition; hence, they must form during quenching from the aging temperature. Particularly in Fig. 27 the dark phases near the edge of the foil are thin enough to clearly reveal their substructure, illustrating that there are no decomposed products in their interior. However, in the early stage of aging of the Alloy A, the ε phase (which has hcp structure found in the as-quenched state) does not undergo decomposition. This is shown in Fig. 28, which was obtained from the Alloy A aged at 640°C for 40 min. The bright field

image in Fig. 28(a) shows the decomposed matrix and retained ε phase, within which fine striations are seen parallel to the (011) direction of the matrix. In the corresponding diffraction pattern (Fig. 28(b)), streaks perpendicular to the striations in bright field are observed and the reflections of the ε phase split to 4H type as marked c.

Prolonged aging increases the volume fraction of the martensites as well as the width of the martensite lath. Figure 29 is taken from Alloy A aged at 640°C for 200 hr, and shows dislocated martensite of ~1.5 mm wide. The existence of a high dislocation density and the absence of any decomposition products in the lath martensite substantiate that a $\gamma \rightarrow$ martensite transformation occurs during quenching from the aging temperature to iced brine. Afterwards, prolonged aging appears to anneal out the dislocations and make the Cr-rich particles visible.

The occurrence of the $\gamma \rightarrow$ martensite transformation during quenching was confirmed by a dilatometer analysis. The as-quenched specimen was held at 640°C for 40 min, and then quenched in air. The transformation temperatures of the alloy aged at 640°C for 40 min were: Ms ~ 158°C; Mf ~ 60°C. These observations are consistent with that reported by Bungardt et al.[66] They show that the austenite formed in the Fe-19 Cr-15 Co steel during exposure for up to 1000 hr in the 450°C-700°C temperature range completely transforms to martensite on subsequent cooling.

In summary, the phase transformations in the Alloy A may be written:

$$\gamma_{fcc} \xrightarrow[\text{quenching}]{} \underset{\text{(martensite)}}{\alpha_{bcc} + \varepsilon_{hcp}} \xrightarrow[\text{aging}]{} \alpha_1 + \alpha_2 + \gamma_{fcc} + \varepsilon_{hcp}$$

$$\xrightarrow[\text{quenching}]{} \alpha_1 + \alpha_2 + \underset{\text{(martensite)}}{\alpha'_{bcc}} + \varepsilon_{hcp}$$

C. Cr-26 Fe-13 Co Alloy

C-1. General Features of Microstructure. The series of bright field micrographs shown in Fig. 30 were taken from the Alloy C aged for 20 hr at (a) 620°C, (b) 600°C and (c) 580°C, respectively. These micrographs reveal that the miscibility gap of the alloy is below 620°C, and that the rod-like α_1 phase with bright contrast is formed upon aging below 620°C. At lower aging temperatures finer α_1 particles appear. Upon further aging, the size of the α_1 particles increases as shown in Fig. 31, which was taken from the alloy aged for 200 hr at (a) 600°C and (b) 580°C. Aging at 600°C produces isolated rod-like α_1 particles of ~140Å diameter, the distribution of which appears to be crystallographically random. This implies that the decomposition process is isotropic in Alloy C. Aging at 580°C yields an interconnecting rod structure, the diameter of which is approximately 50Å. This illustrates the sensitivity of the morphology of the microstructures to the aging temperature.

C-2. Variation of Composition. The magnitude of the compositional fluctuations was deduced by measuring the Curie temperature of the decomposed α_2 phase as was done in Alloy B. The Curie temperature of the α_2 phase aged at 600°C as a function of aging time is summarized in Fig. 32, and suggests that the α_2 phase which develops during aging at 600°C is non-magnetic at room temperature.

4.1.3. Thermomagnetic Treatment

A. Microstructure

Thermomagnetic treatments play an important role in producing good magnetic properties. Figure 33 shows micrographs of the alloy

aged at 640°C for 20 min, 1 hr, and 3 hr in a magnetic field of 2 kOe and their corresponding laser optical diffraction patterns. The bright field micrograph parallel to the field direction, Fig. 33(a), shows that the α_1 phase is oriented almost randomly. However, the corresponding laser optical diffractogram of Fig. 33(a), reveals some tendency for the α_1 phase to be aligned along the direction marked M. The remanence in this state is nearly 0.6 I_S (I_S is the saturation magnetization).

Prolonged aging causes the α_1 phase to be more elongated parallel to the direction marked M, as shown in Fig. 33(b) and (c), and the corresponding laser optical diffraction patterns Fig. 37(b) and (c). The remanence after magnetic-aging for 1 hr increases up to almost 0.9 I_S, and remains unchanged after step-aging. The high remanence indicates that the ferromagnetic α_1 phase is elongated along the direction of an applied magnetic field, independent of crystal orientation.[67] This stems from the fact that the decomposition process is found to be isotropic during the early stage of aging for at least 1 hr. The independence of the magnetic properties on the crystal orientation is already confirmed by the measurements of magnetic properties of single crystals of the alloy. Figure 34 shows the microstructures, (a) parallel and (b) perpendicular to the magnetic field direction, of the alloy aged at 640°C for 40 min. The micrograph perpendicular to the field direction exhibits isotropic decomposition with a slight tendency for particle alignment along 100 directions. These figures illustrate that the Fe-Co rich phase is elongated along the field direction and has a rod-like shape.

When the thermomagnetic-aging time exceeds 2 hr, the remanence decreases to almost 0.8 I_s. This decrease can possibly be explained as follows. Under ideal circumstances, after prolonged aging in a magnetic field, the α_1 phase should normally maintain its alignment parallel with the applied field. However, the present observation suggests that in fact the α_1 phase cannot maintain this alignment in certain localized areas as marked M in Fig. 35. It is believed that in these areas particle alignment is highly affected by the elastic constraints of the matrix, since elastic strain energy minimization favors a ⟨100⟩ particle growth direction. Therefore the exact direction of alignment within these regions is determined by a balance between the applied magnetic field and elastic strain field of the matrix.

Further aging, in fact, increases the tendency for particle growth along ⟨100⟩ directions as shown in Fig. 36 (for 5 hr). This implies that the elastic strain field of the matrix exceeds the applied magnetic field, and decreases the efficiency of the thermomagnetic treatment. Therefore, the optimum time for the thermomagnetic treatment is limited from 40 min to 1 hr at 640°C.

B. Particle Growth

Variations of the morphological parameters of the Fe-Co rich particles as a function of thermomagnetic treatment time are ploted in Fig. 37. The particle length increases linearly with aging time, but the growth rate of its diameter becomes faster after 2 hr aging. Therefore, the ratio of particle length to diameter is maximized when the alloy is aged for 40 min to 1 hr. This is in support of the previous

results of microstructure observations, suggesting that 40 min to 1 hr is optimum time for the thermomagnetic treatment.

C. Optimum Condition

An optimum condition of the thermomagnetic treatment can be determined by considering the three parameters, aging temperature, aging time and applied magnetic field strength. For an Fe-31 Cr-23 Co alloy, 640°C was observed to be an optimum aging temperature since the formation of nonmagnetic σ phase occurred rapidly above that temperature. The field strength for the thermomagnetic treatment should also be over 2 kOe as shown in Fig. 38.[68] Therefore, an optimum thermomagnetic treatment for an Fe-31 Cr-23 Co alloy is such that aging is carried out at 640°C for 40 min 1 hr in a magnetic field of 2 kOe.

4.1.4. Step-Aging

A. Microstructures

It is reported that step-aging has a beneficial effect not only on improving the magnetic properties of Fe-Cr-Co alloys,[1] but also on improving the mechanical properties of Cu-Ni-Fe alloys.[69] Figure 39(a) shows a microstructure taken from the alloy aged at 640°C for 40 min in a magnetic field of 2 kOe. The ferromagnetic phase is somewhat elongated along the direction of the magnetic field and has an interpenetrating rod-like morphology. The rod diameter is about 100Å and average length, 280Å, giving a ratio of length to diameter of nearly 3.

Figure 39(b) shows the microstructure of the alloy given a thermomagnetic treatment at 640°C for 40 min and subsequently

step-aged at 620°C for 20 min and at 600°C for 1 hr. Throughout step-aging it is found that the ratio of length to diameter of the α_1 phase remains essentially unchanged (130Å in diameter, 370Å in length), and that the volume fraction of the α_1 phase increases slightly from 45% to 55%. The main change during step-aging is that of composition of the two phases, which is confirmed by the measurement of the Curie temperature of the α_2 phase of the step-aged alloy as shown in Fig. 40.[43] The α_2 phase is magnetic at room temperature just after the thermomagnetic treatment, but is becomes nonmagnetic after step-aging.

B. Secondary Decomposition

It should be emphasized that this step-aging method to produce the desired microstructure shown in Fig. 39 is valid only when the step-aging temperature interval ($\Delta T = T_{\text{step n}} - T_{\text{step n-1}}$) is small. When the alloy is aged at low temperatures after thermomagnetic treatment, secondary decomposition takes place as shown in Figs. 41 and 42. Figure 41 is a series of bright field micrographs taken from the alloy aged at 600°C for (a) 20 min, (b) 1 hr and (c) 3 hr after thermomagnetic treatment. Figure 41(a) clearly reveals fine particles (~25Å in diameter) homogeneously distributed over the modulated structure developed during thermomagnetic treatment. Further aging enhances particle size (see Fig. 41(b)), but also gives the peculiar morphology seen in Fig. 41. At the lower aging temperatures after the thermomagnetic treatment, the secondary decomposition product appear finer, as illustrated in Fig. 42, taken from the alloy aged at 580°C for (a) 20 min and (b) 1 hr after the thermomagnetic treatment.

4.2. Magnetic Properties

4.2.1. Isothermally Aged Alloy

A. Fe-16 Cr-28 Co Alloy

Magnetic properties of the isothermally aged A alloy are plotted in Fig. 43, indicating the saturation magnetization ($4\pi Is$) is higher at lower aging temperatures and ranges between 13~15 kG. It decreases monotonically with time during aging at 640°C and 620°C, but is almost constant during aging at 600°C and 580°C. The coercive force (Hc) does not vary much during aging, except at 640°C, when it initially increases to maximum value of ~150 Oe and then decreases. The maximum coercivity achieved by the isothermal aging of the Alloy A is ~150 Oe.

B. Fe-31 Cr-13 Co Alloy

Figure 44 shows the magnetic properties of isothermally aged Alloy B vs aging time, where typical values of the saturation magnetization are 12~14 kG. At lower aging temperatures, a higher saturation magnetization occurs. It should be noted that aging at 660°C or 640°C resulted in a remarkable decrease in the saturation magnetization. This decrease is due to the formation of the non-magnetic σ phase, as discussed earlier. The variation of the coercive force with aging time is such as to increase monotonically in the beginning and have a maximum value, and then decrease (except during aging at 580°C). The maximum coercive force achieved by the isothermal aging of the Alloy B is ~300 Oe; however, this value is achieved only after long aging times, e.g., 100 hr at 620°C or 200 hr at 600°C.

C. Cr-26 Fe-13 Co Alloy

Alloy C has a low saturation magnetization of order 3~5 kG as shown in Fig. 45. Nevertheless, the coercive force obtained by isothermal aging reaches 800~900 Oe in the alloy.

In summary, although a high saturation magnetization (13~15 kG) can be obtained with the Fe-rich Alloy A, its coercivity is low (50~150 Oe). Alternatively, a high coercive force (800~900 Oe) can be produced with the Cr-rich alloy, but its saturation magnetization is low (3~5 kG). Thus, optimum magnetic properties should be achieved with Alloy B, even though its coercive force achieved by isothermal aging is relatively low (~300 Oe), and requires long aging times to develop.

4.2.2. Thermomagnetic Treatment and Step-Aging

The magnetic properties of the Alloy B could be further improved, however by combined thermomagnetic treatment and step-aging.[1] The resulting magnetic properties after these treatments are summarized in Table III.

The main difference in magnetic properties between the alloy with and without the thermomagnetic treatment is the remanence, not the coercive force. The remanence of the alloy is fairly improved by aging in a magnetic field (compare No. 2 with No. 18 in Table III). The coercive force of the alloy increases remarkably after the first increment of step-aging at 620^{o} following the thermomagnetic treatment (see No. 6). It further increases after the second and third step-aging (se Nos. 16 and 17). It should be emphasized here that an alloy aged with or without a magnetic field, followed by step-aging exhibits

nearly the same coercive force, but does show a different remanence (compare No. 16 with No. 20). However, when the first step-aging is performed at low temperatures after thermomagnetic treatment (e.g., 580°C), the coercive force is not improved at all (see Nos. 13 and 15). Thus a carefully selected step-aging process is required to improve the magnetic properties. It is interesting to note that the alloy furnace-cooled from the thermomagnetic treatment temperature to the second step aging temperatures, followed by second step-aging, shows a fairly good coercive force compared to the alloy quenched from the thermomagnetic treatment to iced brine, followed by second step-aging (see Nos. 9 and 10, and Nos. 13 and 14). This indicates that the step-aging process can be altered by the proper continuous cooling scheme. The substitution of the step aging with continuous cooling has already been reported in modified Fe-Cr-Co magnets.[19,23,25]

In summary, typical magnetic hysteresis loops corresponding to different heat-treatments are shown in Fig. 46; A. 640°C, 2 hr, B. 600°C, 200 hr, C. 640°C, 40 min MT and D. step-aging. It can be concluded that while thermomagnetic treatment has an effect on improving mainly the remanence of the alloy, step-aging is significant in improving the coercive force.

4.3. Observations of Magnetic Domains

Studying the structures of the magnetic domains can give important information about the magnetization reversal process in these materials. In this section, special emphasis is placed upon studying how isothermal aging, thermomagnetic treatment and step-aging affect the structures of magnetic domains, utilizing both the Powder method and transmission Lorentz microscopy.

4.3.1. Powder Method

In the Powder method, fine particles of magnetic powder, spread on the surface of the specimen, are attracted to regions of high magnetic field gradient which are produced near domain boundary walls. Figure 47 shows the domain patterns of Alloy B aged, (a) at 640°C for 40 min, (b) at 620°C for 100 hr, and (c) at 600°C for 50 hr. The observed domain patterns are characteristic of a magnetically uniaxial ferromagnetic material (e.g., cobalt). These patterns indicate that the direction of domain magnetization differs in each grain. These directions are believed to be the ones of crystallographic easy magnetization.

However, the thermomagnetic treatment alters the direction of easy magnetization as shown in Fig. 48(a) (compare Fig. 47(a) with Fig. 48(a)). Figure 48 shows the powder patterns of the axial surfaces for 40 min in a magnetic field of 2 kOe (a), followed by step-aging (b) (heat treatment No. 17 in Table IV). This figure shows that the stripes are aligned near to the direction of the applied magnetic field. It indicates that the easy magnetization direction is close to the directionof an applied magnetic field, independent of crystal orientation. The contrast of the powder pattern in Fig. 48(b) is stronger than that in (a), suggesting that magnetic anisotropy parallel to the direction of an applied field, induced by the thermomagnetic treatment, becomes stronger by the step-aging treatment. Similar domain patterns are observed with an Fe-28 Cr-23 Co-1 Si alloy by Shur et al.[70]

4.3.2. Transmission Lorentz Electron Microscopy

The details of the domain structure were further observed by means of Lorentz electron microscopy. Figures 49(a) and (b) are the Fresnel micrographs (out-of-focus method) of the Alloy B aged at 640°C for 20 min, showing a 180° domain wall, and Figs. 49(c) and (d) are the Foucault micrographs (displaced aperture method) revealing magnetic domains. The domain wall appears to be straight, lying parallel to the ⟨100⟩ cubic directions. This stems from the fact that ⟨100⟩ directions are the ones of easy magnetization in Fe. This observation agrees with that of the power method in Fig. 51, viz. that domain walls lie preferentially along ⟨100⟩ directions in the grains. Figure 50 shows the magnetic domains ((a) and (b)) and domain walls ((c) and (d)) of the isothermally aged alloy at 600°C for 100 hr. The imaged domain walls in Fig. 50 are not straight but are locally wavy in contrast to those in Fig. 49. This may be ascribed to the difference in microstructures developed by aging at 640°C or 600°C. As discussed earlier, aging at 640°C produces the magnetic Cr-rich phase as a major phase, but aging at 600°C develops a nonmagnetic Cr-rich phase dispersed within the Fe-rich phase. Thus it is speculated that domain wall tends to lie within Cr-rich phase after aging at 640°C since the domain wall energy of the α_2 phase is lower than that of the α_1 phase. This was verified in the overaged Fe-Cr-Co-V alloy[71] by means of transmission Lorentz electron microscopy, which showed that the domain wall exists in the α_2 phase and is pinned by the α_1 phase. However, after aging at 600°C the domain walls must likely lie in the continuous α_1 phase and are

pinned by the non-magnetic α_2 phase. Therefore the reversal mechanism of both isothermally aged alloys B will be domain wall pinning.

Figure 51(b) shows the imaged domain walls ((a) and (b)) and the domains ((c) and (d)), on the axial surfaces of the step-aged alloy after thermomagnetic treatment. The observed domain walls are wavy and less sharp than those of the isothermally aged alloy. The domains are approximately 1~1.5 μm wide and are elongated in the direction of the applied magnetic field (see the morphology of the imaged microstructures in Figs. 51(c) and (d)). Figure 52 shows Foucault micrographs of the region near a grain boundary taken from the same step-aged alloy. The domain appears to be straight across the grain boundary, and elongated along the direction of an applied field. This domain feature is consistent with that observed by the powder method, and suggests that the magnetic anisotropy is introduced parallel to the direction of the applied magnetic field after thermomagnetic treatment and step-aging.

It should be emphasized that the nature of the imaged domain walls in step-aged alloy is different from that in isothermally aged alloy, since domain walls cannot lie within the non-magnetic α_2 phase after the step-aging process.

5. DISCUSSION

5.1. Mode and Kinetics of Decomposition

Alloys (A, B, C) with different compositions located along the same decompositional tie-line give different morphologies of microstructure upon aging (compare Fig. 11 with Figs. 24 and 31). Even Alloy B develops varied morphologies depending on the aging temperatures (see Figs. 8, 9 and 11). The structure resulting from spionodal decomposition is theoretically predicted by Cahn.[72,73] He found that a particular striking feature of this structure is the connectivity of the two phases which is expected when the volume fraction of the mirror phase exceeds about 15% $\pm$ 3%, whereas at volume fractions less than this, isolated aggregates of the minor phase should be formed (e.g., for Alloy A aged at 640°C and Alloy B aged at 600°C). Because of the asymmetry in the shape of the miscibility gap, the volume fraction of the two phases of the alloys varies depending on the aging temperatures. Alloy B shows a particularly striking change in the major phase upon aging above or below ~635°C, while aging of Alloys A and C at any temperature results consistently in the minor phase having a volume fraction of less than 20%, and an unchanged morphology. The change in morphology of Alloy B with aging temperature and the differences between Alloys A and C are thus a consequence of the change in the relative volume fraction of the two product phases. However, the microstructure of the Alloy B aged at 670°C and 660°C appears to show the α_1 phase embedded in the α_2 major phase rather than an idealized continuum, even though the volume fraction of the α_1 phase is more than 20%.

Lattice mismatch of the decomposed two phases (α_1 and α_2) appears to be small since no splitting of the high order reflections in the diffraction patterns were observed even after prolonged aging. The mismatch of the decomposed phases at 600°C is estimated to be 0.6%, assuming the idealized case where the decomposed α_1 and α_2 phases have the composition of Fe-33 wt% Co (a = 2.855Å) and Cr-32% Fe (a = 2.872Å),[74] based on the reported decompositional tie-line. As a matter of fact, Magat et al.[75] measured the lattice parameters of the decomposed products for an Fe-28 Cr-23 Co-1 Si alloy and faild to detect any mismatch between the two phases.

Since the lattice parameter of the alloys is a weak function of the concentration of the solid solution components,[74] namely $\bar{\eta} = (1/a)(da/dc)$ is small, the coherent spinodal, given by the locus of $f'' + 2\eta^2 Y = 0$ (where f" is the second derivative of the Helmholtz free energy and $\eta^2 Y$ is a strain-energy term), will be in approximately the same position as the chemical spinodal. The chemical spinodal curve can be calculated by the formula of Cook and Hilliard,[74]

$$Cs - Cc \simeq Ce - Cc\left[1 - 0.422(T/Tc)\right]$$

where Cs and Ce are the spinodal and equilibrium compositions at temperature T, and Cc is the critical compositions at the critical temperature Tc. Using Tc ~ 680°C and Cc ~ 0.25, as adopted from the estimated miscibility gas curve, the chemical spinodal is derived as shown in Fig. 53.

The asymmetry of the miscibility gap of the system can be explained by the effect of magnetic transition on the phase equilibria. It

is reported that a distinct anomaly is present in the solubility curves of alloying elements in some binary α-iron alloys.[77] Nishizawa et al.[78] computed the miscibility gap of αFe-X systems (where X is Cr, Be, Mo atom, etc) by a thermodynamic treatment in taking into account their magnetic transition, and found that the miscibility gap is not simply parabolic, but has a peculiar "horn" protruding out along the Curie temperature. They also found a similar shape for the miscibility gap in the αFe-X-Co system. In fact, some ferromagnetic alloy systems as well as Fe-Cr alloys in which the Curie temperature of one of the decomposed phase is located above the temperature of the top of miscibility gap exhibits a distinct asymmetry in the shape of the miscibility gap (e.g., Cu-Mn-Al system[59]).

Upon aging Alloy B for certain times (e.g., over 2 hr at 640°C), the alignment of the particles along ⟨100⟩ direction develop as shown in Fig. 9 and 11. The present observations find that this alignment tendency is more pronounced as the particles grow. This effect is believed to arise from the elastic interaction between particles,[79] the strength of which increases with increasing volume fraction of the precipitates and with increasing misfit between the particle and matrix. It is interesting to note that those precipitates which have a lattice misfit with the matrix being less than 0.1% do not show alignment,[79,80] a good example being the system Fe-15% Ni-15% Cr-3.5% Ti.[81] When the misfit exceeds ~1%, the particles form directly the periodic structure along ⟨100⟩ directions as rods or plates (e.g., Cu-Ni-Fe,[9] Cu-Ni-Cr,[82] Ni-Ti,[83] Au-Ni[52]). But when the misfit is ~0.5%, a transition occurs such that precipitates are spheres at the beginning of precipitation,

change their shape to cuboid-like or rods as well as their local distribution, forming the periodic structures, a good example being the system Ni-Al.[79,80] The present Alloy B is in this last category, since decomposition is isotropic in the early stage of aging when periodic structures of the two phases form, having an estimated mismatch of 0.6% at 600°C.

The modulated structures are associated with side-bands in x-ray diffraction or satellites in electron diffraction. Satellites appear along ⟨100⟩ cubic directions in many spinodal systems.[9,59,84] The present alloy exhibits halo-type diffuse satellites in the early stage of aging, followed by a parallel alignment along cubic directions, which indicate a change in morphology of the modulated structure. The appearance of the satellites is due to a modulation in both the scattering factor and of the lattice parameter. Since the differences in atomic scattering factor and lattice parameter of these elements are small, the intensity of the satellites is expected to be weak as is observed in the present alloys. The observation of satellites is also consistent with that of side-bands in Fe-Cr-Co-Si alloys by means of x-ray techniques made by Magat et al.[75]

The initial rate of growth of the wavelength varies, depending on the aging temperature. At lower aging temperatures, slower rates were observed, but after prolonged aging, the kinetics of growth obeys the relationship $\lambda \propto Kt^{1/3}$. The change in the rate of growth of wavelengths during aging has been observed in Nb-Zr[84] and Cu-Ni-Fe[85] spinodal systems, in which, however, no detailed studies of initial kinetics of growth were made. Recently, Pundariks and

Morris et al.[86] studied two phase decomposition in systems wherein like atoms energetically prefer to cluster. Using computer simulation and a basis of a simple microscopic lattice, they found that a Smoluchowski mechanism, e.g., $\sim t^{1/4}$ (Ref. 87) (direct coagulation of clusters) dominates at early times, followed by a Landau-Lifshitz law $t^{1/3}$. Binder et al.[88] also computed the process of phase separation and agreed with their results, showing that early stage coarsening obeys a $t^{1/4} \sim t^{1/5}$ kinetic law. This law fairly well agrees with the present observations, suggesting that a Smoluchowski mechanism may be dominant. The theory of diffusion-controlled particle coarsening developed by Lifshitz and Slyozov[64] and Wagner[65] (LSW) is applicable when the volume fraction of the dipersed phase is small. Ardell[89] modified the LSW theory and found that particle coarsening rates should increase with increasing volume fraction of precipitate, whereas the basic $t^{1/3}$ kinetics of diffusion-controlled coarsening are unaffected. However, his experiments on the Ni-Al system show that the rate constants (K) are independent of the volume fraction of the particles. This might be the case for the present Alloy B. The Alloy B produces different volume fractions, depending on the aging temperatures, but the rate constants vs temperature fit in one straight line fairly well (see Fig. 20). The activation energy for coarsening was found to be ~65 kcal/mole. No data on the activation of diffusion in ternary Fe-Cr-Co system are available; however, the activation energy for cobalt diffusion in ferromagnetic α-Fe is reported to be $\sim 63.6 \pm 2.3$ kcal/mole[90] in the temperature range (630~750°C), and that for Fe in the ferromagnetic α-Fe (683°C~884°C) and Fe-20 wt% Cr alloy (690°C~825°C) is

~60.7 kcal/mole[91] and ~51.9 kcal/mole,[92] respectively. It should be noted that the activation energy for diffusion in the ferromagnetic region is found to be higher than in the paramagnetic range. This is observed in iron,[91,92] cobalt[95] and other alloys.[90,92,96] The magnetic anomaly in diffusion is significantly affected by the exchange integral or the saturation magnetization of the basic lattice.[92] Comparing the observed activation energy with those available for binary alloys, the diffusion of Co might be the activated process for the coarsening of the Alloy B.

The results of the Curie temperature measurements show that the decomposed phases reach their equilibrium composition within almost 2 hr. The difficulty in detecting the Curie temperature of the α_2 phase in the alloys is that the magnetization curve of α_2 phase superimposes on that of the strong magnetic α_1 phase, resulting in a weak change in the slope of the curve. Particularly in the early stage of aging, no clear slope was detected. The higher the volume fraction of the α_2 phase, the sharper the observed discontinuity point in the magnetization curve. The compositional variation of Alloy A could not be measured by this technique since the volume fraction of the 2 phase in Alloy A is less than ~20%. Tahara et al.[97,98] studied the early stages of phase separation in the Fe-31 Cr-23 Co alloy (same as Alloy B) by Mössbauer spectroscopy and found that the composition reached the equilibrium one by a spinodal mechanism within about 10s for 560°C aging. They also found that aging Alloy B at 600°C or 560°C produced the paramagnetic Cr-rich phase, which is consistent with the present results.

The absence of superlattice reflections in the electron diffraction does not mean that the Fe-Co rich phase is not ordered, because the difference in atomic scattering factors of Fe and Co is so small that the intensity of superlattice reflections is expected to be too weak to be detected. In such a case, neutron diffraction is a powerful technique to detect the superlattice reflections. Vintakin et al.[99] confirmed the occurrence of B2 type ordering in the Fe-Co rich phase for an Fe-32 Cr-20 Co alloy by neutron diffraction. They found that aging the alloy at 650°C for 30 min already reveals superlattice reflections and that the intensity of the superlattice reflections increases with decreasing aging temperature, after sufficiant aging time at each temperature. This experiment suggests that the degree of ordering in the Fe-Co rich phase increases with decreasing aging temperature, which could be understood in referring the shape of the miscibility gap of the system. At lower aging temperatures, lesser amounts of Cr are contained in the Fe-Co rich phase.

5.2. Formation of σ Phase

The σ phase is hard, brittle, and non-magnetic at ordinary temperatures, so that the elimination of the σ phase in Fe-Cr-Co magnets is preferable from a properties point of view. In the present Alloy B, the σ phase is formed after slow quenching from the solution treatment temperature and after aging above 600°C. The rate of the formation of σ phase during aging can be estimated from the variation of saturation magnetization in Fig. 44. Aging at 660°C produces the σ phase in more than 50% of the total sample, within 1 hr. Aging at 640°C yields 20% σ phase after 20 hr. On the basis of these results some suggestions

can be made on the manufacturing of Alloy B. The alloy has to be quenched at a rate of over 100°C/sec after solution treatment, which necessarily limits the size of ingots. During thermomagnetic treatment, careful temperature controls are also required to avoid rapid formation of the σ phase. Higuchi[15] et al. studied the rate of formation of the σ phase in establishing the T-T-T diagrams of Fe-(25~30) Cr-(17.5~20) Co-1 Si alloys. They suggested that lowering of Cr, Co, and Si contents shifts the nose of the "C" curve to lower temperature and longer times, resulting in improved workability of the alloys.

The occurrence of the σ phase and its physical properties have been reviewed well by Hall and Algie.[100] The mechanisms for the body-centered cubic to σ phase transformation are suggested by Tucker[101] and Kitchingman.[102] Tucker has pointed out that the σ phase structure can be produced by small atom motions. The closed packed sheets of the σ phase structure may be formed by atom movements in a direction equivalent to the $[1\bar{1}1]$ direction in BCC. Kitchingman has proposed a transformation mechanism and suggested the crystallographic relations:

$$(1\bar{1}1)_{bcc} \parallel (001)\,\sigma$$

$$[1\bar{1}0]_{bcc} \parallel [\bar{1}40]\,\sigma$$

The present investigations, however, could not confirm his proposed relations. For example, the phase formed near the cubic directions of bcc, e.g., $[010]$ which is the trace of (101) or $(10\bar{1})$ plane of the matrix, as shown in Figs. 15-17.

The present investigation verifies that σ phase is stable at 600°C. It is interesting to inquire whether the σ phase is formed

below 600°C. Magat et al.[75] observed the diffraction lines of the σ phase after aging at 560°C for 1.5 hr in a plastically deformed Fe-28 Cr-23 Co-1 Si alloy. This is most likely due to the heterogeneous nucleation of the σ phase on the lattice defects induced by the plastic deformation, which is reported in deformed stainless steel.[103] Thus it can be said that σ phase could be stable to about 560°C.

5.3. Thermomagnetic Treatment

It has been shown that the thermomagnetic treatment is effective in elongating the Fe-Co rich phase parallel to the direction of the applied magnetic field, independently of the crystal orientation of the grains, but its efficiency decreases when the aging time exceeds 1 hr. This characteristic differs from that of the well known Alnico alloys. Heidenreich and Nesbitt[104] found that when the field was applied in the principal crystallographic directions (⟨100⟩, ⟨110⟩, ⟨111⟩), the direction of easy magnetization was the field direction. If the field is applied at a moderate angle to the ⟨100⟩ direction, the direction of easy magnetization lies between the field vector and the ⟨100⟩ direction. The difference in the effect of the thermomagnetic treatment on the microstructures between the Fe-Cr-Co and Alnico alloys is due to the difference in the morphology of the decomposition between two alloys, i.e., decomposition in the early stage of aging appears to be isotropic in the present alloy, but in Alnico alloys decomposition along the ⟨100⟩ directions is preferred.[13,104]

Thus the properties of Alnico alloys can be further improved with an alloy which has a ⟨100⟩ texture,[104] utilizing the anisotropic decomposition to more efficiently elongate the ferromagnetic phase

into the direction of the applied magnetic field. The Fe-Cr-Co alloy cannot be improved by such treatments.[24]

There are several theories on the alignment of the ferromagnetic particles by means of thermomagnetic treatment.[105] Kittel, Nesbitt and Shockley[106] suggested that the magnetostatic energy could control nucleation of the ferromagnetic particle so that only those nuclei with planes parallel to the applied field would form. Zijlstra[107] proposed a model in which a large amount of interfacial energy of initially decomposed fine spheres causes the spheres to grow during which time the spheres change to spheroids in order to minimize their magnetostatic energy. He concluded that the rate of elongation of the particles in Alnico 5 is related to the difference between the corresponding decrease of the magnetic free energy and the simultaneous increase of the interfacial energy. But the latter was found to be extremely small in Alnico 5. Cahn[108] takes into account the magnetostatic and elastic energies in his theoretical model on the effect of magnetic aging on spinodal decomposition. If the anisotropy in magnetostatic energy is very much larger than elastic energy anisotropy, the decomposition ignores the crystallography and gives plane waves whose superposition resembles two phases in rod form parallel to the magnetic field. If the elastic energy anisotropy is the larger, then the magnetic field perfers those waves of the favored crystallographic orientation that are closest to being parallel to the magnetic field. He also suggested that to maximize the effect of the magnetic field, one should age as near to the Curie temperature of the original homogneous alloy as possible.

The present alloy seems to behave according to Cahn's model. In the early stage of aging, decomposition takes place isotropically when the magnetostatic energy dominates over the elastic energy, and the FeCo rich phase grows in parallel to the direction of the applied field. But when the aging time exceeds 1 hr, the elastic energy gradually becomes greater than the magnetic energy, aligning the Fe-Co rich phase along the elasticity soft ⟨100⟩ cubic directions (see Fig. 36), resulting in a decreasing efficiency of the elongation.

Thus a higher degree of alignment of the particles could be achieved in those alloys which have less misfit between the decomposed phases. For example the microstructures of the thermomagnetically treated Fe-23 Cr-15 Co-5 V alloy and Fe-28 Cr-15Co-1Nb-Al Alloy[67] are shown in Figs. 54 and 55, respectively. Both of the figures indicate that the degree of alignment of Fe-Co rich phase is better than that of alloy B (compare with Fig.33). This picture can be clearly seen in the microstructure perpendicular to the applied field direction as shown in Fig. 55(b), as compared to that of alloy B shown in Fig. 34(b). In Fig. 55(b), the Fe-Co rich phase particles are spherical indicating that they are well aligned along the field direction, but in Fig. 34(b) the Fe-Co rich phase shows a modulated structure, not exactly elongated with the field direction. As a matter of fact, the optimum temperature for the thermomagnetic treatment in the Fe-23Cr-15Co-5V alloy is 650°C,[23] which will give less misfit between phases in the alloy B. At 660°C the rapid formation of the non-magnetic phase intrudes.

One possible method to improve the magnetic properties of Fe-Cr-Co alloys should be that of adding elements which make the decomposition

anisotropic, as Ti additions do in Alnico 9.[13] This means increasing the elastic strain energy to assist the elongation of the ferromagnetic particles along ⟨100⟩ cubic directions while the magnetic field is applied along ⟨100⟩ direction in alloy which have ⟨100⟩ textures. An example of such an element to increase the elastic energy in this system is reported to be Mo.[1,109] Although the addition of Mo to Fe-Cr-Co improves the magnetic properties,[1] it is not a practically attractive method since Mo stimulates the formation of the embrittling σ phase.

5.4 Step-Aging

It is shown that isothermal aging itself fails to produce the optimum microstructure for good Fe-Cr-Co magnets. Aging at 640°C does not develop the nonmagnetic α_2 phase. Aging at 600°C also produces an undesirable microstructure because it results in a dispersion of the nomagnetic α_2 phase within the α_1 phase. However it is shown here that these problems can be overcome by optimum step-aging, which gives a microstructure of elongated ferromagnetic α_1 phase imbedded in the paramagnetic α_2 phase.

Optimum step aging increases the coercive-force remarkably, while preserving the remanence enhanced by TMT. The investigations of the corresponding microstructure during step-aging show that the composition of the two phases changes without changing the morphology of the microstructure developed by TMT. Therefore, the increase in coercivity during step-aging is believed to be associated with a change in compositon of the two phases, resulting in an increase in the difference between the magnetizations of the two phases.

These results are consistent with those reported by Magat et al.[75] and Cremer et al.[109] Magat et al., monitored the step-aging process by x-ray diffraction and found that the satellites did not change in position but their intensity increased, indicating an increase in modulation amplitude. Cremer et al. followed this effect by measuring the temperature dependence of the magnetic properties and concluded that the composition of the two phases are changed during step-aging. In 1948, Daniel[110] already adopted the step-aging method to alter the compositional amplitude in keeping the wavelength being constant for studying the diffusion in the Cu-Ni-Fe alloy.

After step-aging, the saturation magnetization (4 Is) increases with decreasing step-aging temperature (see No. 16-17 in Table III). This is due to the fact that the solubility of Cr in the Fe-Co rich phase decreases with decreasing temperature in keeping with the shape of the miscibility gap. It is also observed that the induced anisotropy along the field direction increases by step-aging. It is believed that the increase in difference of the magnetization of the two phases increases the magnetostatic energy of the Fe-Co rich particle along the short axis, causing the magnetic spin to lie along the lower magnetostatic energy position, namely along the long axis of the particles. Then an increase in the induced anisotropy during step-aging is associated with an increase in difference of the magnetization of the two phases.

However, secondary decomposition prevents any improvement of the magnetic properties. A possible explanation of this may be that the spherical, ultrafine (< 45Å diameter) particles behave as superparamagnetic domains.[111] Thus it is important to consider under

what conditions secondary decomposition occurs. The condition might be explained in referring to the spinodal curve drawn in the miscibility gap shown in Fig. 53. The composition of the α_2 phase after the thermomagnetic treatment could be estimated from the results of its Curie temperature measurements (Fig. 22), denoted as x in Fig. 53. After the thermomagnetic treatment, aging at 620°C would be done in the region of classical nucleation between the binodal and spinodal curve (denoted Y in Fig. 53), so that the free energy required to create a nucleus could be described by[112]

$$\Delta G^* = \frac{16\pi\gamma}{3\Delta G_v^2} \propto \frac{\gamma^3}{(\Delta T)^2}$$

where γ is the interfacial energy of the new nuclei and decomposed phases and ΔT is the undercooling. The smaller the undercooling ΔT, the larger the fluctuation in free energy required to create a nucleus. Therefore, when ΔT is small enough so that no new nuclei form, diffusion would only alter the compositions of the two phases without changing the morphology of the microstructures.

However, aging at or below 600°C after the thermomagnetic treatment occurs within the spinodal region as designated as Z in Fig. 53. Under these circumstances it might be possible that the two phases developed during TMT further decomposes into two phases ($\alpha_1' + \alpha_2'$) along the new conjugate tie-line ($\Delta T \geqslant 40°C$).

The critical degree of undercooling for occurrence of the secondary decomposition is ~40°C, the value of which is consistent with that found in the Fe-Cr-Co-V alloy.[71] But the critical ΔT must be varied depending on the alloys system.[13,69] It should be noted that the

volume fraction of the secondary decomposed products ($\alpha_1' + \alpha_2'$) in the α_2 phase must differ from tha in the α_1 phase; namely the α_1' phase is major in the α_1 phase, but the α_2' phase is major in the α_2 phase. In the present investigation these microstructural features are not observed, probably because of the preferential etching of the α_1 phase.

5.5 Magnetic Domains

The interpretation of the domain patterns observed in the isothermally aged alloy is straight-forward, showing the typical patterns of a uniaxial ferromagnetic material. The direction of the easy magnetization in the alloy is found to be ⟨100⟩. Thermo-magnetic treatment alters this however to a direction closely parallel to the applied field.

Step-aging increases the induced anisotropy, producing the microstructure such as the Fe-Co rich ferromagnetic particles of a single domain size dispersed within the paramagnetic Cr-rich phase. Such a microstructure does not involve the formation of conventional-type domains or domain walls at all. Thus, the domain or domain walls observed in the step-aged alloy by the powder method in the present investigation or reported[70] by Shur et al., should not be regarded as the usual Bloch walls. It is then interesting to see what is the nature of the domain or domain walls observed by powder pattern in the step-aged alloy. The same situation is also encountered in high coercive Alnico alloys.[113,116] Craik and Issac[117] interpreted such a powder pattern in terms of interaction domains, i.e., regions in which the magnetic moments of the precipitate particles are mutually

aligned by magnetostatic interactions rather than by exchange forces. The contrast of the powder pattern arose from the interaction domains as discussed by Iwama,[118] which is consistent with those observed. He also found that the contrast between black and white portions in the striped powder pattern is reversed on reversal of the field applied perpendicular to the observed surface.

The observed domains or domain walls in the step-aged alloy by transmission Lorentz microscopy might be also interpreted in terms of the concept of interaction domains as illustrated in Fig. 56. The two interaction domains which have opposite magnetization directions deflect the incident electron beam to form imaginary domain walls when the optimum defocus length is taken. The defocus length of the step-aged alloy (~40 μm in Fig. 52) is found to be larger than that of the isothermally aged alloy (~30 μm in Fig. 49). This could be seen in the background of the micrographs. The observed imaginary domain walls are blurred in comparison with that in the isothermally aged alloy. This might be another indication that the imaged domain wall in the step-aged alloy is not of the usual Bloch-type. A simple calculation can be made to see how much deflection angle (ψ) is required to form the imaginary domain wall in step-aged alloy. The measured divergent wall ($Wd = \delta o + 2Z\psi$) in the step-aged alloy is ~650 $\pm$ 200Å. Putting the values, δo (true width of wall) ~ 0 Z ~ 40 μm, yields the deflection angle ($\psi \sim 8 \times 10^{-4}$ radian). This ψ is 2.5 times as large as that calculated for the case where the incident beam is deflected by a thin foil (thickness ~1500Å) of the single phase Fe-33 Co alloy ($4\pi Is \sim 24$ kG), according to the equation $\psi = e\lambda t 4\pi I_s/Ch$.[56] This

might indicate that the deflection of the incident electron beam by the two phase mixture (e.g., Fe-Co rich phase imbedded within the paramagnetic phase) is stronger than that produced by the single Fe-Co phase, suggesting that the deflected beam by one Fe-Co rich particle would be further displaced by another Fe-Co particle as the beam passes through the foil. Since the contrast mechanism of magnetically inhomogeneous material (α_1 and α_2) phase in Lorentz microscopy is complex, more experiments are needed to prove the existence of the proposed interaction domains.

5.6 Correlation Between Spinodal Microstructures and the Magnetic Properties

Magnetic properties (Br, Hc, 4πIs and (BH)max) of the Fe-Cr-Co alloys are affected by many factors of the spinodal microstructure among which the following parameters are considered: (1) the composition of the constituent phases, (2) volume fraction of the phases, (3) size, shape of the phases, and (4) the morphology of the microstructure such as the degree of alignment of the Fe-Co rich phase. Correlation of the structure-insensitive properties such as the saturation magnetization (4πIs) with these parameters (volume fraction and compositions of the phases) is very well known. In this section main emphasis will be focused on establishing the correlation between the structure-sensitive properties such as Hc or Br with these properties.

5.6.1 Isothermally-Aged Alloy

A. Fe-31Cr-23Co

The variation of the coercive force is replotted against $t^{1/3}$ (aging time) in Fig. 57. This figure illustrates that the coercive force increases linearly with $t^{1/3}$ until it reaches a maximum, and

then decreases. As discussed earlier the wavelength varies as $t^{1/3}$ (Fig. 19), so that the variation of coercive force up to the maximum value must be expressed by the linear function of the wavelength or the diameter of the particles. This section will consider how the coercive force of the isothermally aged alloy can be expressed by the microstructural parameters.

It has been shown through the domain observations that the reversal mechanism for the isothermally aged alloy is domain wall pinning. But the mode of the domain wall pinning differs, depending on the microstructure. Aging at 640°C produces a structure of Fe-Co rich particles imbedded within the weakly ferromagnetic α_2 phase, where the domain walls tends to lie exclusively within the α_2 phase and are pinned by the strongly ferromagnetic Fe-Co rich particles. Aging at 600°C develops the non-magnetic Cr-rich phase dispersed within the Fe-Co rich phase, where the non-magnetic Cr-rich particles are the pinning sites of the domain walls movement in Fe-Co rich phases. The latter case was treated by Kersten[119] and Neel.[120] The present highly simplified model is to treat the former case almost the same way as was done by Kersten, in concerning a cubic array of spherical Fe-Co rich particles separated in the Cr-rich phase by λ as shown in Fig. 58.

It is found that the coercive force can be expressed by the following equation when the domain wall thickness δ is much greater than the Fe-Co particle diameter, d. The derivation of the equation is referred to the Appendix I.

$$H_c \approx \frac{(\gamma_1 - \gamma_2)d}{Is\,\delta^2}\ \alpha^{2/3} \quad \cdots \qquad (5.6.1)$$

where γ_1 and γ_2: domain wall energies of the α_1 and α_2 phases, respectively, Is: saturation magnetization of the matrix and α: packing fraction of the particles.

But when the particles diameter d is much greater than the wall thickness, the coercive force is given by

$$Hc \approx \frac{(\gamma_1 - \gamma_2)}{Is\ d}\ \alpha^{2/3} \quad . \qquad (5.6.2)$$

Among the parameters in these equations, only the diameter of the particles changes during isothermal aging after 2 hrs. The coercive force in either Eg. (5.6.1) or (5.6.2) will be maximum when $\delta \approx d$, reducing both equations to the same expression,

$$(Hc)\max \approx \frac{(\gamma_1 - \gamma_2)}{Is}\ \alpha^{2/3} \quad . \qquad (5.6.3)$$

The coercive force of the alloy aged below 600°C will be given by these equations when substituting $\gamma_2 = 0$, which are basically the same equation derived by Kersten. But aging at 620°C develops the weakly magnetic Cr-rich phase dispersed within Fe-Co rich phase, so that γ_2 is not zero in the equations.

These results can explain fairly well the variation of the coercive force with aging time in Fig. 57, i.e., the initial linear relationship between Hc and d can be expressed by Eq. (5.6.1) and the maximum Hc by Eq. (5.6.3), and followed by the decrease of Hc given by Eq. (5.6.2). For an example, the diameter of the particles

corresponding to the maximum coercivity at 640°C, 620°C and 600°C aging is found to be around 200Å, 250Å and 150Å, respectively. These values are fairly consistent with the observed domain wall thickness except 600°C aging. Likewise, the maximum coercive force after aging 640°C could be calculated in substituting examples of the numerical values in Eq. (5.6.3). The examples of the numerical values are estimated or calculated as shown in Appendix II, and are listed in Table V. After aging at 640°C, the wall energy of the Cr-rich phase (γ_2) was estimated to be 2.64 erg/cm^2 from the results of the observation of the domain wall thickness ($\delta \approx 300$Å), and the magnetization per unit volume (Is) of the Cr-50% Fe phase would be approximately 600 emu/cm^3. The cobalt in this phase probably increases Is to at least 700 emu/cm^3. Inserting these values and $\gamma_1 = 3.5$ erg/cm^2, $\alpha \sim 0.45$ into Eq. (5.6.1) yields $(Hc)_{max} \approx 250$ Oe, a value in fair agreement with the peak experimental coervicity of about 170 Oe.

It is clear that the above discussion is based on an extremely simplified model, which assumes spherical particles as inclusions. But microstructure studies reveal that the particles are rod-like and have a tendency to align alloy ⟨100⟩ directions. The domain walls also tend to lie along ⟨100⟩ directions. Thus in fact there arise two cases where the walls are held straight by rod-like inclusions (1) which run parallel to the easy axis in the plane of the walls or (2) which run normal to the easy axis (but in the plane of the walls). In the former case, the walls may bulge in such a way that they remain parallel to the magnetization, so that no demagnetizing energy is created. But in the latter case, the bulging must give rise to magneto-

static energy corresponding to the component of the magnetization across the walls. This effect was shown to be generally much greater than the wall energy effect.

A most important factor neglected in the present approach discussed above is this magnetostatic energy of the inclusions. Neel[120] first pointed out that a domain wall in passing an inclusion, lowers the magnetostatic energy. Dijkstra and Wert[121] calculated the reduction of both of the magnetostatic energy and the wall energy bar spherical non-magnetic inclusions in Fe and found that the two effects are about equal for particles of the order $\delta/4$; for particles smaller than this the reduction of the wall energy predominates. Therefore it may be possible that lowering the magnetostatic energy dominates in the case (2) discussed above, especially when the diameter of the particles is over $\sim\delta/4$. However in the other case, the domain wall effect would be an important factor in considering the coercive force of the isothermally aged alloy.

In summary, referring to equation 5.6.3 the coercive force due to the mechanism of domain wall pinning can be improved by increasing $(\gamma_1 - \gamma_2)$ and α or decreasing $4\pi I_s$ and δ within the matrix phase. This indicates that the crystal anisotropy (K) of the two phases is more important than $4\pi I_s$ of the particle. In fact Song[17] reported that the addition of small amounts of Sm metal increases the coercive force of the isothermally aged Fe-30Cr-25Co alloy up to 950 Oe. Since Sm metal is known to be the forming element of the intermettalic compounds (Re-Co) with high crystal anisotropy, this might be an indication

that the crystal anisotropy (K) is the controlling factor of the coercive force of isothermally aged alloy.

B. Fe-16Cr-28Co

The coercive force of the Alloy A does not vary much during isothermal aging below 620°C as shown in Fig. 43. This reflects the fact that the formation of the Cr-rich phase in the Fe-Co rich matrix has little effect on the coercive force. Substituting the examples of the numerical values, $\gamma_1 \sim 2.7$ erg/cm^2, $\gamma_2 \sim 0$, $\alpha \sim 0.2$, Is $\sim$ 1900 emu/cm^3 and $\delta \sim 670$Å into the equation 5.6.3 yields a coercive of 70 Oe, which is in fairly good agreement with the experimental values. Aging at 640°C, however, produces some variation in the coercive force. Powder patterns corresponding to these curves (a) as-quenched, (b) 640°C for 20 min, (c) 20 hr and (d) 100 hr, are shown in Fig. 59. As discussed earlier, the change in the morphologies of the powder patterns arise from the microstructural changes of the alloy. In the early stages of aging, the magnetic particles seem to be attracted to the lath boundaries of the decomposed martensite in Figs. 59(a) and (b). But in Figs. 59(c) and (d) they appear to be segregated in the decomposed martensite rather than the fresh martensites formed during quenching from the aging temperature. This could be due to the fact that the decomposed martensite has a higher saturation magnetization than the newly formed martensite since the decomposed martensites precipitated out a large amount of the chromium, but the latter ones still contain Cr atoms. As a matter of fact, the saturation magnetization (4πIs) decreases with increasing martensite which has no decomposed products. Thus the increase in coercive force up to 150 Oe during agint at 640°C might be due to

the formation of fresh martensite which acts as domain wall pinning sites.

C. Cr-26Fe-13Co

The Alloy C shows the highest coercive force among the present alloys after isothermal aging. The variation of the coercivity could not be described by a linear function of the diameter of the particles as that of the Alloy B could. Since the Cr-rich matrix phase is found to be non-magnetic after aging below 600°C, the domain wall pinning model is not applicable to this Alloy C. A detailed consideration of the magnetic hardening of the alloy is the subject of the next section where the same situation is encountered.

5.6.2 Step-Aged Alloy

Step-aging produces ferromagnetic Fe-Co rich particles of approximately 150Å in diameter imbedded within the paramagnetic Cr-rich phase. In such a microstructure the domain wall cannot lie within Fe-Co or Cr-rich phases, and the magnetization reversal process should be considered in terms of single domain behavior. In this section experimental results are tested against various theories on magnetic hardening by fine particles. For simplicity, thermal effects on the magnetization properties of the fine particles are neglected and the Fe-Co rich particles are assumed to be prolate spheroids. Various magnetic constants for the calculations are listed in Table V, some of which being unavailable in the literature are derived in the Appendix II.

A. Coherent Rotation

Stoner and Wohlfath[122] calculated the hysteresis loops of elongated single domain particles, reversing their magnetization by coherent rotation. Since the crystal anisotropy of the Fe-Co particle is smaller than Fe,[123] it is assumed that magnetic anisotropy of the alloy is only due to the shape of the particle. The critical size of elongated ferromagnetic particles, below which the coherent rotation occurs is given by[124]

$$Nb r^2 Is^2/6A = \log(2r/a) - 1 \qquad (5.6.4)$$

$$Nb = \frac{4\pi}{m^2-1} \quad \frac{m}{(m^2-1)^{1/2}} \ln \; m+(m^2-1)^{1/2} \; - 1 \qquad (5.6.5)$$

r: radius, a: lattice parameter, Nb: demagnetizing factor along major axis, Is: saturation magnetization, A: exchange constant, and m: axial ratio of length to diameter.

Substituting the numerical value in Eq. (5.6.5), the critical diameter for single domain behavior is plotted against aspect ratio m in Fig. 60, which shows that the observed diameter (130 ~ 170Å, m ~ 3) of the Fe-Co rich particle in step-aged alloys is within the single domain size. According to their calculation the coercive force of the elongated particles is given by

$$Hc = R(1 - P)(Na - Nb)Is \qquad (5.6.6)$$

where Nb: demagnetizing factor along minor axis, R: numerical factor relating the coercive force of the randomly oriented assembly ($R \approx 0.48$)

to that of the perfect aligned assembly (R = 1), P: packing factor of the particles.

It should be emphasized that a coercive force is independent of diameter of the particle as long as the particle remains single domain. Substituting the numerical values, P ~ 0.55, Is ~ 1900 emu/cm^3, m ~ 3 into Eq. (5.6.6) yields a coercive force of 2100 Oe for the random state and 4400 Oe for the aligned state. However, the observed value of coercive force is around 400 Oe ~ 600 Oe in Alloy B. It should be noted that the observed coercive force (Hc(A)) on the step-aged alloy under a magnetic field (with the alignment of the particles) is found to be almost the same as that (Hc(R)) without it (for a random arrangement), although the remanence of the both alloys differs considerably, i.e., $Br/4\pi Is$ = 0.88, 0.65 with or without a magnetic field, respectively. (See present Table III and Table I in a Ref. 1.) These discrepancies between calculated and experimental data suggest that the reversal mechanism of the alloy would not be due to the coherent rotation mode.

B. Fanning

Jacobs and Bean[125] proposed the chain-of-spheres fanning model due to the "peanut shape" of the electrodeposited iron particles observed by electron microscopy. They considered two possible reversal mechanism: (1) symmetrical fanning as illustrated in Fig. 61(b), (2) parallel rotation mechanisms in Fig. 61(c), and found that the coercive force by two mechanisms is given by

$$Hc = R' \frac{\pi Is}{6} \quad \text{(symmetrical fanning)} \qquad (5.6.7)$$

$$Hc = R\frac{\pi Is}{2} \quad \text{(parallel rotation)} \tag{5.6.8}$$

Where R' = 1 for aligned chains or R' = 1.13 or 1.08 for randomly oriented, two and infinite chains, respectively. R is the same as that defined in Eq. (5.6.6).

The consequences of this model are (1) the coercive force is independent of size of the particle, the same as for the Stoner and Wohlfarth model, and (2) a peak in the angular variation of coercive force rather than a monotonically decreasing function. Substituting the numerical values (P = 0), the coercive force of aligned or randomly oriented two sphere chains by symmetrical fanning is around 1000 Oe or 1120 Oe, respectively. This calculations qualitatively agree with the experimental results ($Hc(A) \approx Hc(R)$). The coercive force will depend on the packing of the particles, because there are surface charges on each of the particles in the saturated state and these modify the field inside the other particles. Taking into account the packing fraction, Hc(A) ~ 550 Oe, Hc(R) ~ 620 Oe, These values are fairly in good agreement with the experimental values. This fair agreement is believed to be due to the actual shape of the Fe-Co rich particles. Referring to the micrographs in Figs. 34 and 37, the Fe-Co rich particles will be described by a peanut shape rather than by prolate spheroids. The calculation was made assuming symmetrical fanning because of its lower energy mechanism. It should be noted that the symmetrical fanning mode implies negligible exchange interaction between adjacent spheres because of their point contact. But if the contact area between spheres increases, the exchange forces would

favor parallel rotation mechanism. In Figs. 34 and 37, the actual shape of the Fe-Co particles is closer to a chain of squashed-together spheres than to a chain of spheres in point contact. Thus the actual mode may be a mixture of these fanning effects.

C. Curling

Brown[126] and Frei and co-workers[127-130] theoretically examined the mode of incoherent reversal, in which all spins do not remain parallel (opposed to coherent rotation), by the method of micromagnetics. Their calculations[127] show that coercivity in the curling mode is markedly size-dependent. The critical size will generally be given in terms of the characteristic diameter of the material.

$$do = 2\, A^{1/2}\, Is^{-1} \qquad (5.6.9)$$

where A is the exchange constant (do~143Å for Fe-33Co). Their results show that the critical size is practically independent of crystal anisotropy and of elongation.

Nucleation field (Hn) for the prolate spheroid particles is given by

$$Hn = NbIs - 8\pi k \frac{Is}{(d/do)} \geq Hc \qquad (5.6.10)$$

where k depends on the axial ratio m and varies from 1.08 for the infinite cylinder to 1.39 for the sphere (e.g., m = 3, k ~ 1.25).[131] It is assumed for simplicity that Hn (nucleation field) = Hc (coercivity) for prolate spheroids as it holds for an infinite cylinder.[127] Putting the numerical values (P = 0) into Eq. (5.6.10), the coercive force for aligned particles is plotted vs. the diameter of the particle

with varying the axial ration (m) in Fig. 62. Considering the present results i.e., d $\approx$130 ~170Å (m = 3),the coercive force expected by the curling mechanism will be 1.5 x 10^4 ~ 8 x 10^3 Oe, the values of which are very much higher than the experimental values and are close to that calculated by coherent rotation. According to the calculations by Frei et al., coherent reversal is the lower energy mechanism for S(=d/do) $\leq$1, but the curling mechanism is favored for S $>$1. Thus when S $\leq$1, for randomly oriented samples, Hc $\approx$0.48 Hc(A) (aligned), given by Stoner and Wohlfarth model. But for S $>$1, Hc(R) varies depending on the value of S, e.g., Hc(R) $\leq$ Hc(A) for S $\leq$ 1.47 and Hc(R) $>$Hc(A) for S $>$1.47.[132] For example, Hc(R) ~ 0.64 Hc(A) for the present case S ~ 1.2 (= 170/143). Therefore when d ~ 170Å (m = 3), Hc(A) ~ 8000 Oe, and Hc(R) = 5100 Oe. These results are not consistent with the experimental values, Hc(R) $\approx$ Hc(A).

The calculations above are summarized in Fig. 63. The chain-of-spheres model appears to be the lowest energy mechanism for magnetization reversal for the step-aged Alloy B. This conclusion, however, is not rigid since the coercive force of only two cases (randomly and aligned particle assemblies) are considered. From the above analysis it is presumed that the shape irregularities of the Fe-Co rich phase in Alloy B gives rise to the observed properties. For uniform elongated particles the curling mode will be the lowest energy mechanism of magnetization reversal as seen in Fig. 63, so that it will be possible for even Alloy B to undergo a different reversal mechanism when the morphology of the Fe-Co particles is changed. For example, swaging[14,24] which improves the Hc and Br, produces uniform elongated particles

in which the curling mode might be dominant. It is reported that the fanning mode adequately describes the magnetic properties of elongated Fe or Fe-Co particles magnets comprised of irregularly shaped particles,[133] but the curling mode could dominate after wire drawing of the magnets.[134]

The Fe-Co rich phase in the isothermally aged alloy C cannot be described as "peanut shape" as shown in Fig. 31 and the coercive force of the alloy C shows some size dependence; hence the reversal mechanism of alloy C should be different from the chains of spheres fanning mode. In order to quantitatively analyze the magnetization reversal mechanism of the alloy B and C, more experimental data are required such as 1) the dependence of the particle size on the coercive force, holding the magnetization of the particle constant, 2) the angular dependence of coercive force on particle diameter, 3) the rotational hysteresis integral as a function of diameter.

5.7 General Comments on Future Development of Fe-Cr-Co Magnets

There seems to be two ways to go for the future development of Fe-Cr-Co magnets, (1) one is to aim for better properties with alloys containing less Cr <25% and Co <15% content, and (2) the other is to obtain high coercive force (~>1000 Oe) by increasing the Cr and Co content in the alloys.

It should be noted, particularly for (2), that the ductility of the alloy which is one of the advantages of this magnet, decreases with increasing Cr content. For example, the fractographs of the alloy B (31Cr) and C(61Cr) in the as-quenched state are shown in Fig. 64 and 65, respectively. Figure 64 shows a mixture of ductile (b) and cleavage (c) fracture modes, but Fig. 65 exhibits only cleavage

fracture. The brittle fracture mode might be due to 1) the existence of the σ phase or 2) the inherent nature of the material. Careful microstructural observations suggest that cleavage fracture is an essential property of the alloy C because the very small amount of σ phase in the structure (e.g., Fig. 30(a)). These results indicate that Cr content of the alloy should be limited to keep good ductility of the magnets.

The methods to further improve the magnetic properties (especially Hc) of Fe-Cr-Co alloys will differ, depending on the microstructural features, such as the Fe-Co rich phase imbedded within (1) weak ferromagnetic or (2) non-magnetic Cr-rich phase. Microstructures of (1) type will be found in alloys having Cr < 25% and Co < 15% since more Fe atoms will possibly be contained in Cr-rich phase in these alloys, and those of (2) type will be obtained in the alloys containing high Cr content.

It is proposed that in such a microstructure as type (1) the magnetization reversal mechanism will be due to domain wall pinning by the α_1 phase, where the maximum coercive force will be given by equation 5.6.3. Higher coercive force will be expected when the difference in wall energies of two phases ($\gamma_1 - \gamma_2$) and the packing fraction of the particles (α) become greater, while the saturation magnetization ($4\pi Is$) and the thickness of the wall of the matrix phase become smaller. Thus the crystal anisotropy (K) of the Fe-Co particle is rather important than the $4\pi Is$ of the particle.

Now it is interesting to see how these parameters vary during a step-aging process. It is reported that K of Fe-Co alloys decreases

with increasing Co content and becomes zero for an Fe-40 wt% Co alloy.[123] This means that the wall energy of the Fe-Co particle (γ_1) is decreasing during the step-aging process. The other parameters such as γ_2, δ and $4\pi Is$ might also decrease. Then the increase in coercive force during the step-aging of the microstructure type (1) would be attributed to a decrease in $4\pi Is$ or δ of the Cr-rich phase (increase in α is neglibly small). The decrease in δ is also associated with reducing the optimum diameter of the particle (d) since optimum coercive force will be achieved for $\delta \approx d$. Therefore, one possible method to improve the magnetic properties of the alloy with the microstructure type (1) should be that of adding those elements which increase the crystal anisotropy of the Fe-Co rich phase. Rare-earth metals will be a good candidate for this purpose since they are known to be the constituents of the intermetallic compounds (Re-Co) with high crystal anisotropy. In fact, Song[17] reported that even a small amount of Sm metal increased the coercive force of the isothermally aged Fe-30Cr-25Co alloy up to 950 Oe. This would suggest that one of the strong controlling factors of the coercive force given by the domain wall pinning could be crystal anisotropy (K).

In such a microstructure as type (2), the domain wall cannot lie within the Cr-rich phase, suggesting that the magnetization reversal mechanism will be given by the fine-particle theory such as coherent rotation, fanning and curling modes. All three models agree to predict such a desirable microstructure for better properties as the highly elongated Fe-Co rich particles with high $4\pi Is$ dispersed within the paramagnetic phase. As discussed earlier, such a microstructure would

be achieved by the following methods: (1) Utilizing anisotropic spinodal decomposition to more efficiently elongate the Fe-Co rich phase into the direction of the applied magnetic field in a ⟨100⟩ texture sample or (2) swaging or drawing to mechanically align and elongate the Fe-Co rich particle. The latter method has a disadvantage in that it limits the shape or size of the magnets. For the former case two factors must be taken into account, (1) finding the adding elements which make the decomposition anisotropic and (2) developing a ⟨100⟩ texture. The ⟨100⟩ texture of Fe-Cr-Co alloys would be developed by means of (1) columnar crystals or (2) recrystallization[24] using $\gamma \rightarrow \alpha$ transformation. It is hoped that the ⟨100⟩ texture might be achieved by easy thermomechanical treatments, utilizing the advantage of the good ductility of these alloys.

6. SUMMARY AND CONCLUSIONS

The microstructures and magnetic properties of spinodal Fe-Cr-Co ductile permanent magnet alloys have been investigated. From this work the following conclusions have been drawn:

1. Three alloys along the same conjugate tie-line exhibit two types of microstructures in the as-quenched state; 1) a single phase (bcc) in the Fe-31%Cr-23%Co (B) and the Cr-26Fe-13Co (C) alloys, and 2) lath martensite in the Fe-16Cr-28Co (A) alloy. The alloy B must be quenched at a rate of over 100^{o}/sec to obtain a single α phase.
2. Isothermal aging of the alloys inside a miscibility gap results in the decomposition into two phases, an Fe-Co rich phase (α_1) and a Cr-rich phase (α_2). The lattice imaging technique reveals that the two phases are coherent.
3. Microstructural changes during isothermal aging of the alloy B are summarized as follows:
   (i) The decomposition process appears to be isotropic, as evidenced by halo-type diffuse satellites in diffraction patterns. Continued aging develops a periodically modulated structure along ⟨100⟩. The occurence of this transition is possibly due to an elastic interaction between particles, particularly when the misfit between the two phases is around 0.4 ~ 0.6%.
   (ii) The kinetics of the growth of the wavelength is described by a $\lambda \propto kt^n$ law where n was found to be 1/4, 1/5 and 1/20 in the early stage of aging (Smoluchowksi mechanism) at 640^{o}C,

620°C and 600°C, respectively. But prolonged aging results in identical values of n = 1/3 (Lifshitz, Slyozov mechanism) for all three different temperatures. The activation energy for coarsening is about 65 kcal/mol, which corresponds with that of Co diffusion in the alloy.

(iii) Curie temperature measurements show that the decomposed phases reach their equilibrium composition within about two hours aging. Aging at 640°C produces the magnetic Cr-rich phase, but at 600°C the non-magnetic phase is formed.

(iv) The formation of the embrittling σ phase occurs at various stages of aging inside and/or ouside the miscibility gap. σ phase appears to be precipitate either on grain boundaries or inside grains. The morphology of the γ phase varies from plate-like to a circular type, depending on the aging condition.

4. Isothermal aging of the alloy A develops a rod-like Cr-rich phase homogeneously within the martensite plates. Aging at 640°C is also associated with the formation of the austenite, which transforms to martensite during quenching from the aging temperature to iced brine. The transformation temperature is measured as M_S ~ 158°C, and Mf ~ 60°C. The phase transformations occurring in the alloy are summarized as follows:

$$\gamma(\text{fcc}) \xrightarrow{\text{Quenching}} \alpha(\text{Martensite}) + \varepsilon(\text{hcp}) \xrightarrow{\text{Aging at } 640^\circ\text{C}}$$

$$\alpha_1 + \alpha_2 + \gamma_{fcc} + \varepsilon \xrightarrow{\text{Quenching}}$$

$$\alpha_1 + \alpha_2 + \alpha' \text{ (Martensite)} + \varepsilon$$

5. Alloy C exhibits a miscibility gap below 620°C, and results in a rod-like Fe-Co rich phase upon aging.
6. Magnetic properties of the isothermally aged alloys (A, B and C) were measured and it was found that alloy B is best as a permanent magnet among the three alloys because of its combination of good ductility and good magnetic properties.
7. Isothermal aging of the alloy B fails to improve magnetic properties. Aging at 640°C develops the magnetic Cr-rich phase. Aging at 600°C produces a non-magnetic Cr-rich phase dispersed within the Fe-Co rich phase. The variation of coercive force during isothermal aging is explained by a modified Kersten's theory for domain wall pinning. Observations of domain walls by Lorentz microscopy support this pinning model in isothermally aged alloys.
8. The thermomagnetic treatment (TMT) of the alloy B mainly improves remanence (Br), by elongating the Fe-Co particle along the direction of the applied magnetic field. Optimum TMT of the alloy B involves aging at 640°C for 40 min to 1 hr in a magnetic field of 2 kOe.
9. Step-aging after TMT improves mainly the coercive force, by increasing the difference in the composition of the two phases, while preserving morphology of the microstructure. The Cr-rich phase which is magnetic after TMT becomes non-magnetic after step-aging. The resulting desirable microstructure is comprised of elongated Fe-Co rich particles imbedded within a paramagnetic Cr-rich phase. The domain walls imaged in these alloys by Lorentz microscopy are interpreted as imaginary walls of interaction

domains. A desirable microstructure is only produced when the step-aging interval (ΔT) is small. When the alloy is aged at low temperatures after TMT ($\Delta T \geq 40^{o}C$), secondary decomposition takes place.

10. The experimental data of step-aged alloy was tested using fine particle theories (coherent notation, fanning and curling models). It was found that the fanning model is the lowest magnetization reversal mechanism. This is probably due to the fact that the Fe-Co rich particles in the step-aged alloy are described as having a "peanut shape" rather than a prolate spheroid shape.

ACKNOWLEDGMENTS

The author wishes to express his deepest gratitude to Professor Gareth Thomas for his guidance, encouragement, unending patience and support during the course of this work. He would like to thank Dr. Ronald Gronsky, Professor Jack Washburn and Professor S. Wang for their review and critical comments of this manuscript. Appreciation is also extended to Dr. Raja K. Mishra, Professor Motofumi Homma, Professor Hideo Kaneko, Dr. J. P. Jakubovics and Dr. M. J. Goringe for many helpful discussions.

The assistance of the support staff in the Materials and Molecular Research Division of the Lawrence Berkeley Laboratory is acknowledged. In particular, the author wishes to recognize Carolyn Gosnell, Gloria Pelatowski, Ed Edwards, Lee Johnson, and John Holthius. He is also thankful to Mr. Yalcin Belli, Mr. Chien Kuo Wu and Mr. Takehisa Minowa for their help in this research.

Finally, he gives the sincere thanks to his wife, Naoe and his parents for their patience and encouragement.

This research was performed under the auspices of the U. S. Department of Energy through the Materials and Molecular Research Division of the Lawrence Berkeley Laboratory.

APPENDIX I Modified Kersten Theory

Domain walls are positions of minimum energy, from which they may be displaced by the application of a magnetic field. Consider that the wall energy per unit area γ increases by $\Delta\gamma$ when the wall traverses a distance Δx; then by energy balance:

$$2HI_S\Delta x = \Delta\gamma \qquad \text{(A.1.1)}$$

where $2HI_S$ is the effective pressure exerted by the field. The left-hand side of this equation represents the magnetic energy, which is converted into surface energy of the domain wall. The threshold field Ho for the displacement of a boundary over the length of a domain will be determined by the largest local obstacle encountered in passage, thus:

$$Ho = \frac{1}{2I_S}\left(\frac{d\gamma}{dx}\right)_{max} \qquad \text{(A.1.2)}$$

The problem is now the estimation of $(d\gamma/dx)_{max}$.

Consider now the case where strongly magnetic particles (α_1) are imbedded within a weakly magnetic matrix phase (α_2). The domain wall will tend to lie within the weakly magnetic phase where the domain wall energy is lower. Therefore, the domain wall must pass a higher energy barrier (α_1 particle) during displacement over the length of a domain. Using a highly simplified model, a cubic array of spherical inclusions (α_1) of diameter d is assumed to exist in the α_2 matrix at a spacing λ, as shown in Fig. 58. When the domain wall intersects a sphere, the wall energy is increased by an amount corresponding to the energy in the wall area of the α_1 particles. The field required to pass the α_1 particles is the coercive force. For this model, there are two extreme cases, $d \gg \delta$ (wall thickness) and $d \ll \delta$.

(i) $d \gg \delta$

From a geometrical consideration, the wall energy is given by:

$$\gamma(x) = \frac{\gamma_2\lambda^2 - \pi(\gamma_2-\gamma_1)}{\lambda^2}[\frac{d^2}{4} - x^2] \qquad (A.1.3)$$

where γ_1 and γ_2 are the wall energy of the α_1 and α_2 phase, respectively, and $|x| \leq d/2$.

$$\frac{d\gamma}{dx} = \frac{2\pi(\gamma_2-\gamma_1)x}{\lambda^2} \qquad (A.1.4)$$

$$(\frac{d\gamma}{dx})_{max} = \frac{\pi(\gamma_1-\gamma_2)d}{\lambda 2} \qquad (A.1.5)$$

By substituting equation (A.1.5) into equation (A.1.2), the coercive force is:

$$Hc = \frac{\pi(\gamma_1-\gamma_2)d}{2 \quad I_s^2 \quad \lambda^2} \qquad (A.1.6)$$

Introducing the packing fraction (α) of the particles:

$$\alpha = \frac{\pi}{6}\frac{d^3}{\lambda^3} \qquad (A.1.7)$$

Then:

$$Hc = 2.4\frac{(\gamma_1-\gamma_2)}{I_s}\frac{\alpha^{2/3}}{d} \qquad (A.1.8)$$

Therefore,

$$Hc \simeq \frac{(\gamma_1-\gamma_2)\alpha^{2/3}}{I_s d} \qquad (A.1.9)$$

This is derived on the assumption that the inclusion diameter d is much greater than the wall thickness δ. Then the maximum value of Hc will occur when $\delta = d$.

(ii) $d \ll \delta$

The domain wall energy is expressed by:

$$\gamma(x) = \frac{\gamma_2 \lambda^2 - \pi/6\, d^3\, w(x)}{\lambda^2} \qquad \text{(A.1.10)}$$

where $w(x)$ is the energy per unit volume of the wall at a point x inside wall and is approximately given by:

$$w(x) = \frac{2(\gamma_2-\gamma_1)}{\delta}\left[1 \pm \frac{2x}{\delta}\right] \quad \text{for } |x| < \frac{1}{2}\delta \qquad \text{(A.1.11)}$$

$$\left(\frac{d\gamma}{dx}\right)_{max} = \frac{2\pi d^3 (\gamma_1-\gamma_2)}{3\delta^2\lambda^2} \qquad \text{(A.1.12)}$$

Then,

$$Hc = \frac{\pi}{3}\frac{(\gamma_1-\gamma_2)d^3}{I_s \delta^2 \lambda^2}$$

$$= \frac{1.6(\gamma_1-\gamma_2)d}{I_s \delta^2}\alpha^{2/3} \qquad \text{(A.1.13)}$$

$$Hc \simeq \frac{(\gamma_1-\gamma_2)d}{I_s \delta^2}\alpha^{2/3} \qquad \text{(A.1.14)}$$

This equation will be valid when the wall thickness δ is much greater than the particle diameter d. Hence the maximum value of Hc will occur when $\delta = d$. In such a case the equations (A.1.9) and (A.1.14) give the same form apart from a small numerical factor. Therefore, the maximum coercive force will be expected when $d \simeq \delta$, given by

$$(Hc)_{max} \simeq \frac{(\gamma_1-\gamma_2)}{I_s \delta}\alpha^{2/3} \qquad \text{(A.1.15)}$$

APPENDIX II Estimation of Magnetic Constants

(i) Domain wall energy

Domain wall energy is generally given by [55]

$$\gamma = 2\sqrt{\frac{JS^2\pi^2K}{a}}$$

Where, J: exchange integral

S: total quantum spin number

K: crystal anisotropy

a: lattice constant

J for the bcc lattice can be approximately related to the Curie temperature [139]

$$J = 0.15\ kTc \quad (S=1) \quad \text{where k: Boltzman constant}$$

$$\therefore \gamma = 2\sqrt{\frac{0.15kTc\pi^2K}{a}}$$

For example, the wall energy for Fe-33wt%Co alloy, with $K\sim 2.0\times10^5 ergs/cm^3$, $Tc=1273°K$ and $a=2.86Å$ is calculated as

$$\gamma = 2\pi\sqrt{\frac{0.15(1.38\times10^{-16})\times 1273\times 2.0\times10^5}{2.86\times10^{-8}}}$$

$$\simeq 2.7\,(ergs/cm^2)$$

(ii) Domain wall thickness

The domain wall thickness will be given by

$$\delta = \sqrt{\frac{JS^2\pi^2}{Ka}}$$

$$= \sqrt{\frac{0.15kTc\pi^2}{Ka}} \qquad \text{(for bcc, s=1)}$$

For example, the wall thickness of Fe-33wt%Co alloy will be,

$$\delta = \sqrt{\frac{0.15(1.38\times10^{-16}) \times 1273\pi^2}{2\times10^5 \times 1.86\times10^{-8}}}$$

$$\simeq 674\text{Å}$$

(iii) Exchange constant [139]

$$A = \frac{2JS^2}{a} = \frac{0.30kTc}{a} \qquad \text{(for bcc, s=1)}$$

For an Fe-33wt%Co alloy, A is given by

$$A = \frac{0.3 \times 1.38\times10^{-6} \times 1273}{2.86\times10^{-8}}$$

$$= 1.84\times10^{-6}\text{(ergs/cm)}$$

REFERENCES

1. H. Kaneko, M. Homma and K. Nakamura, A.I.P. Conf. Proc. 5, 1088 (1972).
2. H. Kaneko, M. Homma, K. Nakamura and M.Miura, I.E.E.E. Trans. Magnetics MAG-8, 347 (1972).
3. J. W. Cahn, Trans. AIME 242, 166 (1968).
4. J. E. Hilliard, in Phase Transformations, ASM (1970), p. 497.
5. D. deFontaine, in Ultrafine-Grain Metals, Syracuse Univ. Press (1970), p. 93.
6. H. Neumann, A. Büchner and H. Reinboth, Z. Metallk. 29, 173 (1937).
7. V. Daniel and H. Lipson, Proc. Roy. Soc. London 181A, 368 (1943).
8. A. Nagarajan and P. A. Flinn, Appl. Phys. Lett. 11, 120 (1967).
9. E. P. Butler and G. Thomas, Acta Met. 18, 374 (1970).
10. W. Dannöhl and H. Neumann, Z. Metallk. 30, 217 (1938).
11. W. G. Dorfeld and V. A. Phillips, Acta Met. 18, 955 (1970).
12. T. Mishima, Ohm 19, 353 (1932).
13. K. J. DeVos, in Magnetism and Metallurgy, A. E. Berkowitz and E. Kneller (eds) vol. 1, Academic Press (1969) p. 473.
14. H. Kaneko, M. Homma, K. Nakamura and S. Hoshi, unpublished work.
15. A. Higuchi, M. Kamiya and K. Suzuki, 3rd European Conf. Proc. on Hard Mag. Mat. Amsterdam, p. 201 (1974).
16. W. Wright, R. E. Johnson and P. L. Burkinshow, 3rd European Conf. Proc. on Hard Mag. Mat. Amsterdam, p. 197 (1974).
17. J. T. Song, J. Korean Inst. Metals 12, 250 (1974).
18. J. T. Song, J. Korean Inst. Metals 13, 267 (1975).
19. H. Kaneko, M. Homma, T. Fukunaga and M. Okada, I.E.E.E. Trans. Magnetics MAG-11, 1440 (1975).

20. M. McCaig, I.E.E.E. Trans. Magnetics MAG-11, 1443 (1975).

21. T. Miyamoto, J. of Japan Inst. Metals 40, 111 (1976) (in Japanese).

22. T. Miyamoto, J. of Japan Inst. Metals 42, 41 (1978) (in Japanese).

23. H. Kaneko, M. Homma and T. Minowa, I.E.E.E. Trans. Magnetic MAG-12, 177 (1977).

24. H. Kaneko, M. Homma, M. Okada, S. Nakamura and N. Ikuta, A.I.P. Conf. Proc. 29, 620 (1975).

25. G. Y. Chin, J. T. Plewes and B. C. Wonsiewicz, J. Appl. Phys. 49, 2046 (1978).

26. W. Köster, Arch Eisenhuettenw 6, 113 (1932).

27. S. Rideout, W. D. Manly, E. L. Kamen, B. S. Lement and P. A. Beck, Trans.AIME 191, 872 (1951).

28. W. Köster and G. Hofman, Arch Eisenhuettenw 30, 249 (1959).

29. R. O. Williams, Trans. AIME 212, 497 (1958).

30. R. M. Fisher, E. D. Dulis and K. G. Carroll, Trans. AIME 197, 690 (1953).

31. E. Z. Vintaikin and A. A. Loshmanov, Phys. Met. Metallography 22, 475 (1966).

32. M. J. Marcinkowski, R. M. Fisher and A. Szirmae, Trans. AIME 230, 676 (1964).

33. Y. Imai, M. Izumiyama and T. Masumoto, Sci. Rep. Res. Inst., Tohoku University, Ser. A 18, 56 (1966).

34. R. Lanelorg, Trans. ASM 60, 67 (1967).

35. E. Z. Vintaikin, V. B. Dimitriev and V. Yu. Kolonstsov, Fiz. Metal. Metalloved 27, 1131 (1969).

36. H. Yamamoto, Japanese J. Appl. Phys. 3, 745 (1964).

37. H. Ettwig and W. Pepperhoff, Archiv Eisenhuettenw 41, 471 (1970).

38. D. Chandra and L. H. Schwarts, Met. Trans. A 2, 511 and 2294 (1971).

39. T. DeNys and P. M. Gielem, Met. Trans. 2, 1423 (1971).

40. D. Coutsouradis, in Cobalt Containing High Strength Steels, Cobalt Information Center (1974) p. 91.

41. D. Coutsouradis, J. M. Drapier, E. Diderrich and L. Habraken, Cobalt 36, 144 (1967).

42. D. J. Abson and J. A. Whiteman, J. of Iron and Steel Inst. 208, 594 (1970).

43. H. Kaneko, M. Homma, K. Nakamura, M. Okada and G. Thomas, I.E.E.E. Trans. Magnetic MAG-13, 1325 (1977).

44. M. Hansen, Constitution of Binary Alloys, 2nd Ed. McGraw Hill, (1958), p. 472.

45. P. Vigoureux and C. E. Webb, in Principles of Electric and Magnetic Measurements, Prentice-Hall (1937), p. 392.

46. N. F. Artbury, The Institute of Physics, 132 (1952).

47. R. L. Sanford and L. I. Cooter, in Basic Magnetic Quantities and the Measurement of the Magnetic Properties of Materials, National Bureau of Standard Monograph, 1962.

48. H. Ziglstra, Experimental Methods in Magnetism, vol. 2, John Wiley, (1967).

49. V. Dahiel and H. Lipson, Proc. Roy. Soc. (A) 182, 378 (1944).

50. D. R. Clarke, J. of Mater. Science 10, 172 (1975).

51. R. W. Horne and R. Markham, in Practical Methods in Electron Microscopy, A. M. Glanert (ed), vol. 1, Elsevier, N. Y. (1972), p. 327.

52. R. Sinclair, R. Gronsky and G. Thomas, Acta Met. 24, 789 (1976).

53. S. G. Lipson and H. Lipson, Optical Physics, Cambridge University Press, London (1969).

54. F. Bitter, Phys. Rev. 38, 1903 (1931).

55. S. Chikazumi, Physics of Magnetism, John Wiley (1964).

56. P. B. Hirsch, A. Howie, R. B. Nicholson, D. W. Pashley and M. J. Whelan, Electron Microscopy of Thin Crystals, Butterworths, London (1965).

57. J. P. Jackubovics, in Electron Microscopy in Materials Science, Part lV, Commission of the European Communities (1975).

58. H. Kaneko, M. Homma, K. Nakamura and R. Takeda, unpublished work.

59. M. Bouchard and G. Thomas, Acta Met. 23, 1485 (1975).

60. B. G. Bergman and D. P. Shoemaker, Acta Cryst. 5, 157 (1952), 7, 857 (1954).

61. G. J. Dickins, A. M. B. Douglas and W. H. Taylar, J. Iron Steel Inst. 167, 27 (1951).

62. G. J. Dickins, A. M. B. Douglas and W. H. Taylar, Acta Cryst. 9, 297 (1956).

63. S. H. Algie and E. O. Hale, Acta Cryst. 20, 142 (1966).

64. I. M. Lifshitz and V. V. Slyozov, J. Phys. Chem. Solids 19, 35 (1961).

65. C. Wagner, Z. Electrochem 65, 58 (1961).

66. K. Bungardt, W. Spyra and G. Lennartz, in Steel-Strengthening Mechanism, Climax Molybenum, Zurich (1970), p. 97.

67. M. Okada, M. Homma, H. Kaneko and G. Thomas, 34th Ann. Proc. EMSA p. 606 (1976).

68. H. Kaneko, M. Homma and K. Nakamura, unpublished work.

69. K. Kubarych, M. Okada and G. Thomas, Trans. AIME, in press.

70. M. G. Luzhinskaya, N. F. Shilova and YA. S. Shur, Fiz. Metal. Metalloved 40, 748 (1975).

71. Y. Belli, M. Okada, G. Thomas, M. Homma and H. Kaneko, J. App. Phys. 49, 2049 (1978).

72. J. W. Cahn, Acta Met. 14, 477 (1966).

73. J. W. Cahn, J. Chem. Phys. 42, 93 (1965).

74. W. B. Person, Lattice Spacing and Structure of Metals and Alloys, Pergamon Press (1958).

75. L. M. Magat, G. V. Ivanova, T. P. Lapiha, L. V. Solina and YA. S. Shur, Phys. of Metal. and Metallography 40, 43 (1975).

76. H. E. Cook and J. E. Hilliard, Trans. Met. Soc. AIME 233, 142 (1965).

77. M. Ko and T. Nishizawa, Trans. JIM 16, 369 (1975).

78. T. Nishizawa, M. Hasche and M. Ko, to be published.

79. A. J. Ardell, R. B. Nicholson and J. D. Eshelby, Acta Met. 14, 1295, 1306 (1966).

80. H. Gleiter and E. Hornbogen, Mater. Scie. Eng. 2, 285 (1968).

81. A. Kelly and R. B. Nicholson, in Progress in Materials Science, vol. 10, Permagon Press, Oxford (1963), p. 149.

82. L. H. Schwartz, S. Mahajan and J. T. Plewes, Acta Met. 22, 601 (1974).

83. D. E. Laughlin, Acta Met. 24, 53 (1976).

84. P. E. J. Flewitt, Acta Met. 22, 47 (1974).

85. R. J. Livak and G. Thomas, Acta Met. 19, 497 (1971).

86. E. S. Pundarika, K. Hanson and J. W. Morris, Jr., LBL #6613, University of California, Berkeley (1977).

87. M. V. Smoluchowski, Phy. Z. 17, 385 (1916).

88. K. Binder, M. H. Kalos, J. L. Lebowits and J. Marro, in Nucleation, A. C. Zettlemoyer (ed.), M. Dekker, New York (1969).

89. A. J. Ardell, Acta Met. 20, 61 (1972).

90. K. Hirano and M. Cohen, Trans. JIM 13, 96 (1972).

91. D. W. James and G. M. Leak, Phil. Mag. 14, 701 (1966).

92. S. P. Ray and B. D. Sharna, Acta Met. 16, 981 (1968).

93. B. J. Borg and C. E. Birchenall, Trans. Am. Inst. Min. Metal. Engrs. 281, 980 (1960).

94. B. J. Borg and D. Y. F. Lai, Acta Met. 11, 861 (1963).

95. K. Hirano, R. P. Agarwala, B. L. Averbach and M. Cohen, J. Appl. Phys. 33, 3049 (1962).

96. J. Kucera, B. Million, J. Ruzickova, V. Foldyna and A. Jakobava, Acta Met. 22, 135 (1974).

97. R. Tahara, Y. Nakamura, M. Inagaki and Y. Iwama, Proc. Internat. Conf. Mössbauer Spectroscopy, vol. 1, Cracow, p. 107 (1975).

98. R. Tahara, Y. Nakamura, M. Inagaki and Y. Iwama, Phys. Stat. Sol. (a) 41, 451 (1977).

99. YE. Z. Vintaykin, G. G. Vrushadze, I. S. Belyatskaya and YE. A. Sukharova, Phys. of Metals and Metallography 38, 102 (1974).

100. E. O. Hall and S. H. Algie, Met. Review 11, 104 (1966).

101. C. Tucker, Acta Cryst. 4, 425 (1951).

102. W. J. Kichingman, Acta Cryst. A24, 282 (1968).

103. S. Nenno, M. Tagaya, K. Hosomi and Z. Nishiyama, Trans. JIM 4, 222 (1963).

104. R. D. Heidenreich and E. A. Nesbitt, J. Appl. Phys. 23, 352,366 (1952).

105. C. D. Graham,in Magnetic Properties of Metals and Alloys, ASM, Ohio, (1958), p. 288.

106. C. Kittel, E. A. Nesbitt and Shockley, Phys. Rev. 77, 839 (1950).

107. H. Ziglstra, J. Appl. Phys. 32, 194S (1961).

108. J. W. Cahn, J. Appl. Phys. 34, 3581 (1963).

109. R. Cremer and I. Pfeiffer, Physica 80B, 164 (1975).

110. V. Daniel, Proc. Roy. Soc. 192, 575 (1947).

111. C. P. Bean and J. D. Livingston, J. Appl. Phys. 30, 120S (1959).

112. P. G. Shewmon, in Transformation in Metals, McGraw-Hill (1969), p. 159.

113. E. A. Nesbitt and H. J. Williams, Phys. Rev. 80, 112 (1950).

114. A. Kussmann and J. H. Wollenberger, Z. Angrew. Phys. 8, 213 (1956).

115. W. Andrä, Ann. Phys. 19, 10 (1956C).

116. L. F. Bates, D. J. Craik and E. D. Issac, Proc. Phys. Soc. 79, 970 (1962).

117. D. J. Craik and E. D. Issac, Proc. Phys. Soc. 76, 16 (1960).

118. Y. Iwama, Trans. JIM 9, 273 (1968).

119. M. Kersten, Grundlagen einer Theoric der Ferromagnetishen Hysterese und der Koerzitivkraft. (S. Hirzel, Leipzig; reprinted, J. W. Edwards, Ann Arbor, 1943).

120. I. Neel, Annales Univ. Grenoble 22, 299 (1946).

121. L. J. Dijkstra and C. Wert, Phys. Rev. 79, 979 (1950).

122. E. C. Stoner and E. P. Wohlfarth, Phil. Trans. Roy. Soc. A-240, 599 (1948).

123. R. C. Hall, J. Appl. Phys. 31, 157S (1960).

124. A. H. Morrish, The Physical Principles of Magnetism, Wiley (1965).

125. I. S. Jacobs and C. P. Bean, Phys. Rev. 100, 1060 (1955).

126. W. F. Brown, Jr., J. Appl. Phys. 30, 625 (1959).

127. E. H. Frei, S. Shtrikman and D. Treves, Phys. Rev. 106, 446 (1957).

Table I. Chemical compositions of the alloys studied.

Alloy Number	Nominal Composition	Composition (wt%) Fe	Cr	Co	C	N
A	Fe-16Cr-28Co	Bal	16.03	28.45	0.003	0.009
B	Fe-31Cr-23Co	Bal	30.73	23.39	0.007	0.006
C	Cr-26Fe-13Co	Bal	59.81	12.95	0.001	0.064

Table II. Rate consant (K) measured for growth of modulations.

Temp(°C)	(°K)	$\frac{1}{T}(^{o}K)^{-1}$	K(Å/(hr)$^{1/3}$)	K^3
640	873	1.145×10^{-3}	45	8.9×10^{4}
620	893	1.198×10^{-3}	116	1.5×10^{6}
600	913	1.095×10^{-3}	229	1.2×10^{7}

Table III. Magnetic properties of the alloy B after thermomagnetic treatment and step aging.

No.	Heat Treatment		$4\pi I_s$ (kG)	B_r (kG)	$_BH_c$ (Oe)
1	640°C TMT	20 min	12.4	7.7	40
2	640°C TMT	40 min	12.4	10.6	130
3	640°C TMT	1 hr	12.0	10.9	140
4	640°C TMT	3 hr	11.0	9.2	170
5	640°C TMT	5 hr	11.0	8.4	170
6	No. 2 + 620°C	20 min	12.4	11.0	325
7	No. 2 + 620°C	1 hr	12.4	11.0	350
8	No. 2 + 620°C	3 hr	12.4	10.6	285
9	No. 2 + 600°C	20 min	13.3	12.3	250
10	No. 2 → Furnance cool → 600°C	20 min	12.6	11.2	345
11	No. 2 + 600°C	1 hr	13.3	11.7	305
12	No. 2 + 600°C	3 hr	13.3	11.5	375
13	No. 2 + 580°C	20 min	13.5	11.4	130
14	No. 2 → Furnance Cooling → 580°C	20 min	13.0	11.0	348
15	No. 2 + 580°C	1 hr	13.5	11.6	175
16	No. 6 + 600°C	1 hr	13.0	11.4	410
17	No. 16 + 580°C	1 hr	13.7	12.6	460
18	640°C (without TMT)	40 min	12.4	6.4	120
19	No. 18 + 620°C	20 min	12.5	7.3	310
20	No. 19 + 600°C	1 hr	13.3	9.1	400

Table IV. Approximate equilibrium compositions of two phases.

Temp(°C)	Fe-Co rich phase(wt%)	Cr-rich phase
640	Fe-30Co-8Cr	Cr-16.5 Co-33.5Fe
620	-31Co-5Cr	-13Co-26Fe
600	-32Co-3Cr	-10Co-21Fe
580	-33Co-2Cr	-8Co-17Fe

Table V. Magnetic constants used for numerical calculations.

Magnetic Constant		Fe-33wt%Co	Cr-50%(Fe-33Co)
Crystal anisotropy	$K(erg/cm^3)$	2.0×10^5 [123]	$(4.4 \times 10^5)^{**}$
Saturation magnetization	$\sigma(emu/g)$	238 [135]	80 [136]
Density	$\rho(g/cm^3)$	8.0 [147]	7.5
Saturation magnetization	$\sigma(emu/cm^3)$	1900	600
Curie temperature	$Tc(^oC)$	1000 [138]	(285)**
Lattice constant	$a(10^{-8}$ cm)	2.856 [74]	2.868 [74]
Wall thickness	$\delta(10^{-8}$ cm)	675*	(300)**
Wall energy	$\gamma(erg/cm^2)$	2.7*	2.64*

**Estimated from the present experimental data.

*Calculated.

FIGURE CAPTIONS

Fig. 1. Demagnetized curves of various Fe-Cr-Co magnets in comparison with those of commercial ductile magnets.

Fig. 2. Isothermal sections of iron-chromium-cobalt system according to Köster, et al.[26], and Rideout, et al[27].

Fig. 3. (a) Miscibility gap of an α phase in Fe-Cr-Co system.
(b) Vertical sections of the miscibility gap along the conjugate lines A, B, C and D shown in Fig. 3(a).

Fig. 4. Vertical section of the miscibility gap along the conjugate line A shown in Fig. 3(a)

Fig. 5. Electron micrographs of the as-quenched alloy A, showing the dislocated lath martensites are twin-related.
(a) Bright field, (b) SAD of (a), (c) dark field of $(0\bar{1}1)_T$ twin spot and (d) of $(0\bar{1}1)$ spot.

Fig. 6. The as quenched alloy B (31Cr-23Co) exhibits the σ phase,
(a) bright field image and (b) dark field of (003) spot of σ phase.

Fig. 7. Phase relations of an Fe-31Cr-23Co alloy vs. cooling rate, showing that the critical cooling rate to obtain an α single phase is over 100°C/sec.

Fig. 8. Bright field micrographs of the alloy B aged for 1 hr. at,
(a) 680°C, (b) 670°C, (c) 660°C and (d) 650°C.

Fig. 9. Bright field micrographs of the alloy B at 640°C for,
(a) 3 min, (b) 20 min, (c) 2 hr and (d) 20 hr.

Fig. 10. Satellites around (002) reflections in the corresponding electron diffraction patterns if Fig. 9.

Fig. 11. Micrographs of the alloy B aged at 600°C for (a) 2 min., (b) 2 hr, (c) 100 hr and (d) 500 hr.

Fig. 12. (110) lattice image (a) and corresponding laser optical diffraction pattern (b) of the alloy aged at 660°C for 1 hr showing two phases are coherent.

Fig. 13. Diffraction patterns of the σ phase. (a) $\bar{1}$100) (b) (001).

Fig. 14. Bright field micrographs of the alloy B aged at 640°C for (a) 50 hr and (b) 100 hr.

Fig. 15. Micrograph of the alloy B aged at 600°C for 500 hr. (a) Bright field micrograph, (b) higher magnification micrograph of (a), (c) dark field micrograph of (b) imaged with the σ phase spot.

Fig. 16. Micrograph of the alloy B aged at 670°C for 1 hr, showing the σ phase precipitated in a row within a grain. (a) Bright field micrograph, (b) dark field micrograph of (a), imaged with the σ phase spot and (c) higher magnification micrograph of (a).

Fig. 17. Micrograph of the alloy B aged at 640°C for 20 min, showing the Widmanstätten type of σ phases formed during quenching.

Fig. 18. Log-log plot of wavelength against aging time determined for alloy B.

Fig. 19. Plot of the wavelength against $(\text{time})^{1/3}$.

Fig. 20. A plot of log K^3 vs. 1/T.

Fig. 21. The magnetization as a function of temperature of the alloy B aged at 640°C.

Fig. 22. Curie temperature of the Cr-rich phase of the alloy B aged at various temperatures as a function of aging time.

Fig. 23. Bright field micrographs of the alloy A aged at 640°C for (a) 20 min and (b) 20 hr.

Fig. 24. Bright field micrographs of the alloy A aged at 600°C for (a) 2 min, (b) 20 min and (c) 200 hr.

Fig. 25. Bright field micrographs of the alloy A aged at 640 C°for (a) 40 min, (b) 5 hr and (c) 20 hr.

Fig. 26. Electron micrographs of the alloy A aged at 640°C for 20 hr. (a) Bright field micrograph, (b) dark field of the martensite $g = (10\bar{1})M$, and (c) SAD of (a).

Fig. 27. Bright field of micrographs of the alloy A aged at 640°C for 20 hr, showing that the dark phases are heavily dislocated martensites.

Fig. 28. Electron micrographs of the alloy A aged at 640°C for 40 min, showing the decomposed matrix and ε phases with fine striations due to stacking faults. (a) Bright field micrograph, (b) SAD of (a) and (c) dark field of faulted ε phase.

Fig. 29. Bright field micrograph of the alloy A aged at 640°C for 200 hr, showing the dislocated martensite of order of $\sim$1.5μm wide.

Fig. 30. Bright field micrographs of the alloy C aged for 20 hr, at (a) 620°C, (b) 600°C and (c) 580°C, showing the miscibility gap of the alloy C is below 620°C.

Fig. 31. Bright field micrographs of the alloy C aged for 200 hr, at (a) 600°C and (b) 580°C.

Fig. 32. Curie temperatures of the Cr-rich phase of the alloy C aged at 600°C as a function of aging time.

Fig. 33. Bright field micrographs of the alloy B aged at 640°C in a magnetic field of 2 kOe for (A) 20 min, (B) 1 hr, and (C) 3 hr, and their corresponding laser optical diffraction pattern (a), (b) and (c).

Fig. 34. Bright field micrographs (a) parallel (axial surface) and (b) perpendicular (basal surface) to the magnetic field direction, of the alloy B aged at 640°C for 40 min.

Fig. 35. Bright field micrograph taken from the alloy magnetically-aged at 640°C for 3 hr localized deviation in particle alignment is shown at M.

Fig. 36. Bright field micrograph of the alloy B aged at 640°C for 5 hr. in a magnetic field.

Fig. 37. Variation of the particle size of the alloy B vs. aging time of thermomagnetic treatment.

Fig. 38. Variation of magnetic properties of the alloy B vs. applied magnetic field strength.

Fig. 39. (a) Micrograph of the alloy B aged at 640°C for 40 min in a magnetic field of 2 kOe Hc $\sim$ 130 Oe. (b) Micrograph of the alloy B step-aged at 620°C for 20 min, and 600°C for 1 hr after thermomagnetic treatment, Hc $\sim$ 410 Oe.

Fig. 40. Variation of the Curie temperatures of the α_2 phase vs. step-aging time.

Fig. 41. Bright field micrographs taken from the alloy B aged at 600°C for (a) 20 min, (b) 1 hr and (c) 3 hr. after thermomagnetic treatment, showing the secondary decomposition.

Fig. 42. Bright field micrographs taken from the alloy B aged at 580°C for (a) 20 min and (b) 1 hr after the thermomagnetic treatment, showing the finer secondary particles appears at lower aging temperature.

Fig. 43. Variation of the magnetic properties of the isothermally aged alloy A vs. aging time.

Fig. 44. Variation of the magnetic properties of the isothermally aged alloy B vs. aging time.

Fig. 45. Variation of the magnetic properties of the isothermally aged alloy C vs. aging time.

Fig. 46. Typical magnetic hysteris loops A, B, C and D corresponding to the different heat-treatments.

Fig. 47. Domain structures of the alloy B aged (a) at 640°C for 40 min (b) 620°C for 100 hr and (c) at 600°C for 50 hr.

Fig. 48. Domain pattern of the alloy B (a) after thermomagnetic treatment and (b) followed by step-aging, showing that easy magnetization direction is close to one of the applied magnetic field.

Fig. 49. Fresnel [(a), (b)] and Foucault micrographs [(c), (d)] of the alloy B aged at 640°C for 20 min.

Fig. 50. Foucault [(a), (b)] and Fresnel micrographs [(c), (d)] of the alloy B aged at 600°C for 100 hr.

Fig. 51. Fresnel [(a), (b)] and Foucault micrographs [(c), (d)] on the axial surfaces of the step-aged alloy.

Fig. 52. Foucault micrographs on the axial surfaces of the step-aged alloy, showing that the domains are elongated to the direction of the applied magnetic field, independently on the crystal orientation.

Fig. 53. The miscibility gap of Fe-Cr-Co system, showing the chemical spinodal.

Fig. 54. Bright field micrograph of the Fe-23Cr-15Co-5V alloy aged at 650°C for 1 hr in a magnetic field, followed by continuous cooling at a rate of 1°C/min. to 540°C.

Fig. 55. Bright field of micrograph of Fe-28Cr-15Co-1Nb-1Al alloy at 640°C in a magnetic field of 2 kOe, showing the ferromagnetic particles are elongated along the direction of the magnetic field, independently of crystal orientation. (a) Parallel to magnetic field, A: [111] B: [110] orientation, (b) normal to magnetic field [110] foil.

Fig. 61. The schematic illustration of (a) normal order and (b) the directional order in Fe-Co rich particle.

Fig. 56. Schematic illustration of observation of the magnetic interaction domains by out-of-focus method, showing that incident electron beams are deviated in opposite directions in adjacent interaction domains, leading to a deficiency of electrons at A, and an excess at B, which appear to be imaginary domain walls.

Fig. 57. The variation of the coercive force of the alloy B, vs. (aging time)$^{1/3}$.

Fig. 58. Model for the calculation of coercive force on Kersten impurity center theory.

Fig. 59. Powder patterns of the alloy A, (a) in the as-quenched state, aged at 640°C for (b) 20 min, (c) 20 hr and (c) 100 hr.

Fig. 60. Critical diameter for single domain behavior vs. the axial ratio ($m = l/d$) of the Fe-Co particle.

Fig. 61. Schematic representation of magnetization revealing aligned chain or particles. Prolate spheroid model: a - coherent rotation mechanism; d - curling mechanism. Chain-of-Spheres model: b - symmetrical fanning mechanism; c - parallel rotation mechanism.

Fig. 62. Coercive force calculated by curling mode vs. diameter of the particle with varying axial ratio m.

Fig. 63. Coercive force expected by coherent rotation, symmetrical fanning, and curling vs. diameter of the particle in comparison with the experimental data.

Fig. 64. SEM fractograph taken from alloy B in the as-quenched state, showing a mixture of ductile and cleavage fracture modes.

Fig. 65. SEM fractograph taken from the alloy C in the as-quenched state, showing the cleavage fracture.

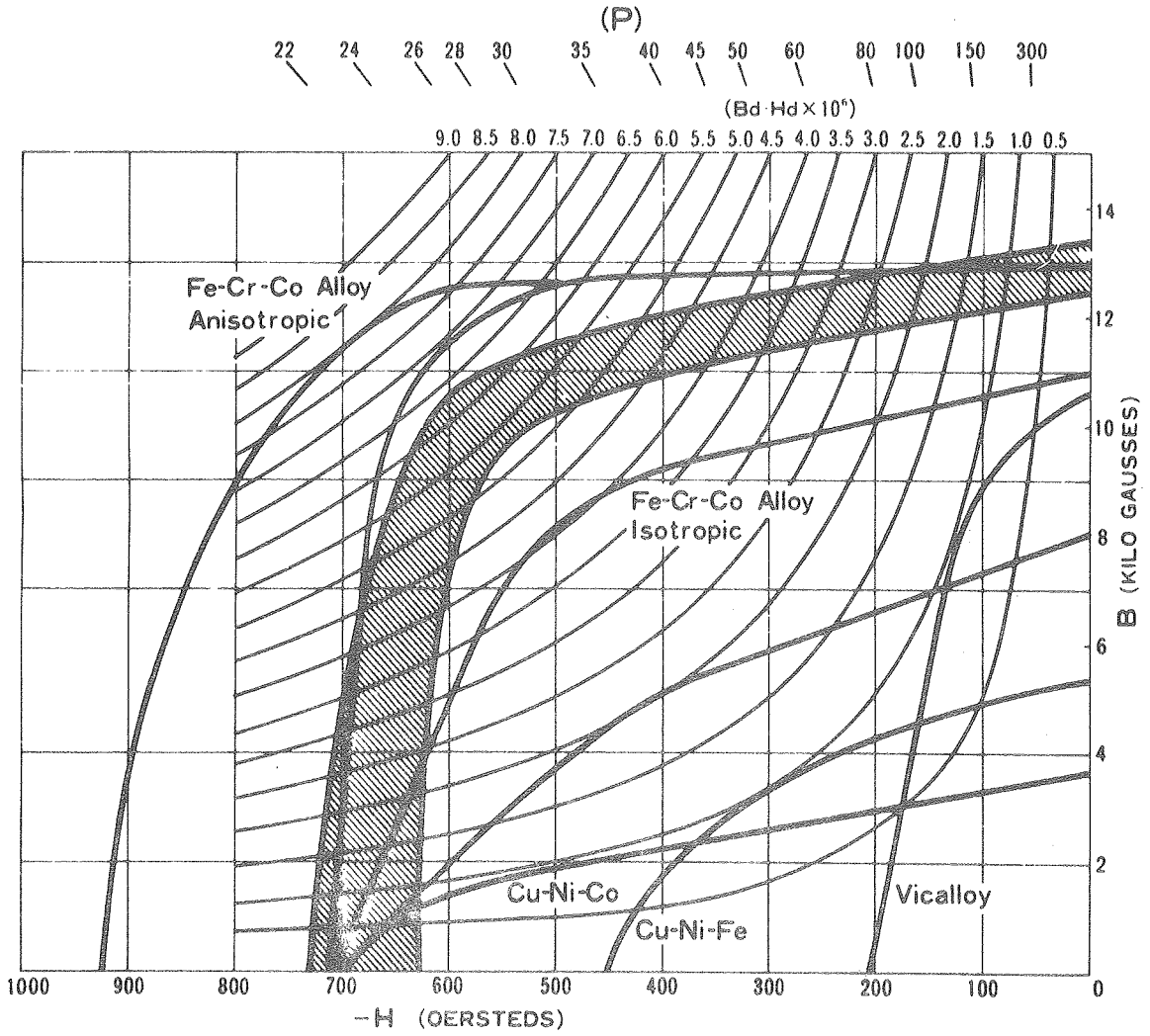

XBL 781-6968

Fig. 1

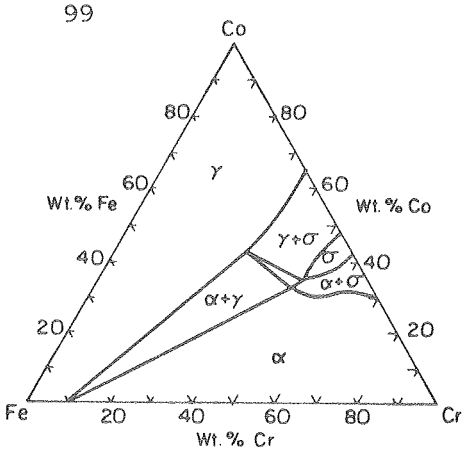

(a) 1200°C

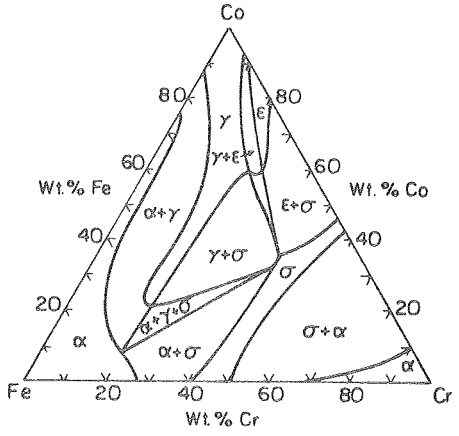

(b) 700°C

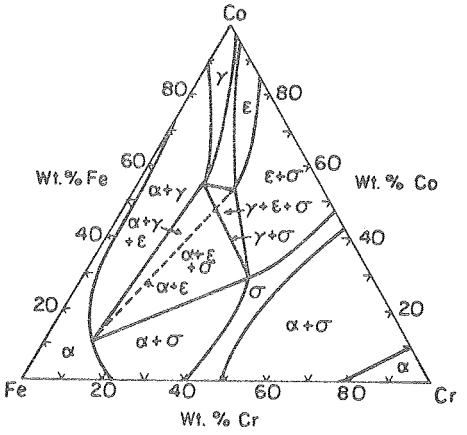

(c) 600°C

XBL 782-4566

Fig. 2

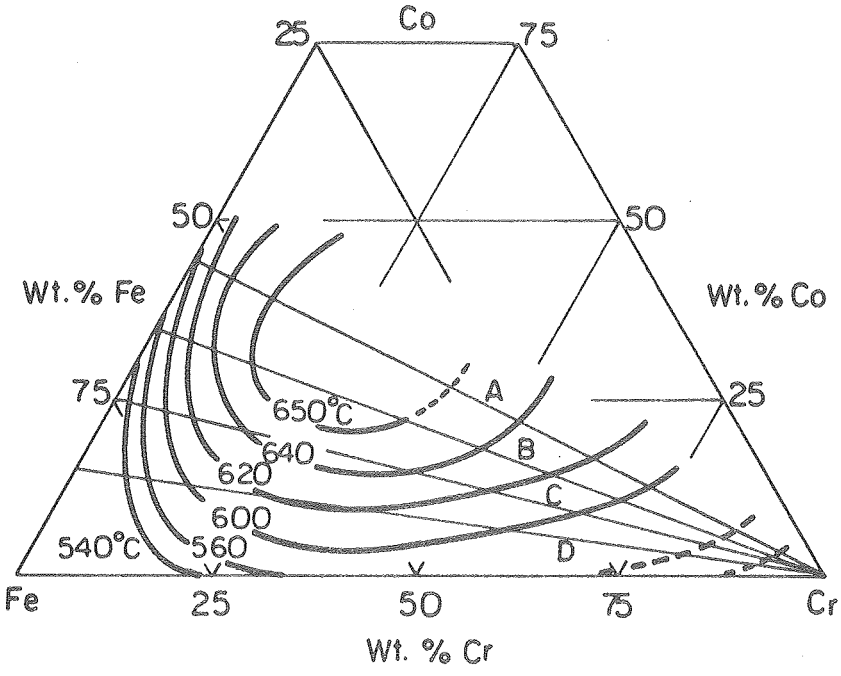

(a)

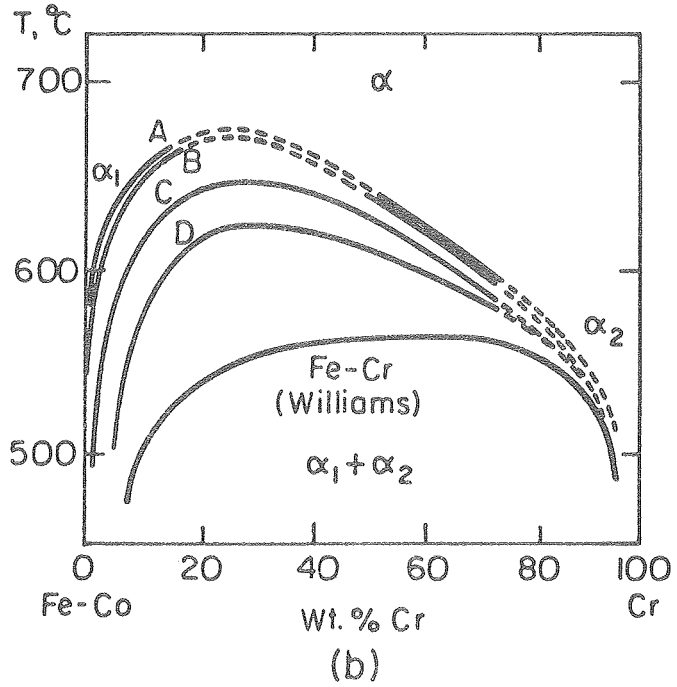

(b)

XBL782-4564

Fig. 3

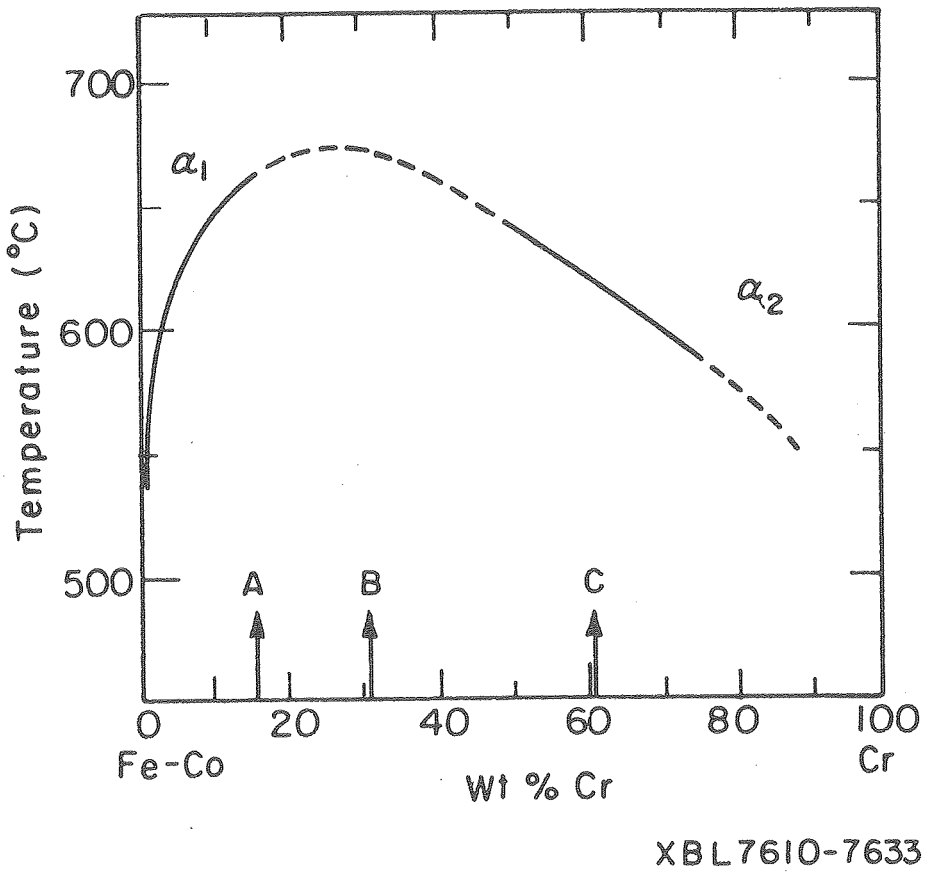
700
600
500
Temperature (°C)
α_1
α_2
A
B
C
0
20
40
60
80
100
Fe-Co
Cr
Wt % Cr
XBL7610-7633

Fig. 4

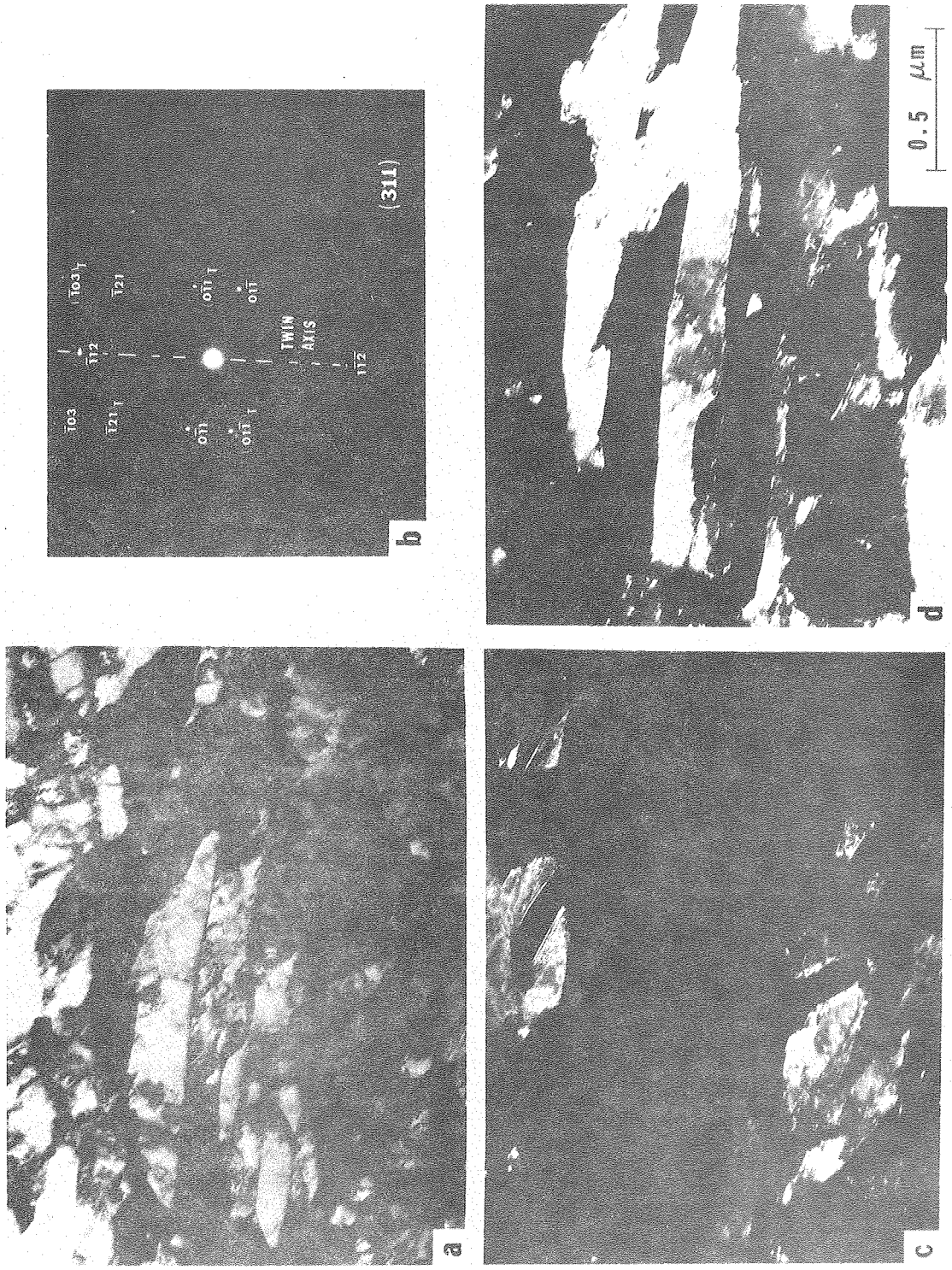

XBB 781-661

Fig. 5

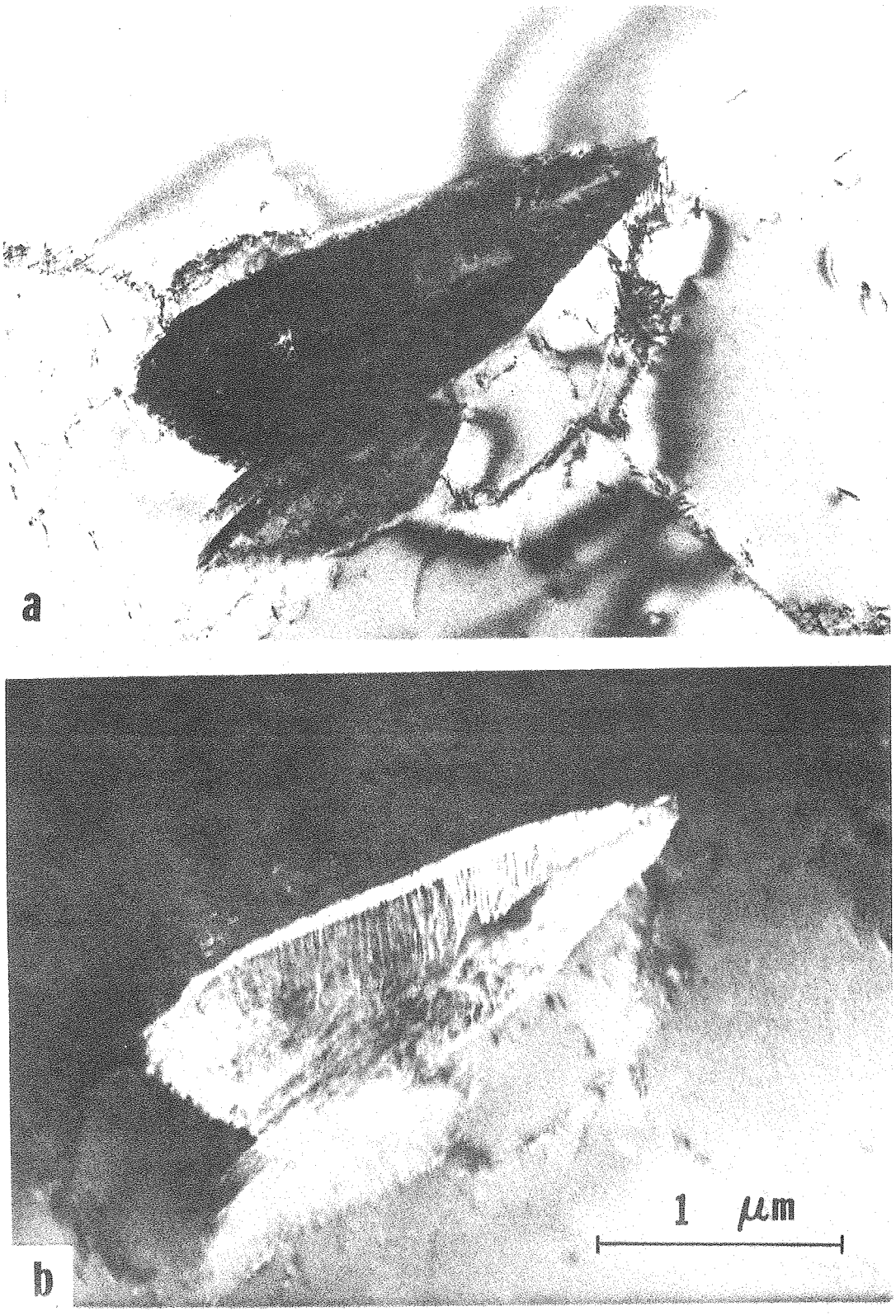

XBB 7612-11937

Fig. 6

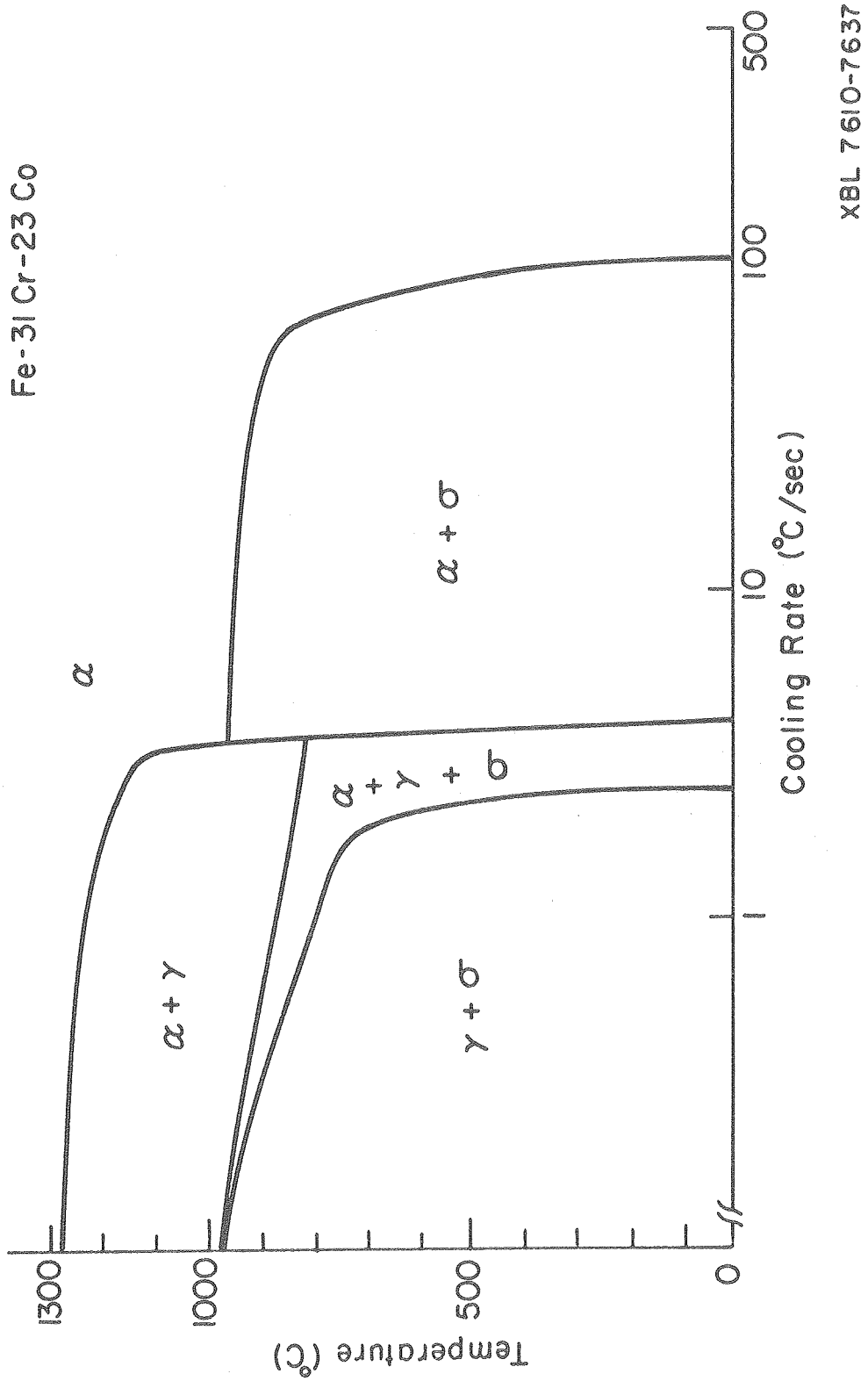
Fe-31 Cr-23 Co
α
α + γ
α + γ + σ
α + σ
γ + σ
Temperature (°C)
1300
1000
500
0
Cooling Rate (°C/sec)
1
10
100
500
XBL 7610-7637

Fig. 7

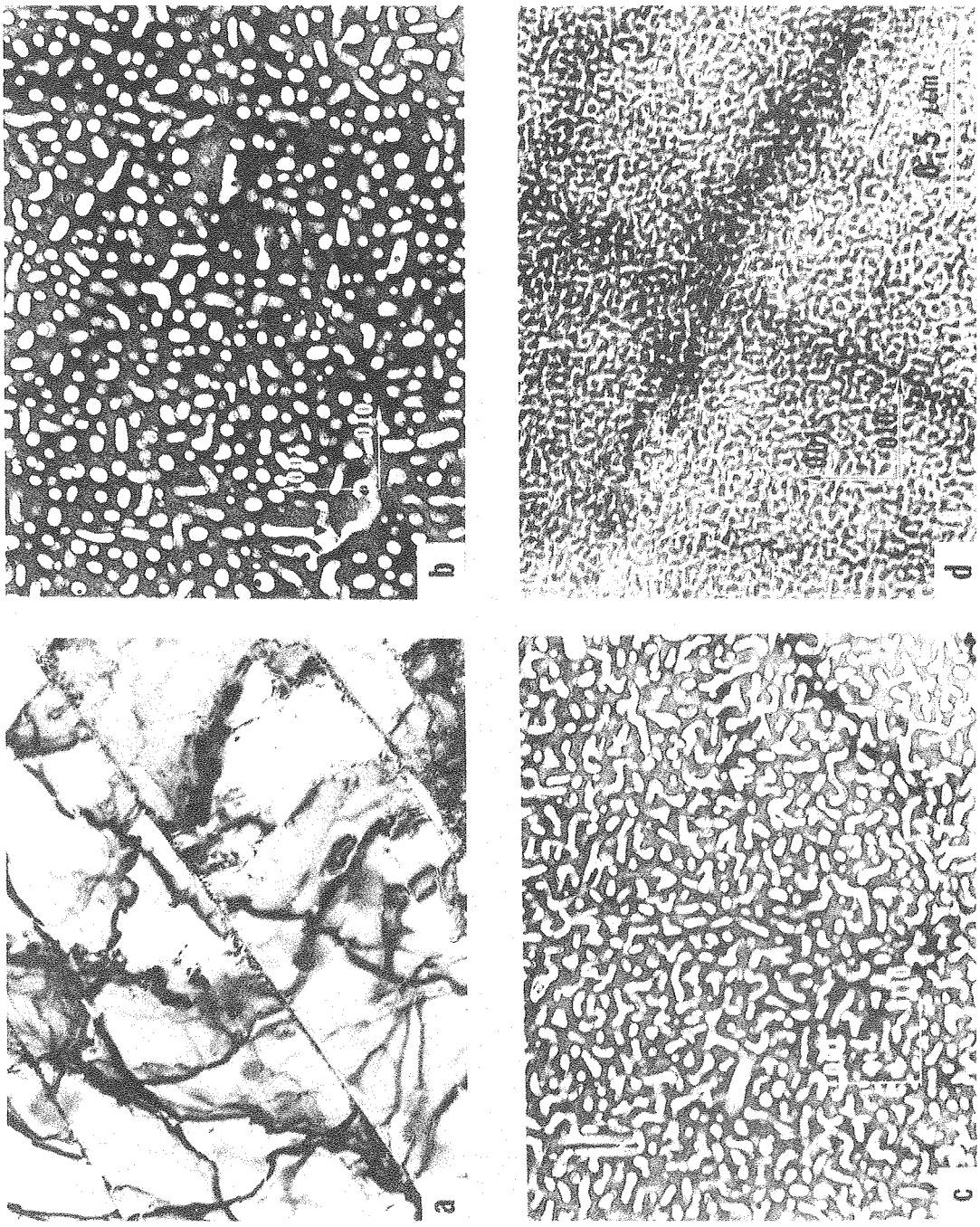

XBB 769-8660

Fig. 8

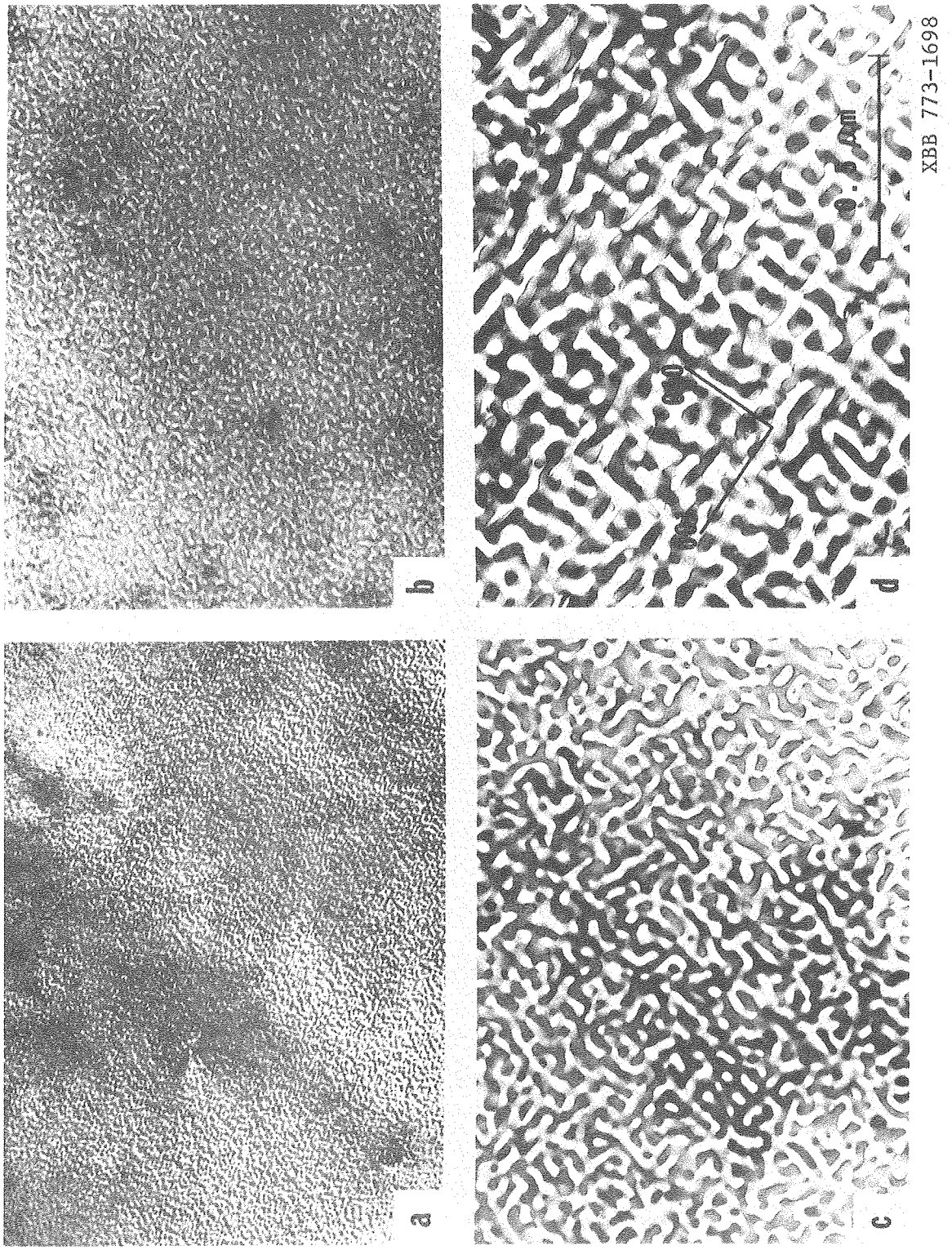

Fig. 9

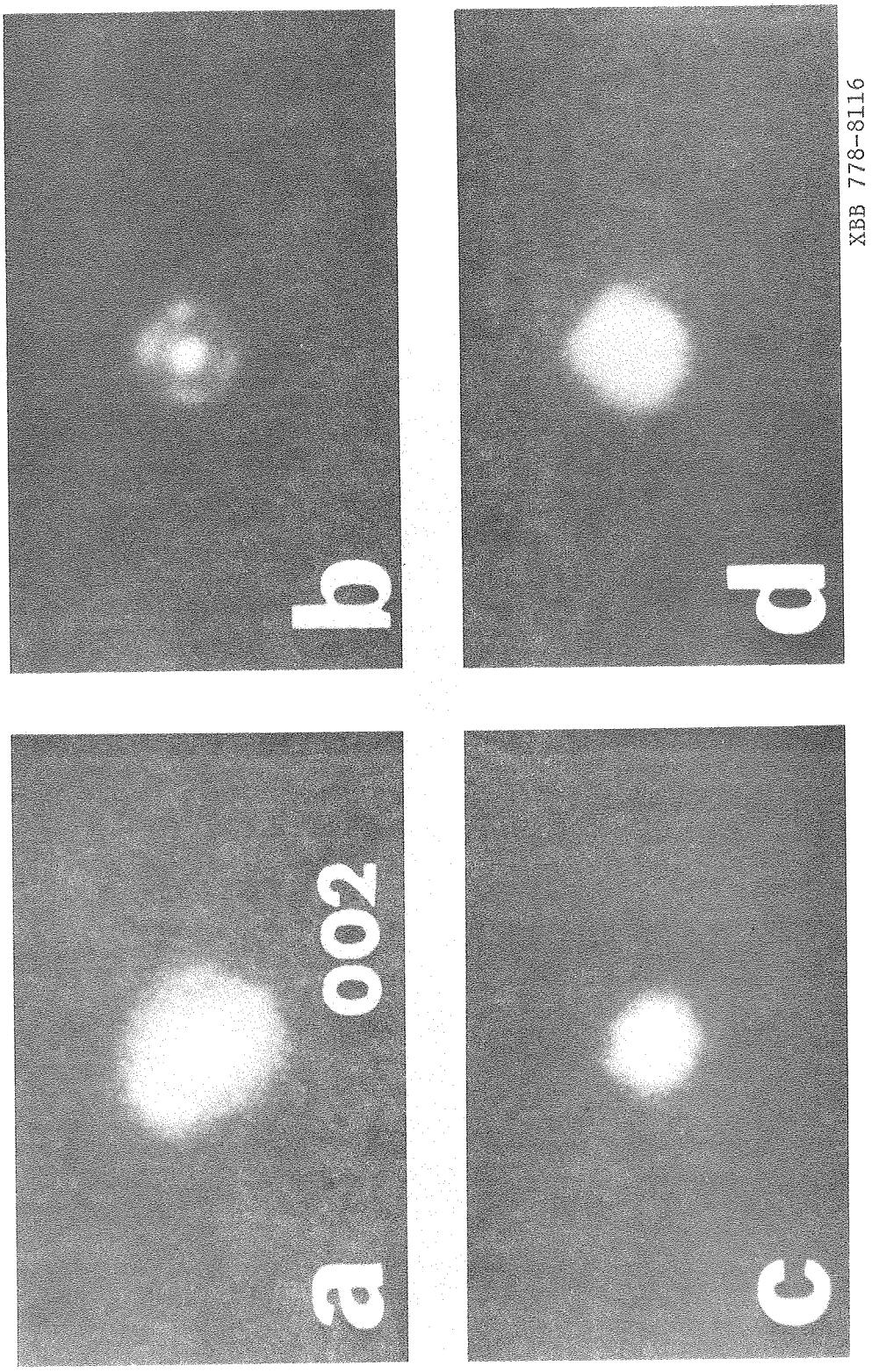

XBB 778-8116

Fig. 10

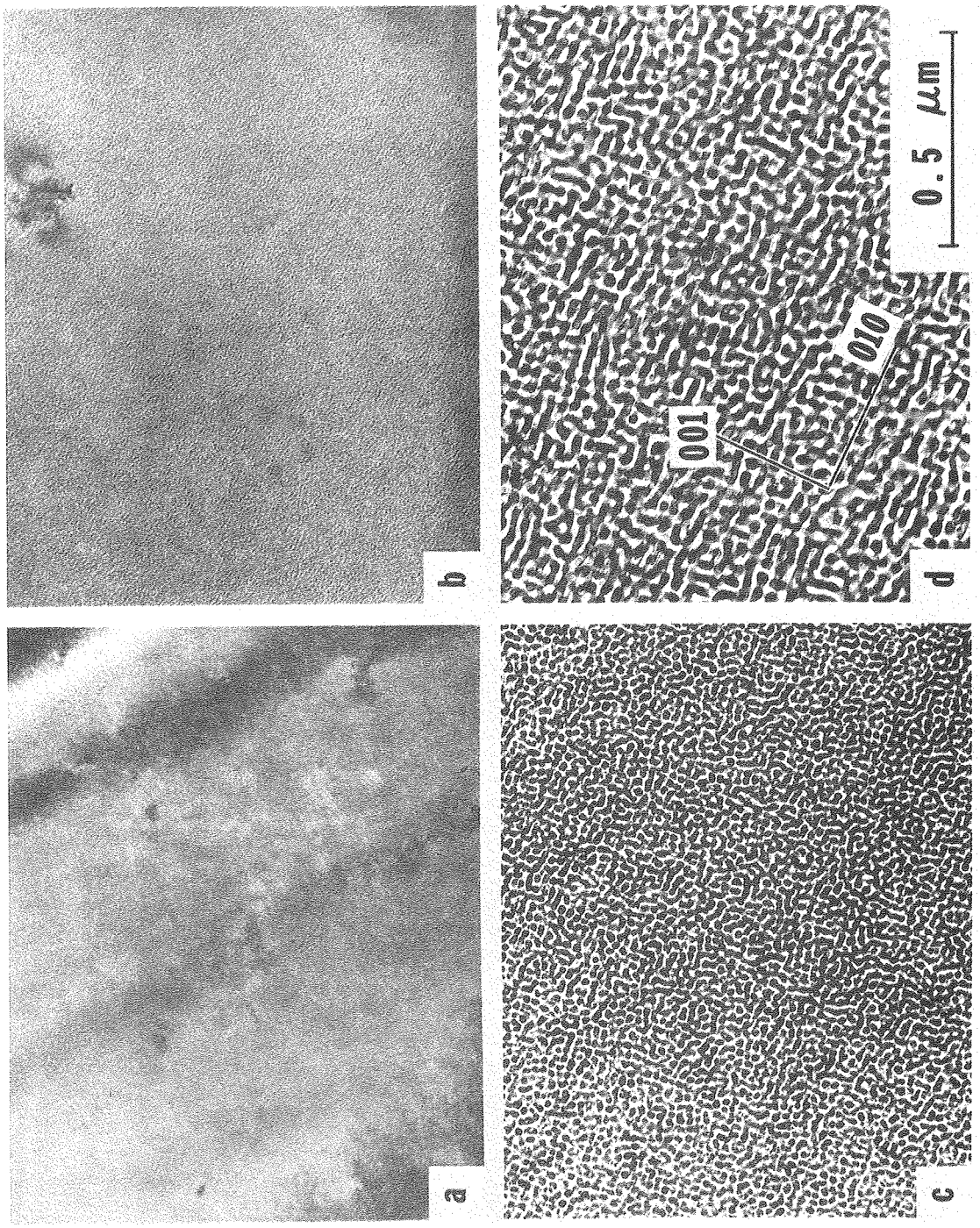

Fig. 11

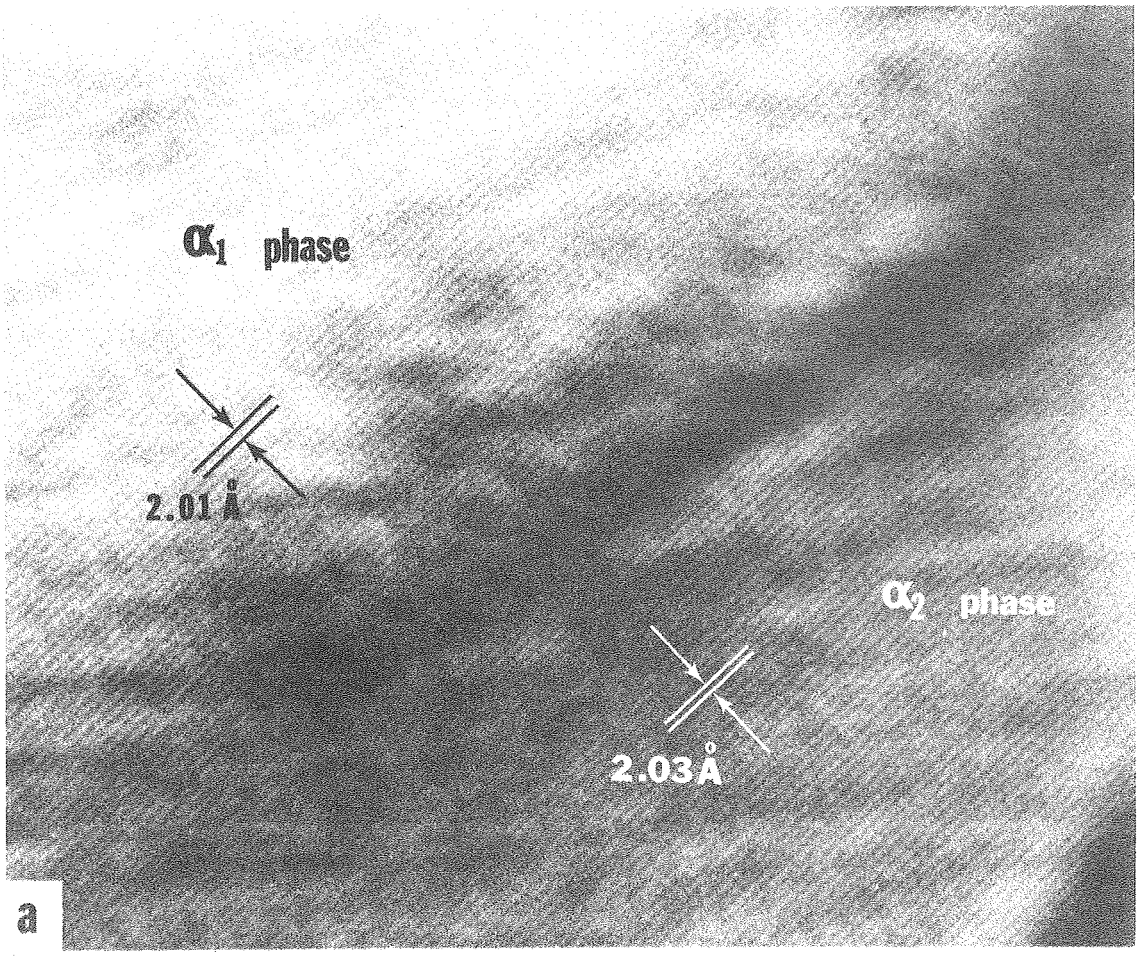

XBB 773-1892

Fig. 12

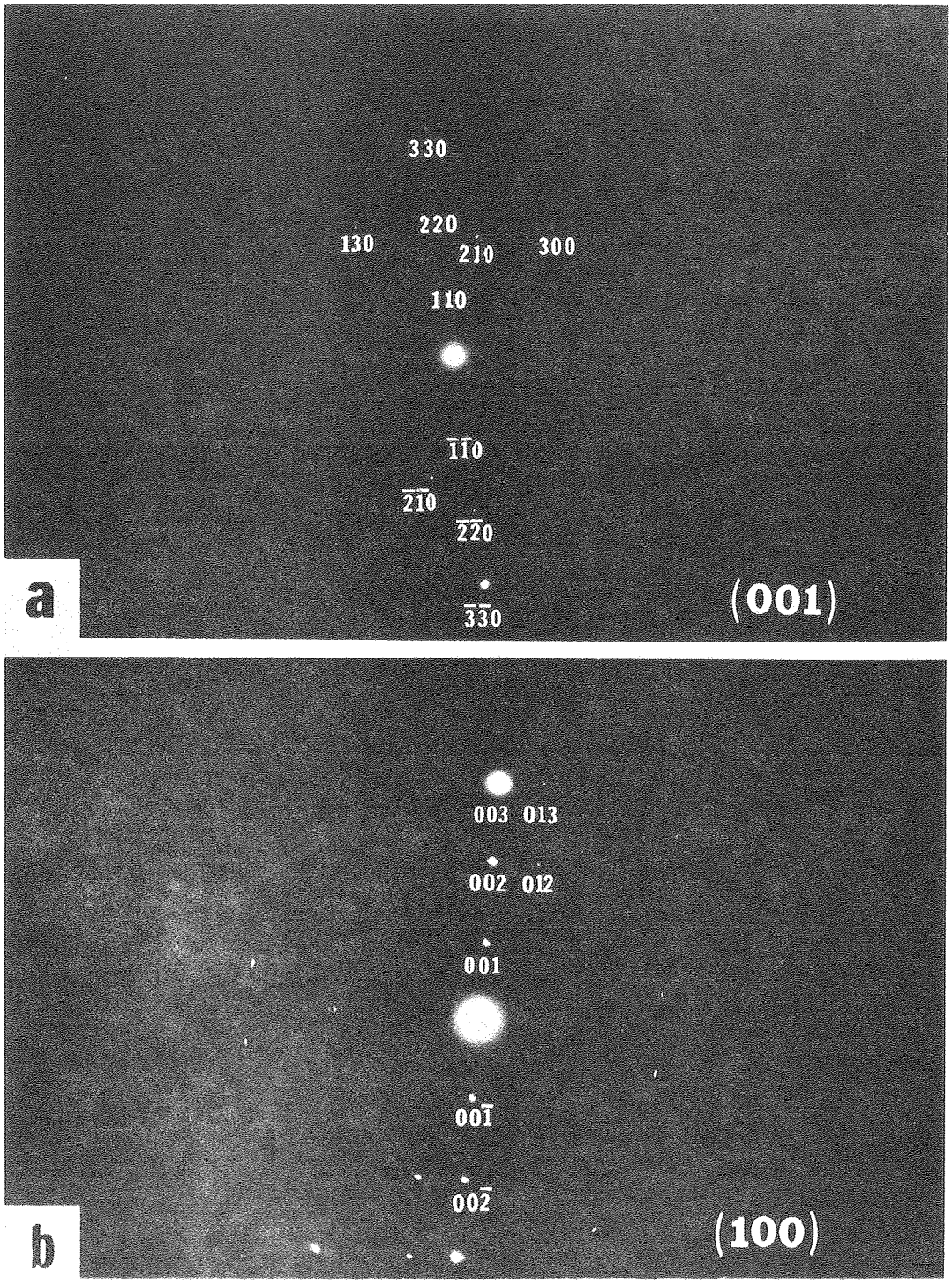

XBB 783-3254

Fig. 13

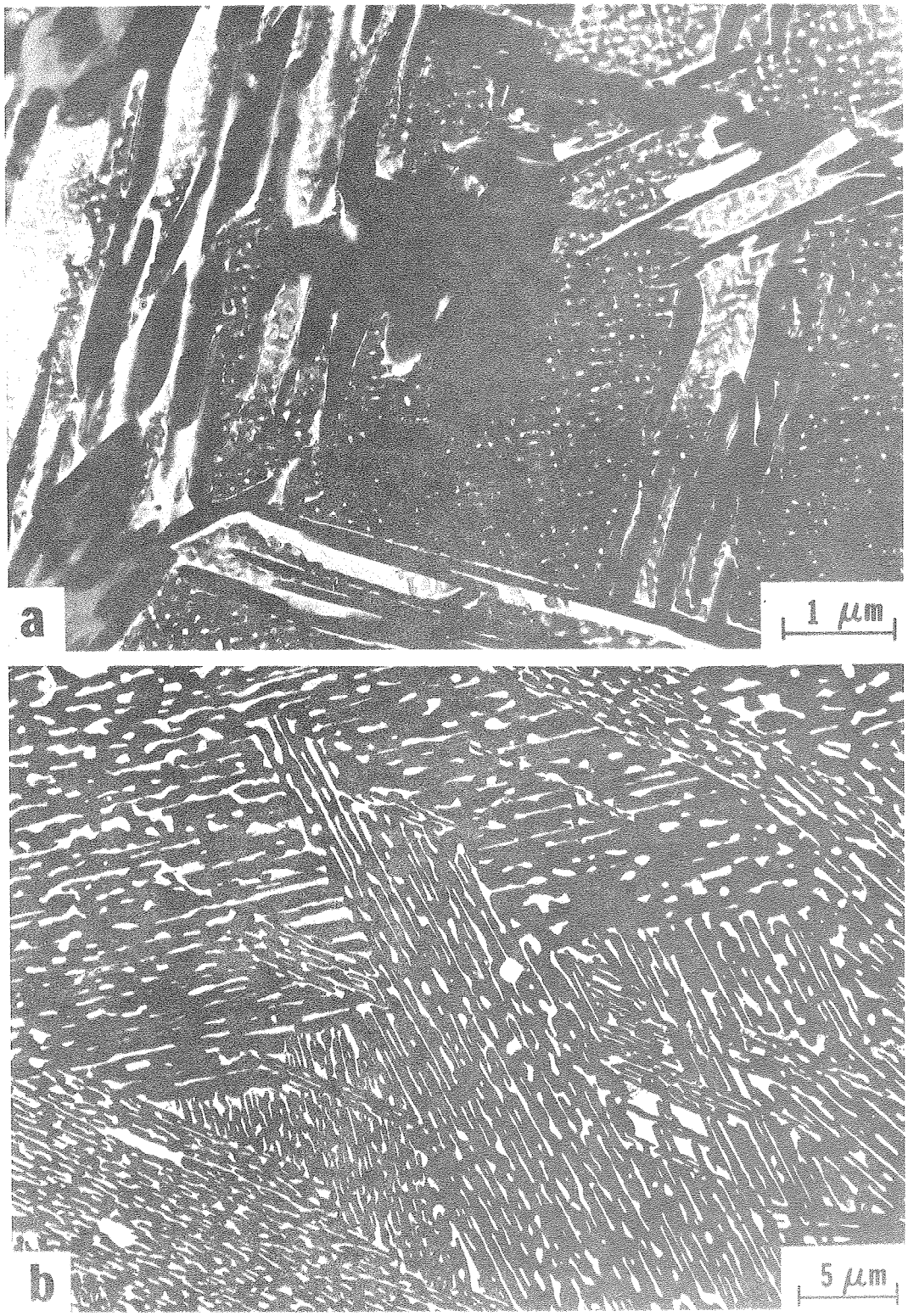

XBB 781-994

Fig. 14

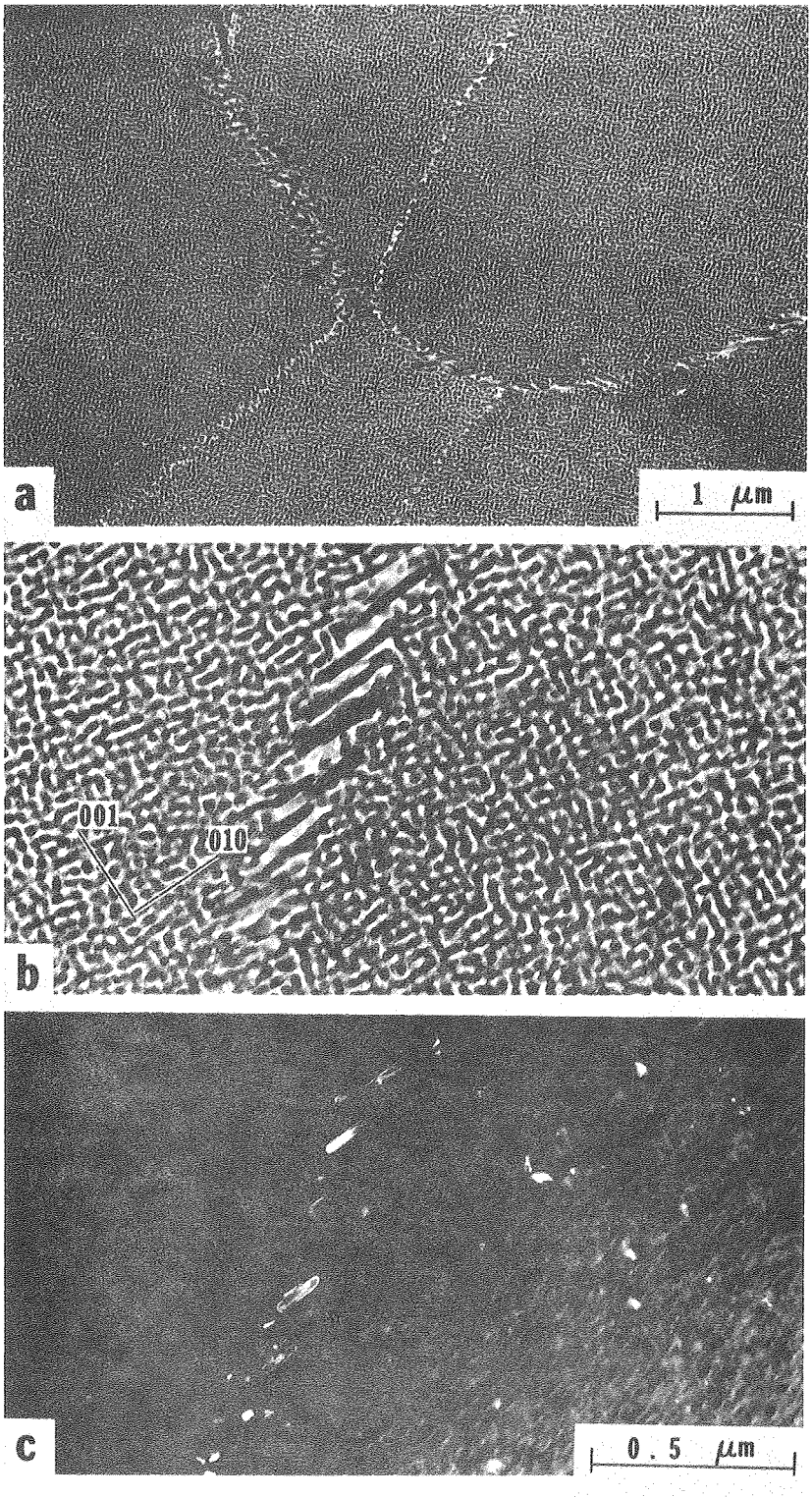

XBB 781-991

Fig. 15

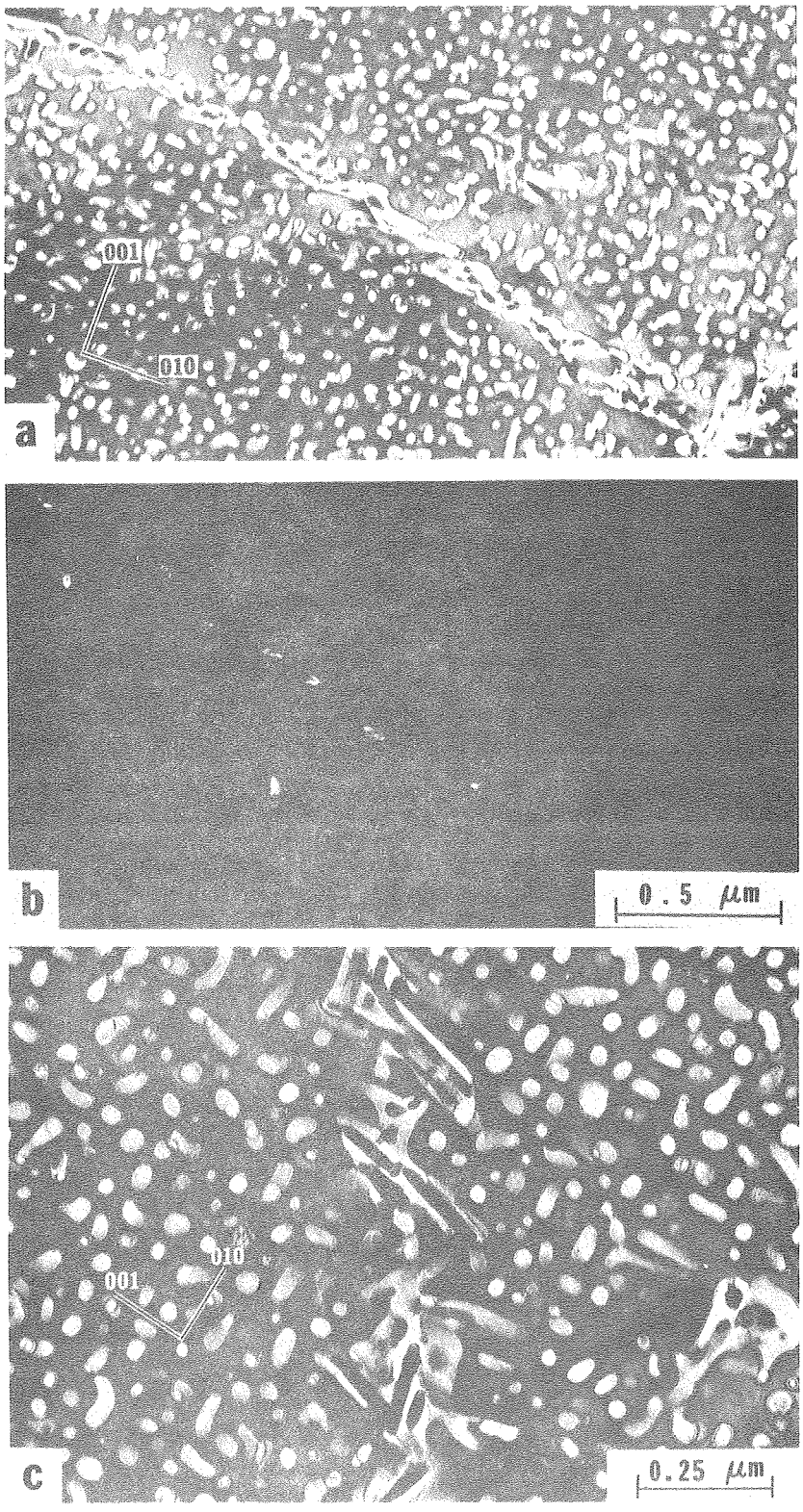

XBB 781-992

Fig. 16

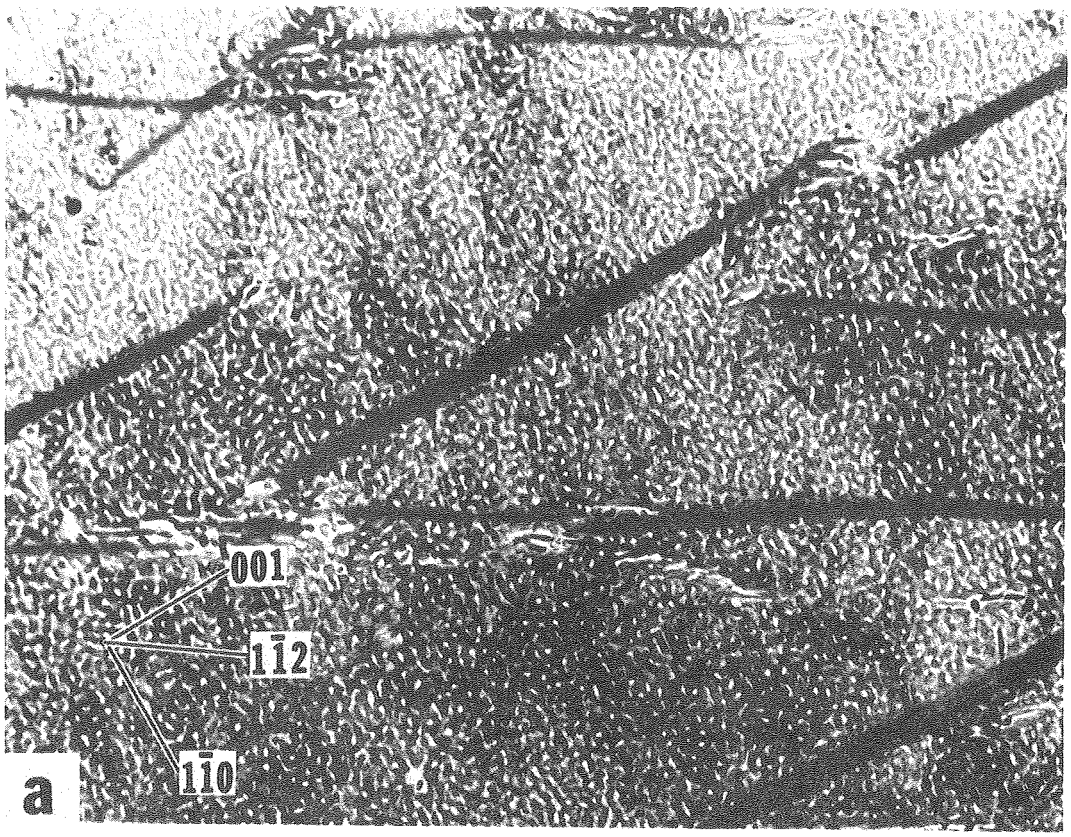

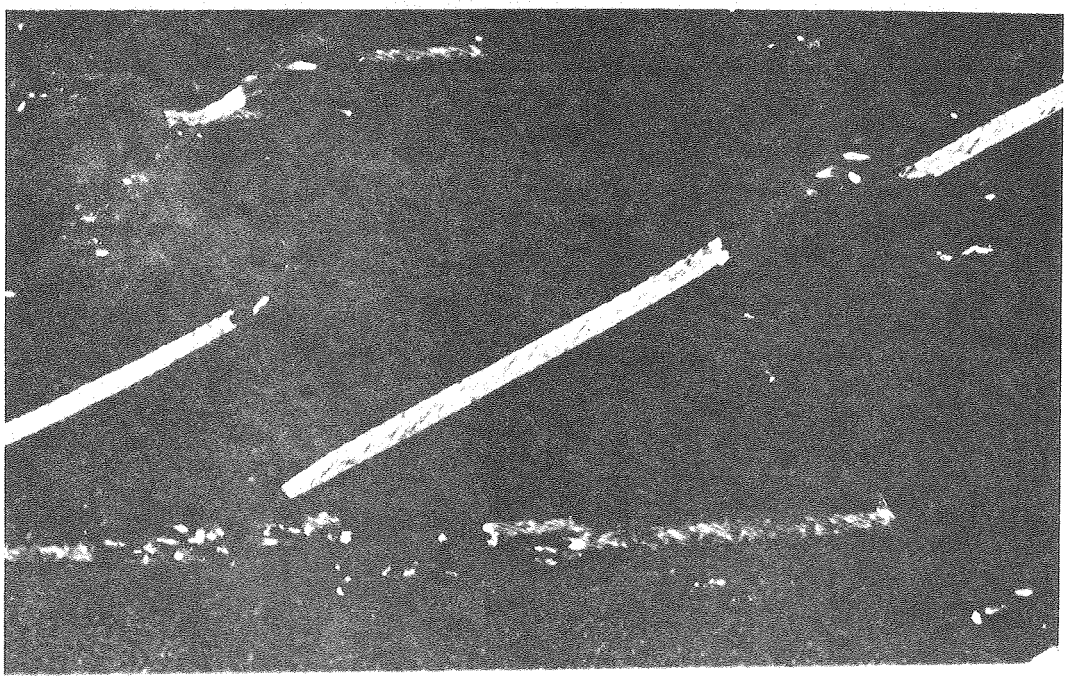

XBB 781-993

Fig. 17

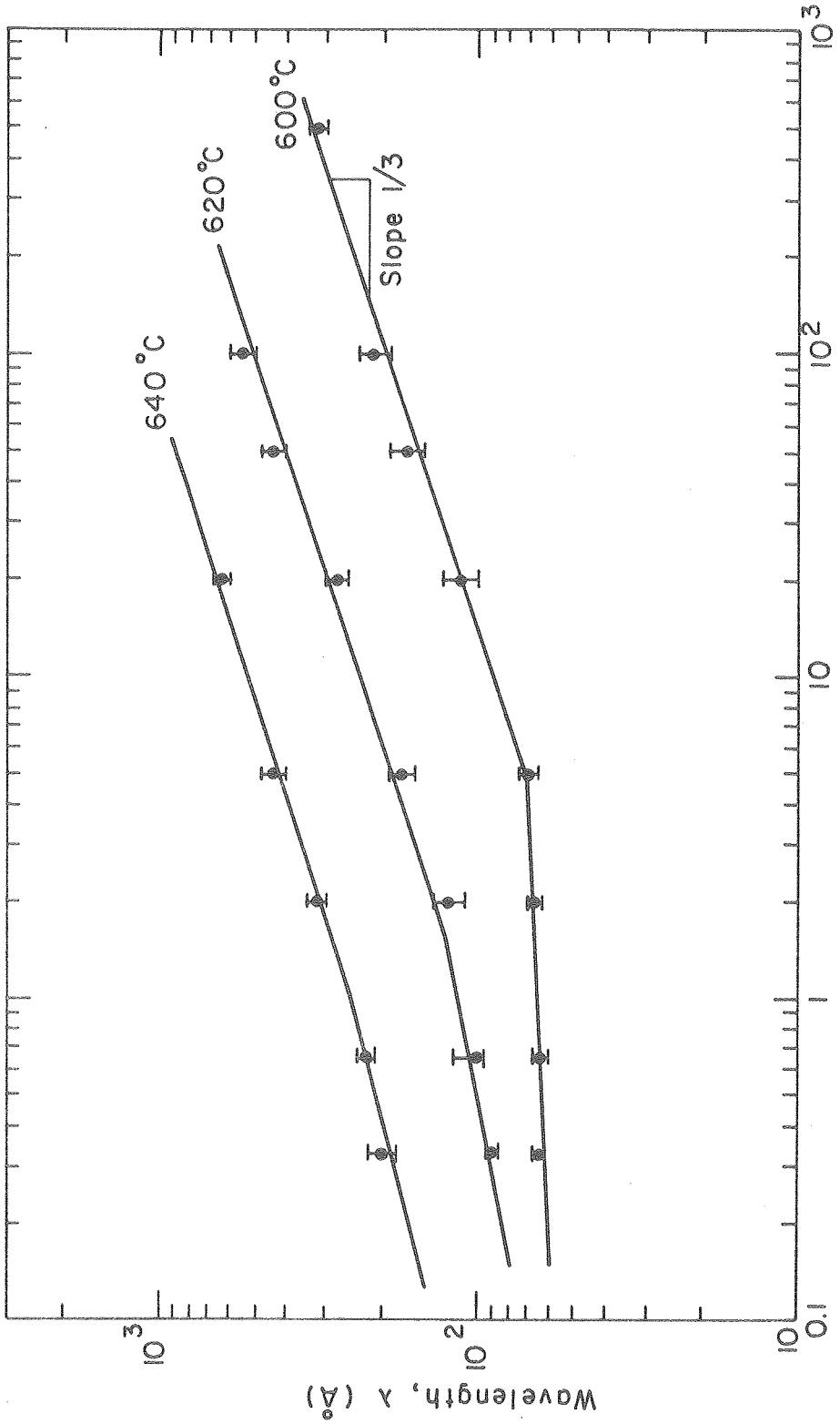

XBL 782-4568

Fig. 18

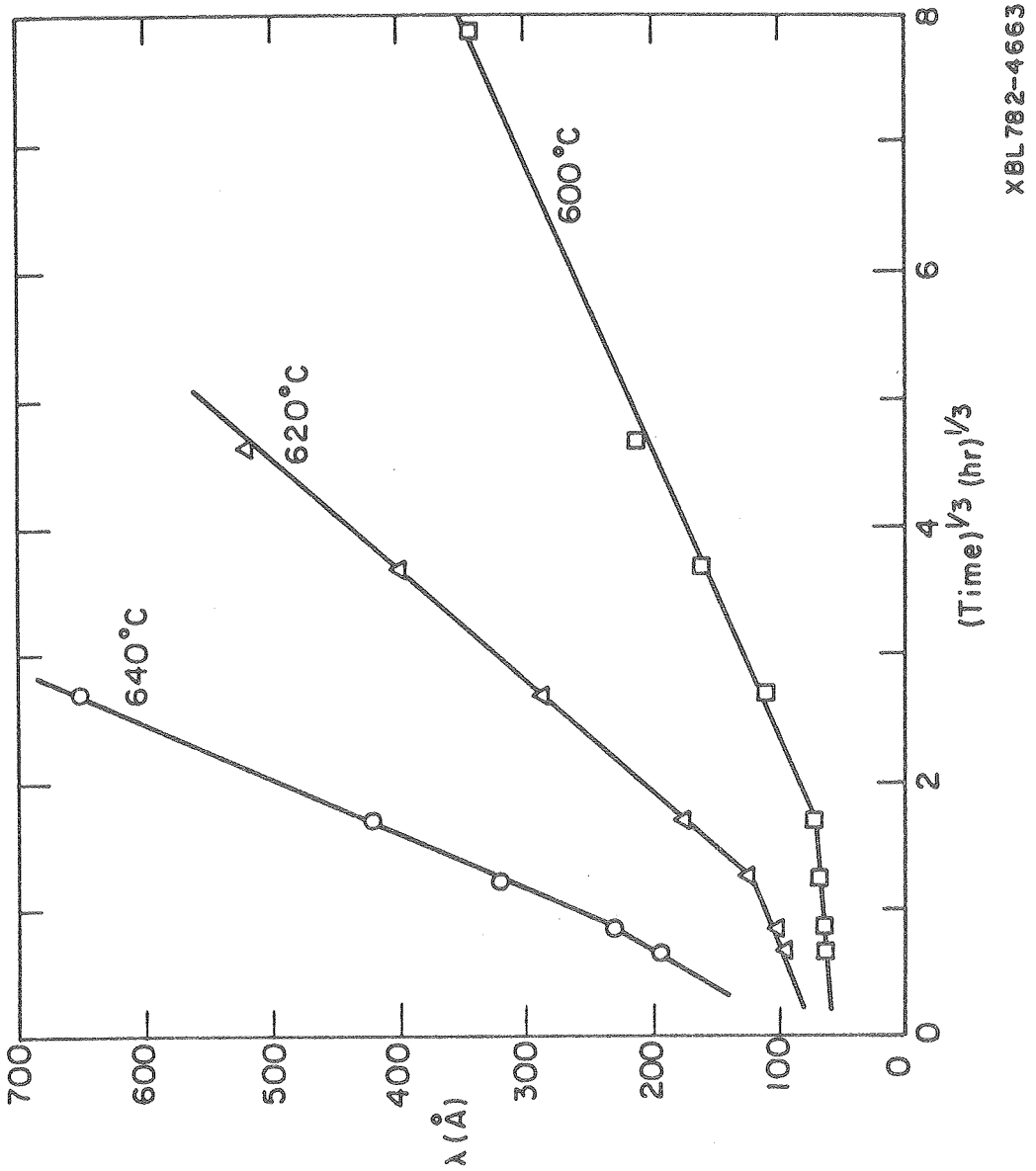
700
600
500
400
300
200
100
0
λ (Å)
0
2
4
6
8
(Time)^1/3 (hr)^1/3
640°C
620°C
600°C
XBL782-4663

Fig. 19

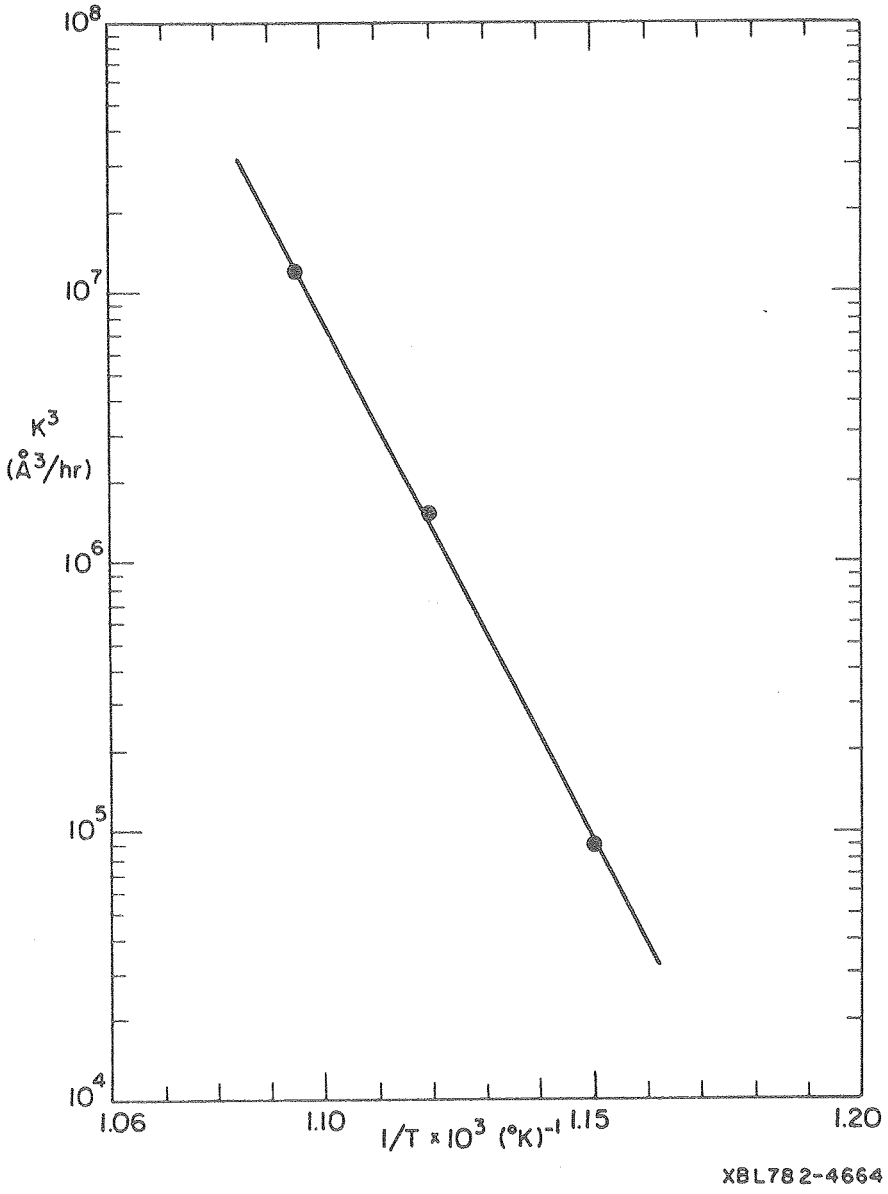
10^8
10^7
10^6
10^5
10^4
K^3
$(Å^3/hr)$
1.06
1.10
1.15
1.20
$1/T \times 10^3$ (°K)$^{-1}$
XBL782-4664

Fig. 20

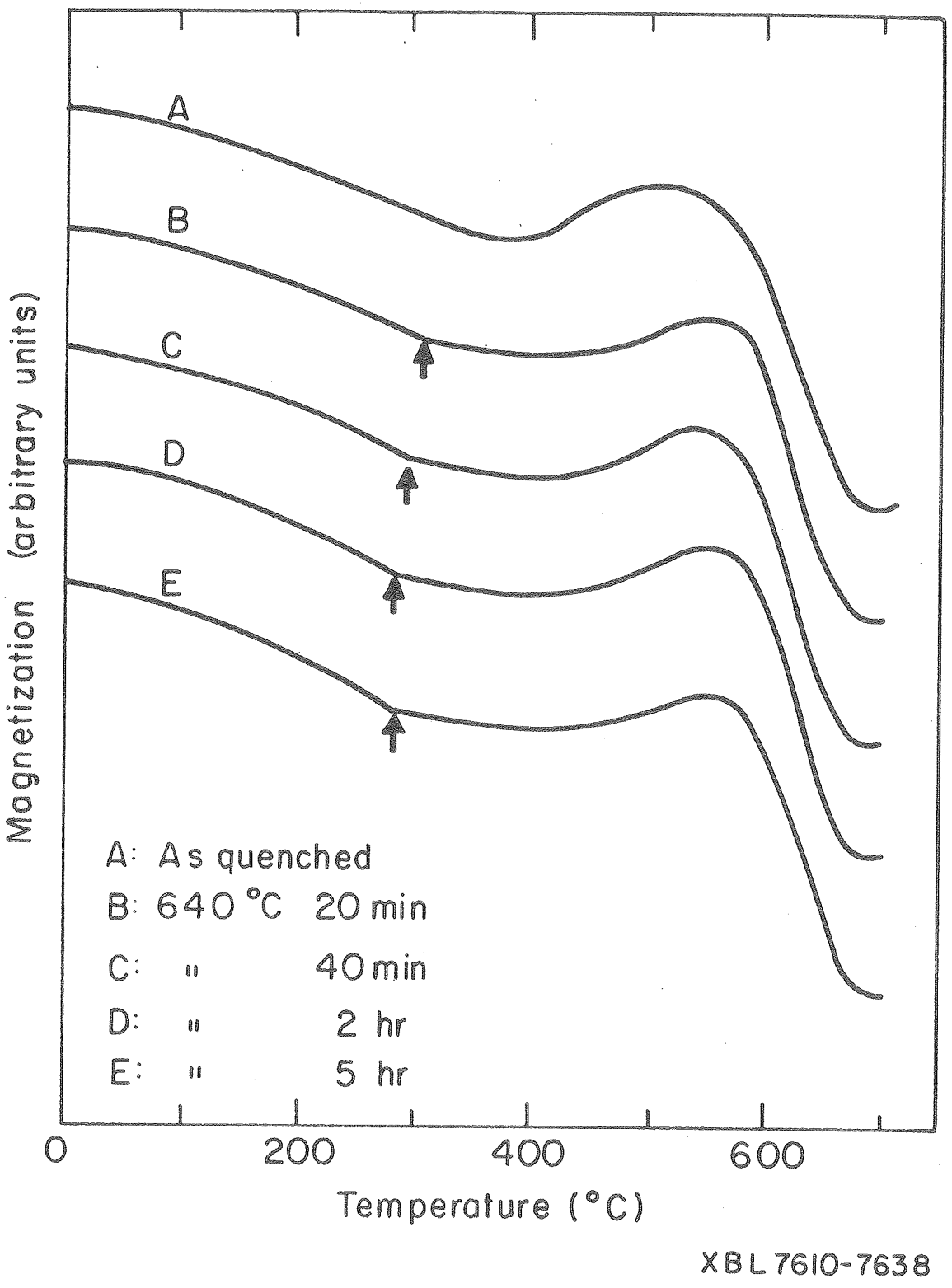
A
B
C
D
E
Magnetization (arbitrary units)
A: As quenched
B: 640 °C 20 min
C: " 40 min
D: " 2 hr
E: " 5 hr
0
200
400
600
Temperature (°C)
XBL 7610-7638

Fig. 21

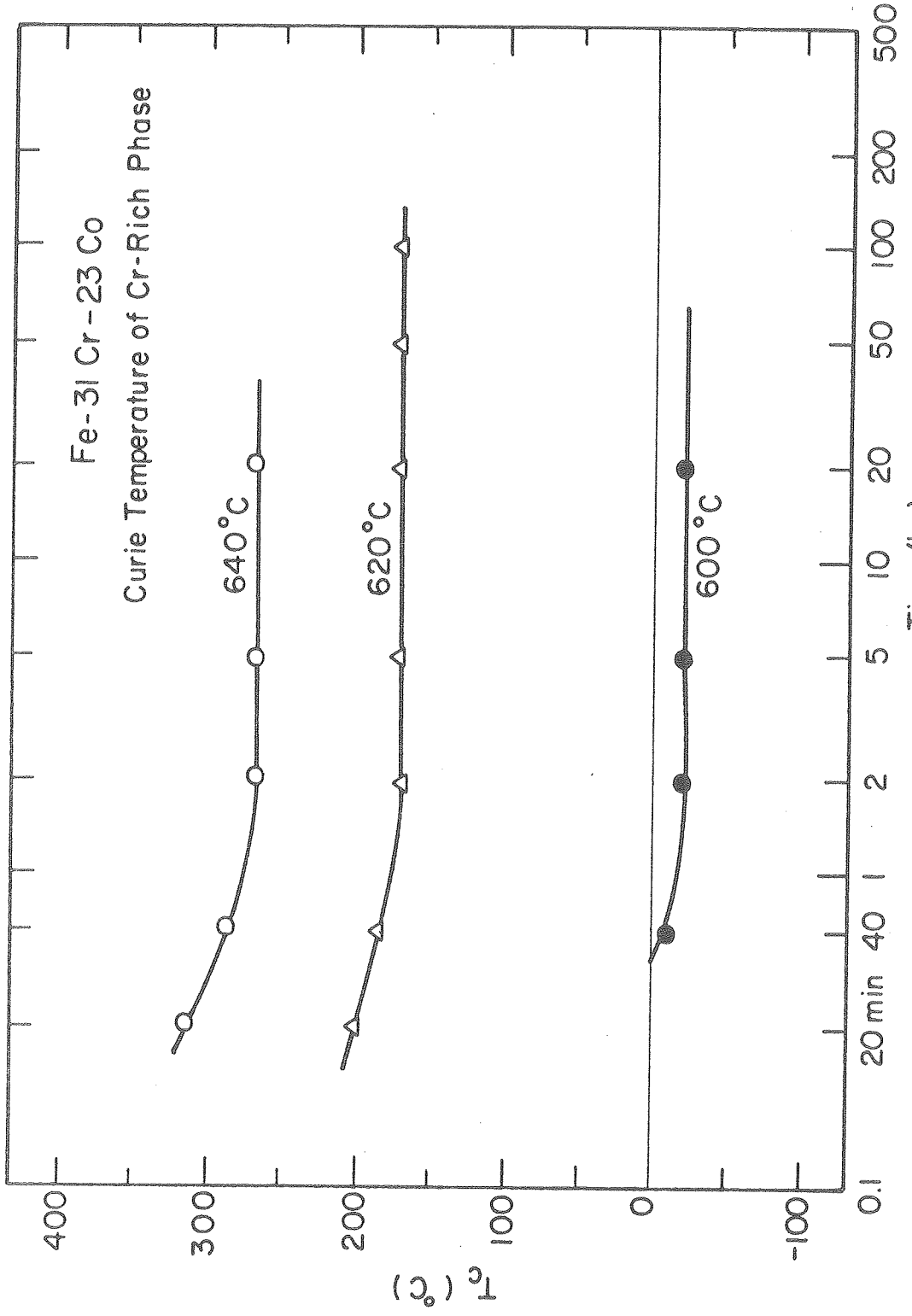

XBL 7610-7640

Fig. 22

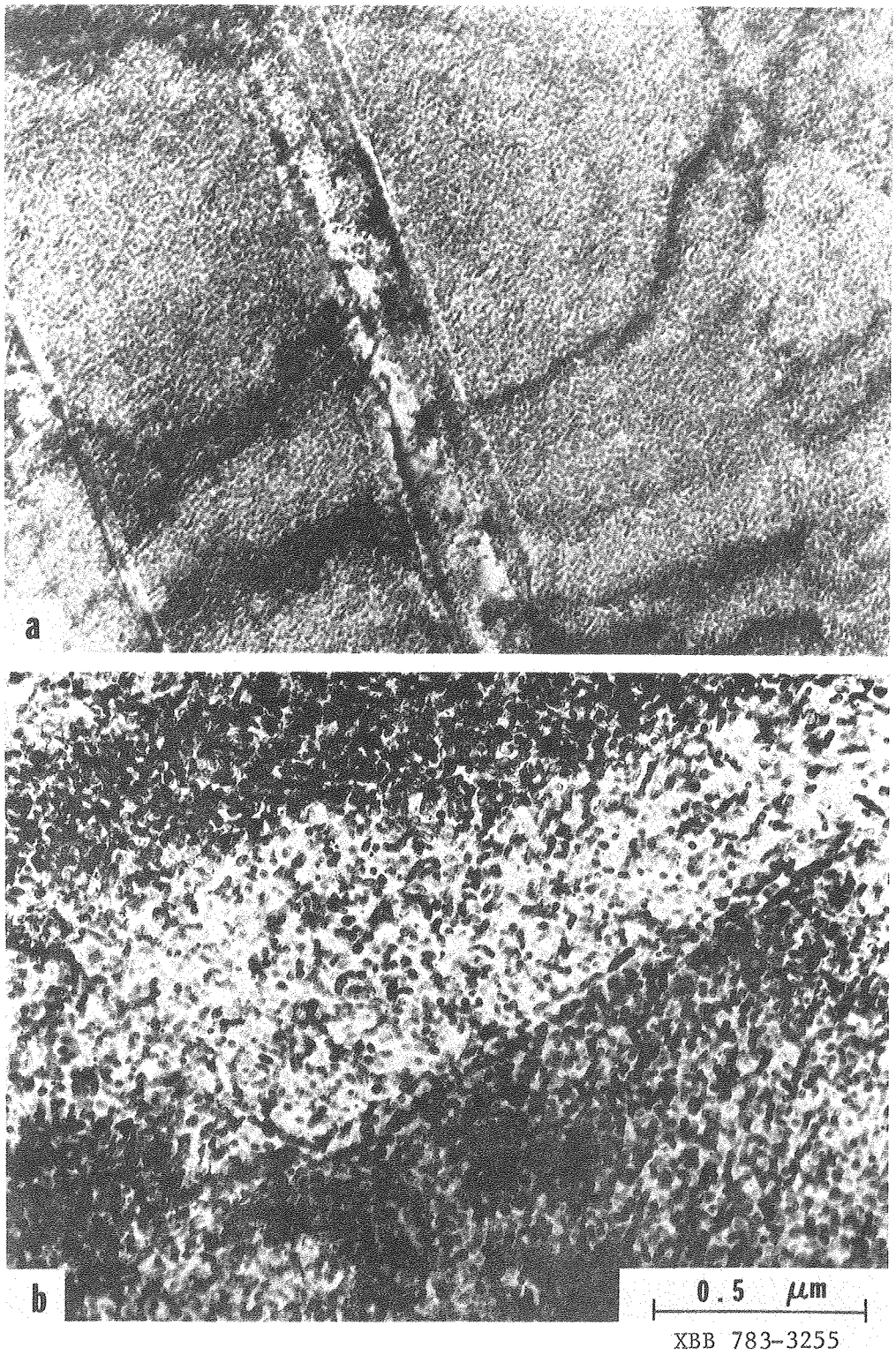

Fig. 23

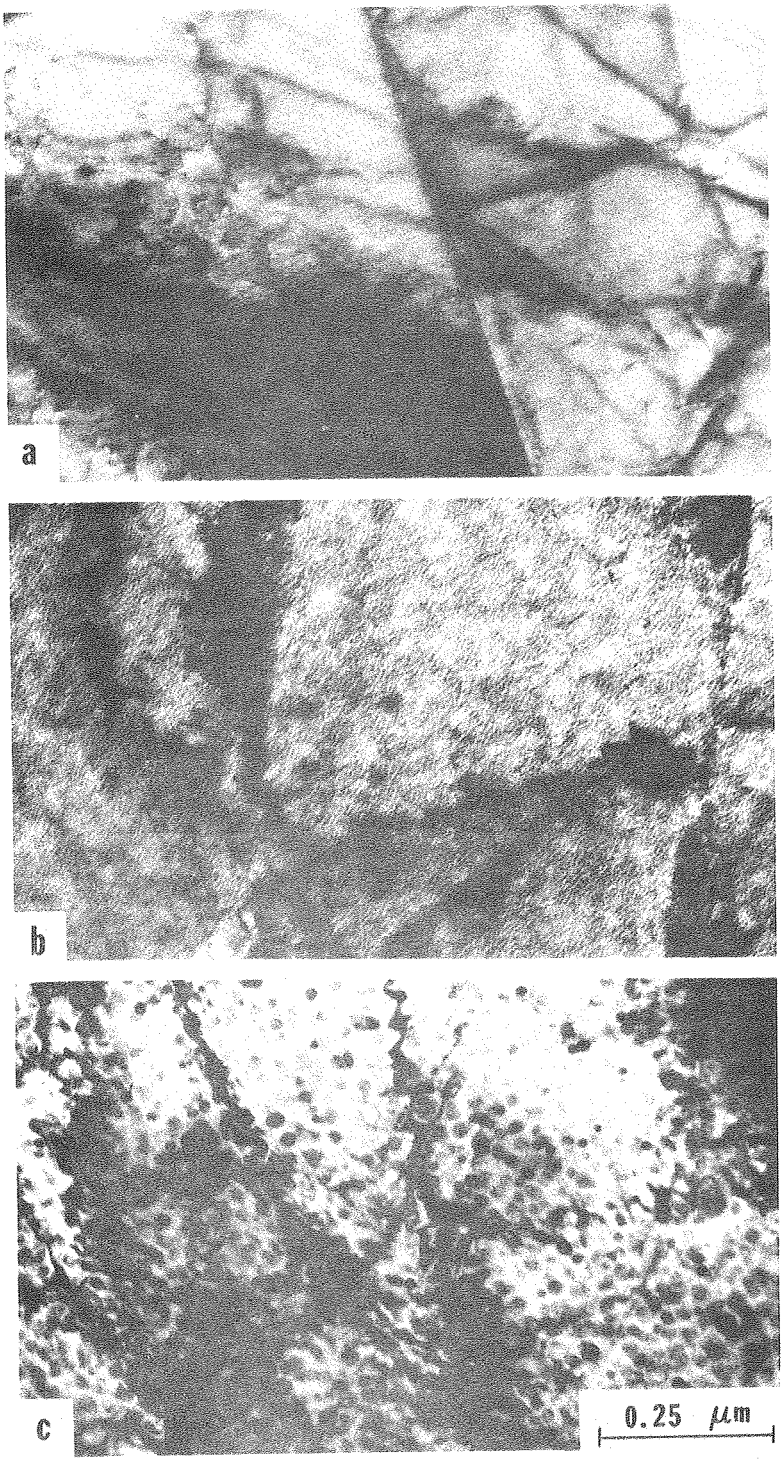

XBB 783-3257

Fig. 24

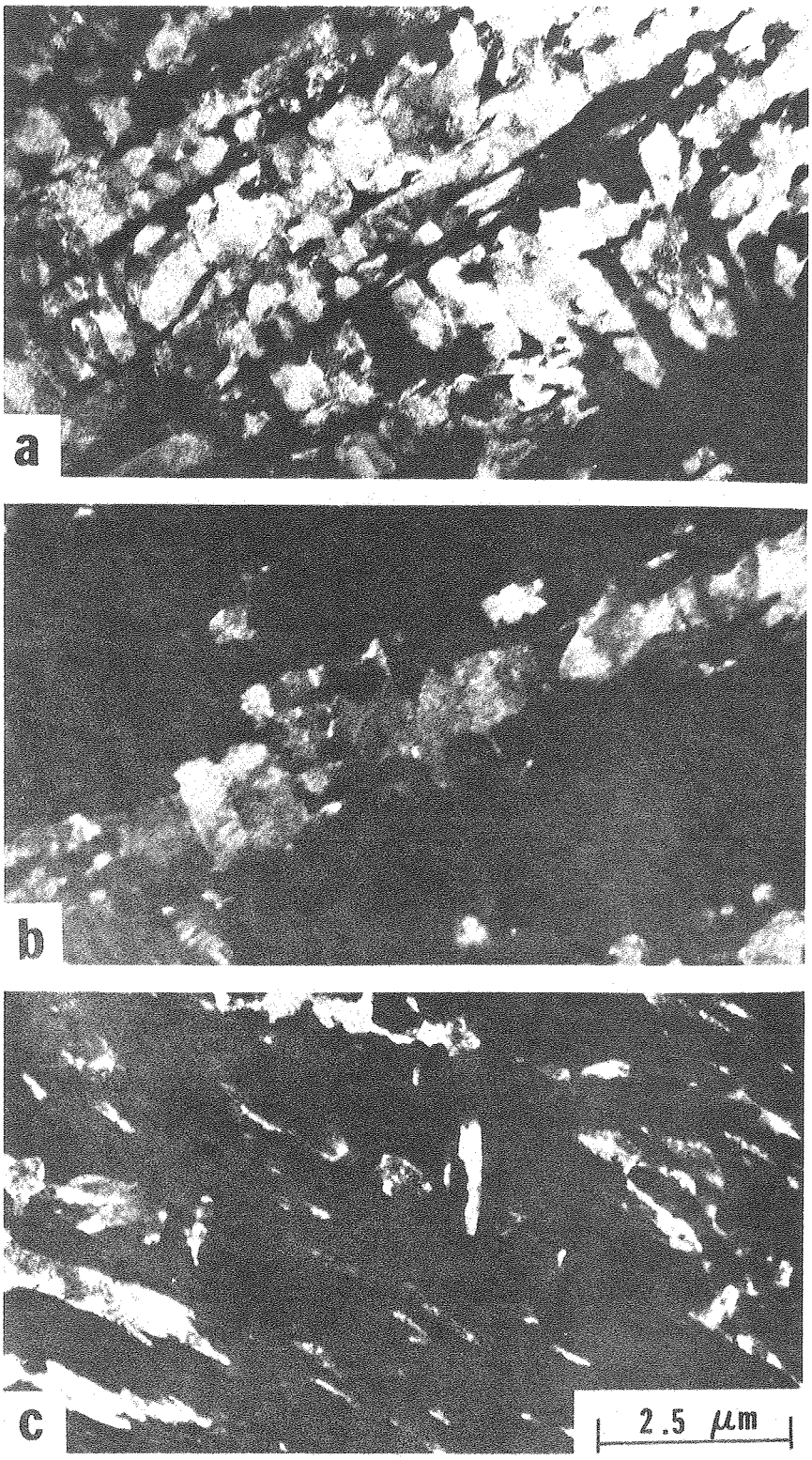

XBB 781-651

Fig. 25

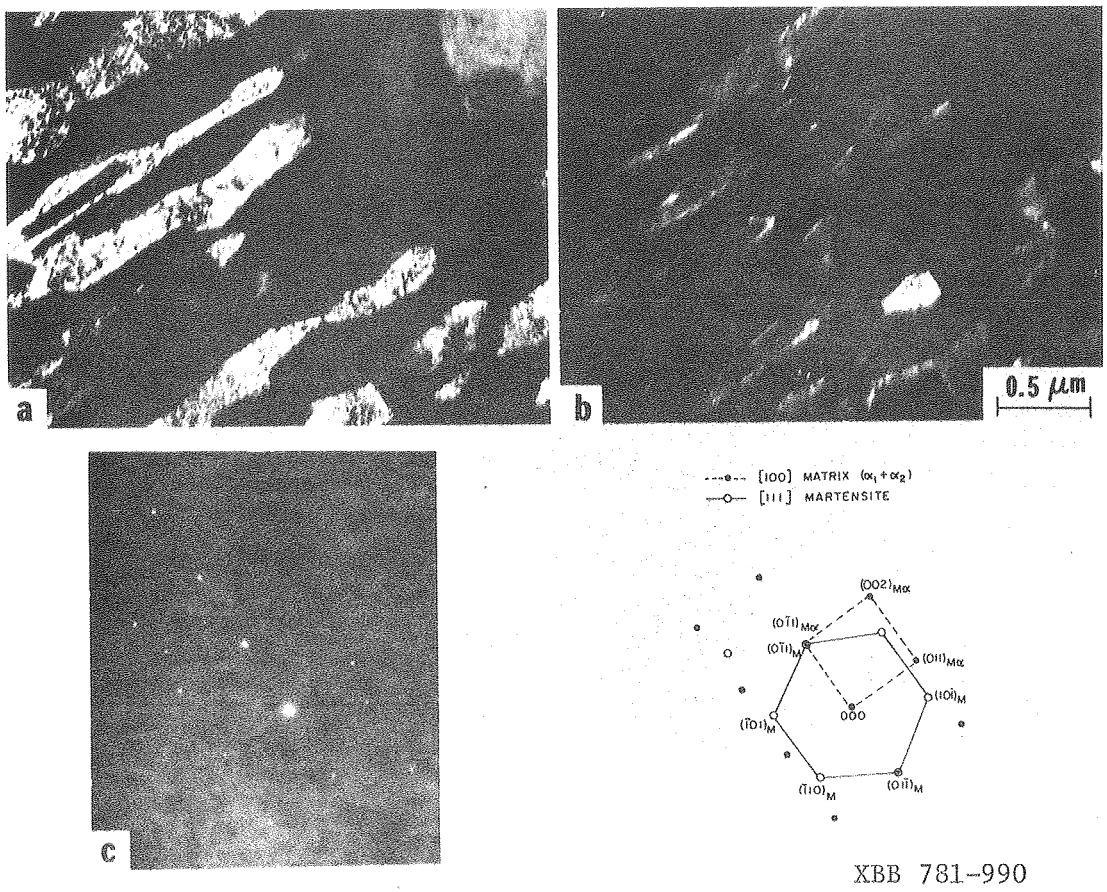
a
b
0.5 μm
c
[100] MATRIX ($\alpha_1+\alpha_2$)
[111] MARTENSITE
$(002)_{M\alpha}$
$(0\bar{1}1)_{M\alpha}$
$(0\bar{1}\bar{1})_M$
$(011)_{M\alpha}$
$(10\bar{1})_M$
000
$(\bar{1}01)_M$
$(\bar{1}10)_M$
$(01\bar{1})_M$
XBB 781-990

Fig. 26

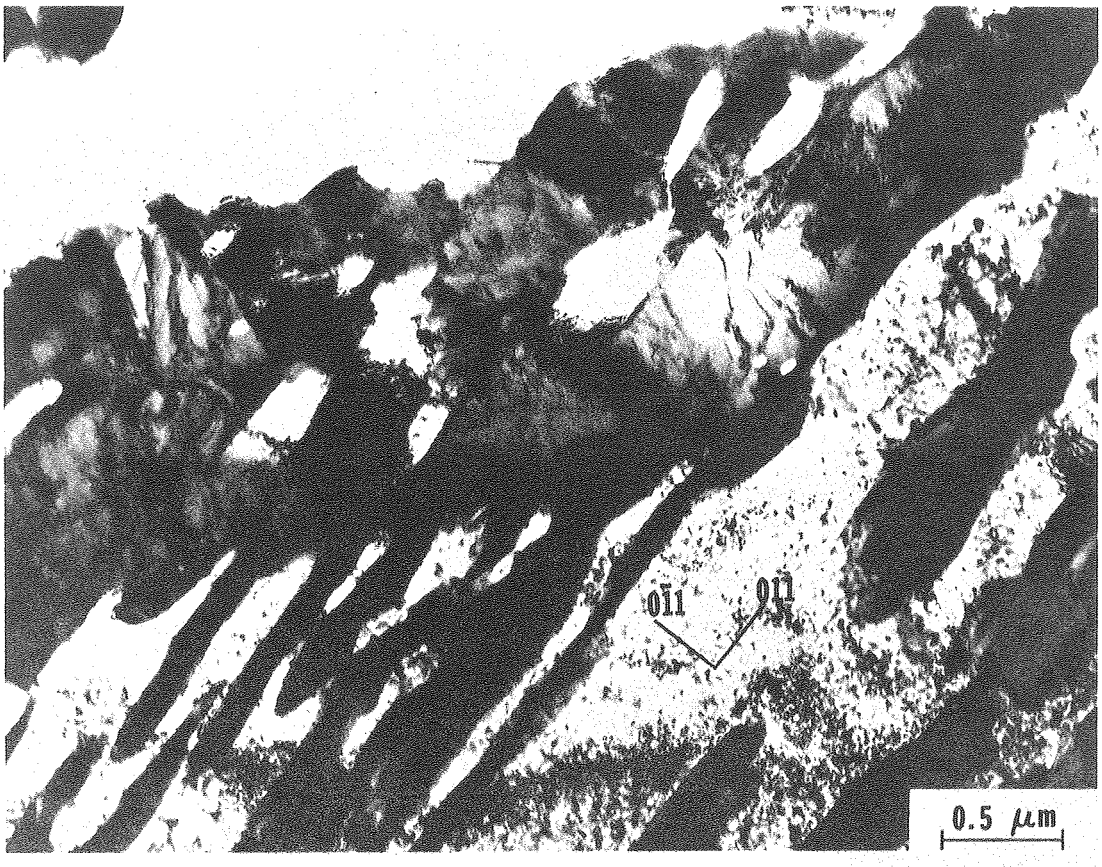

XBB 783-3260

Fig. 27

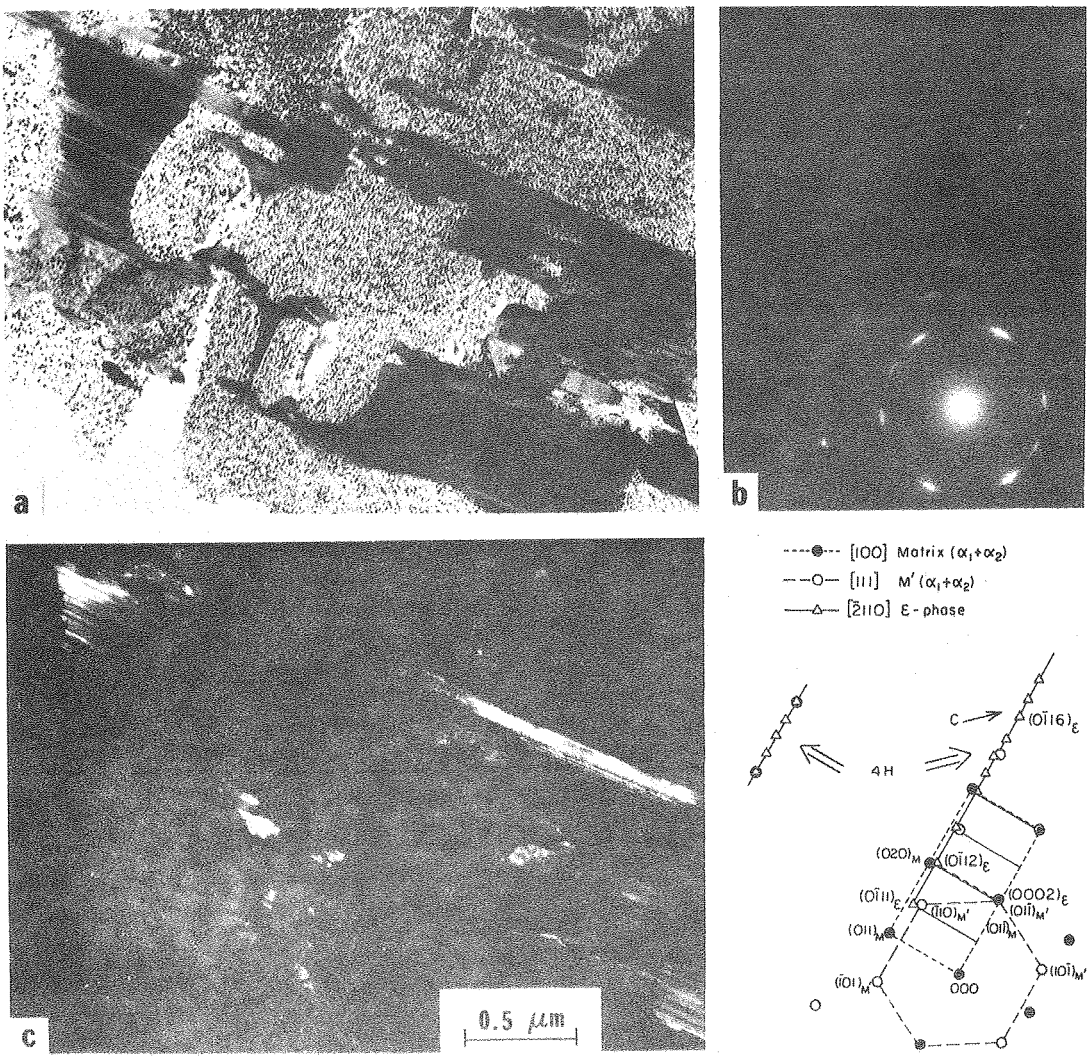
a
b
c
0.5 μm
[100] Matrix (α1+α2)
[111] M' (α1+α2)
[2̄110] ε-phase
C
4H
(0001)ε
(020)M
(0002)ε
(000)
XBB 782-1924

Fig. 28

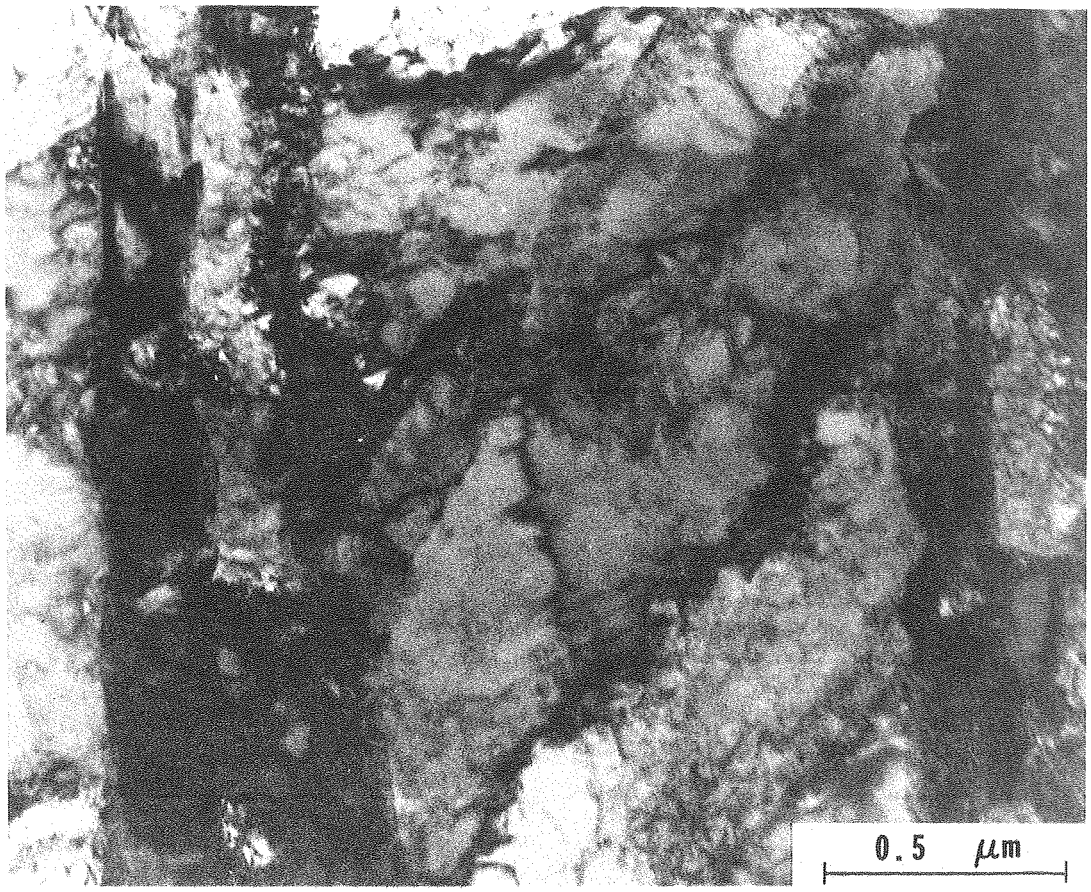

XBB 783-3259

Fig. 29

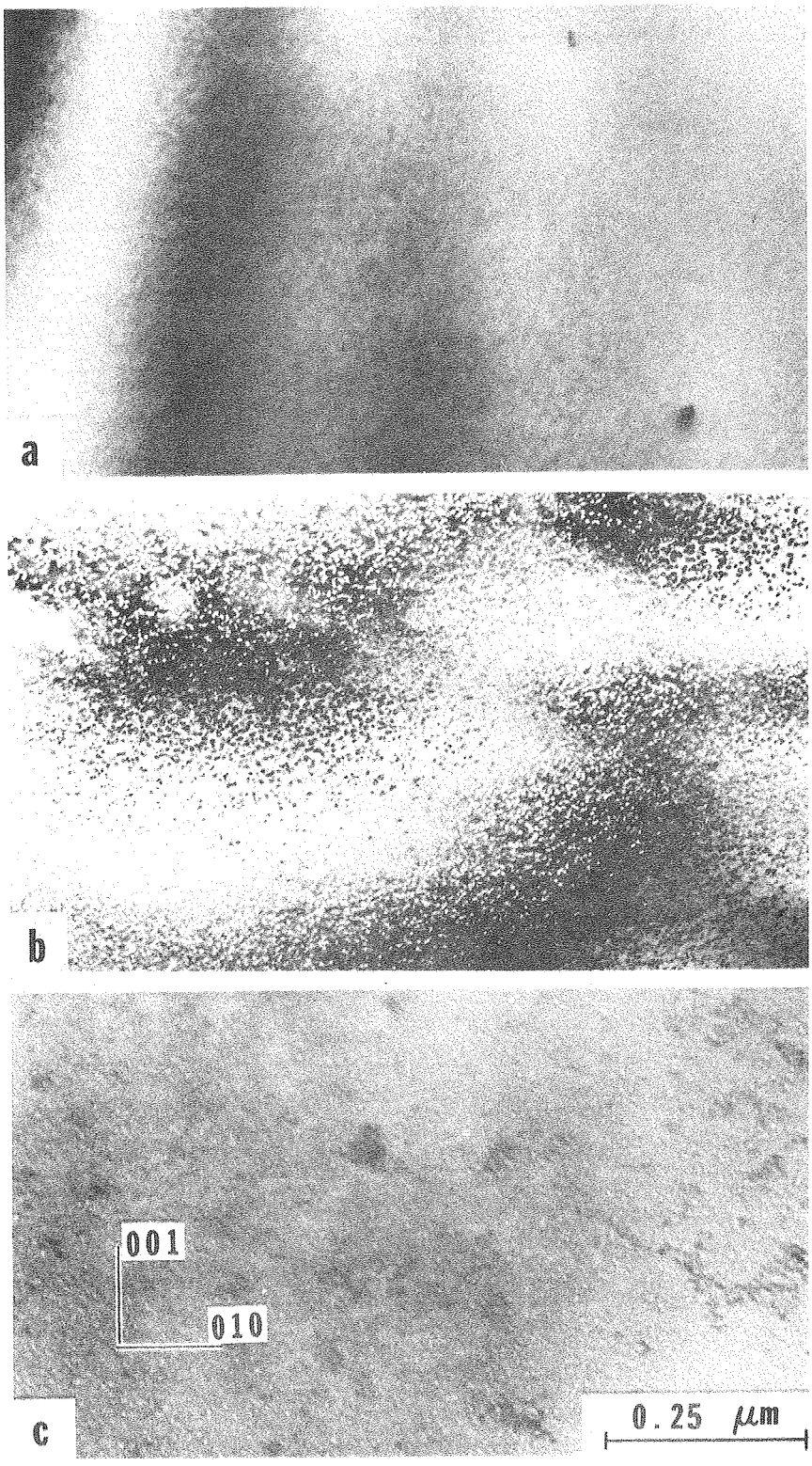

XBB 781-652

Fig. 30

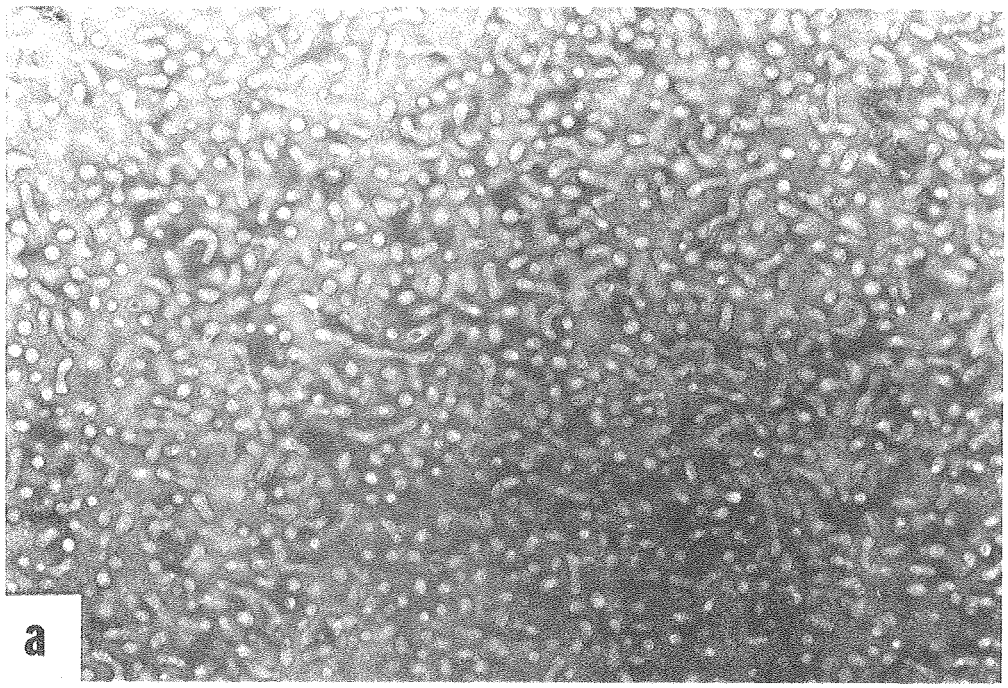

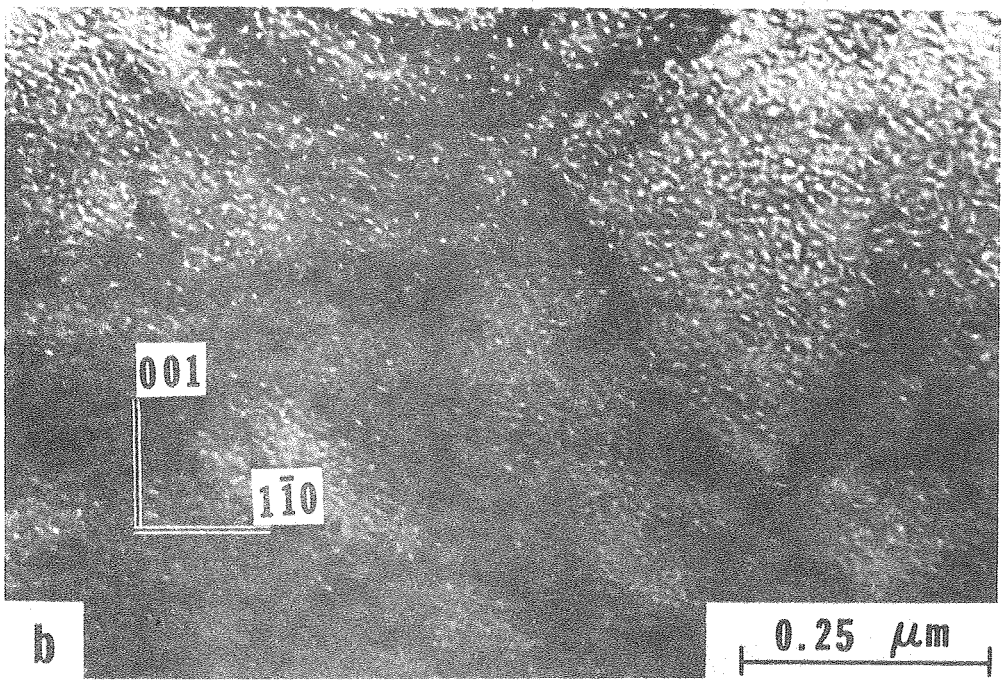

XBB 781-652

Fig. 31

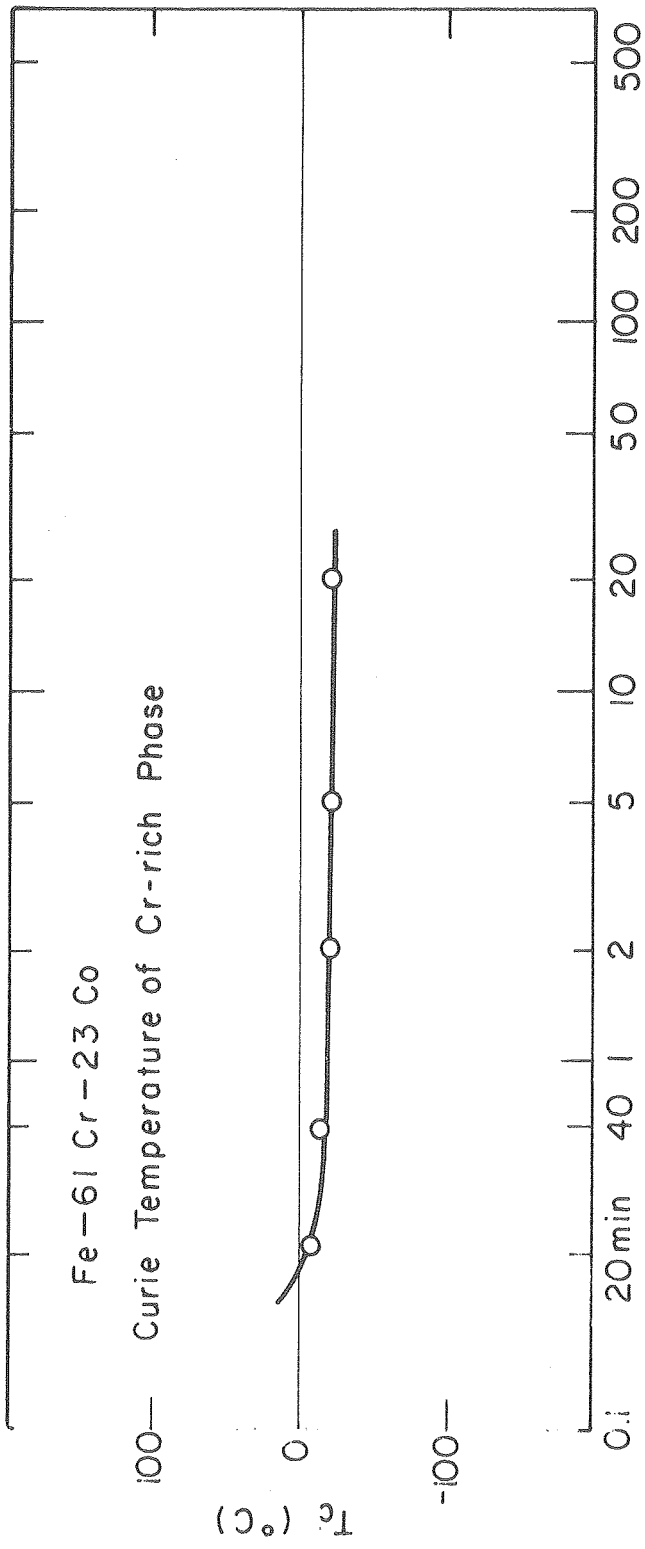
Fe-61 Cr-23 Co
Curie Temperature of Cr-rich Phase
T_c (°C)
100
0
-100
0.1
20 min
40
1
2
5
10
20
50
100
200
500
Time (hr)
XBL 773-5171

Fig. 32

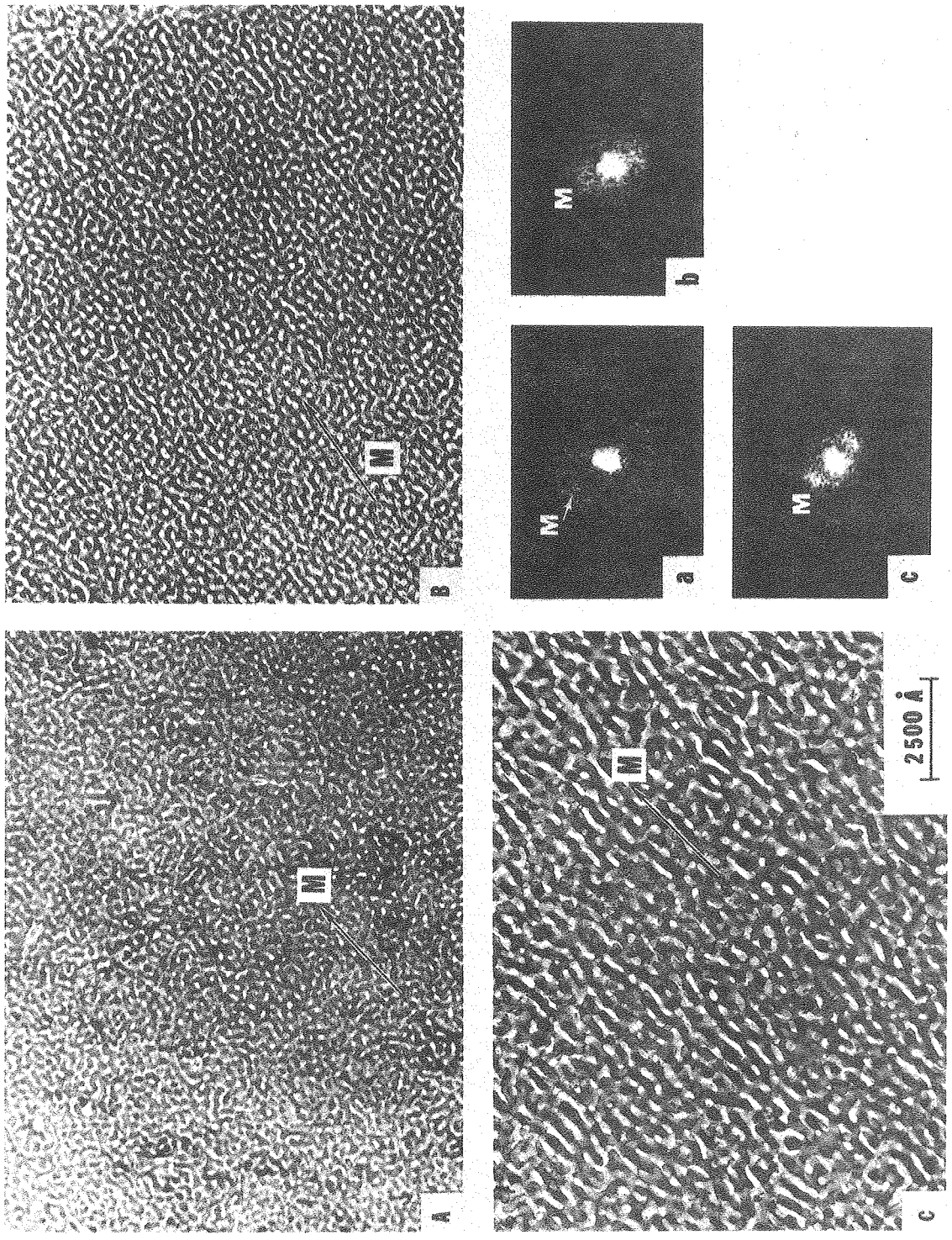

XBB 7612-11047

Fig. 33

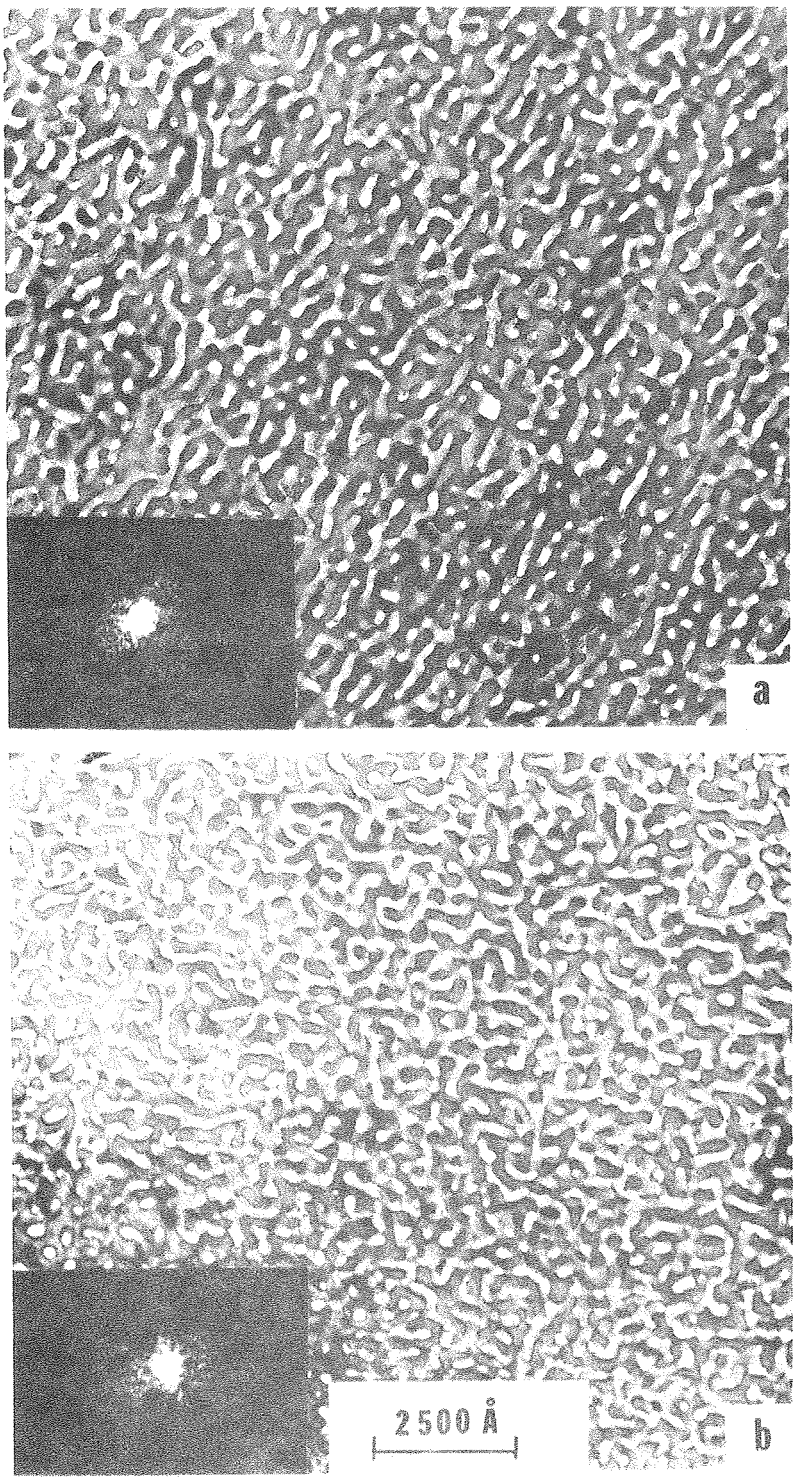

XBB 7612-11039

Fig. 34

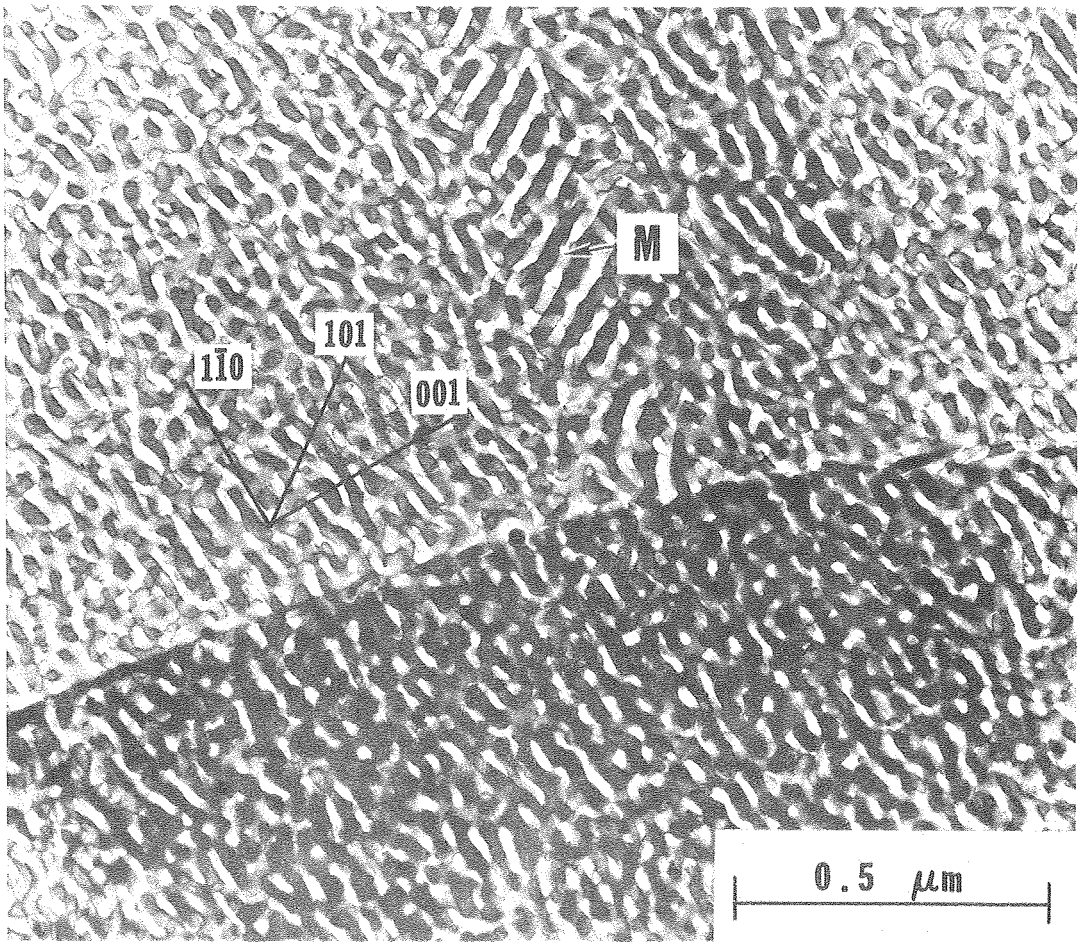

XBB 7612-11044

Fig. 35

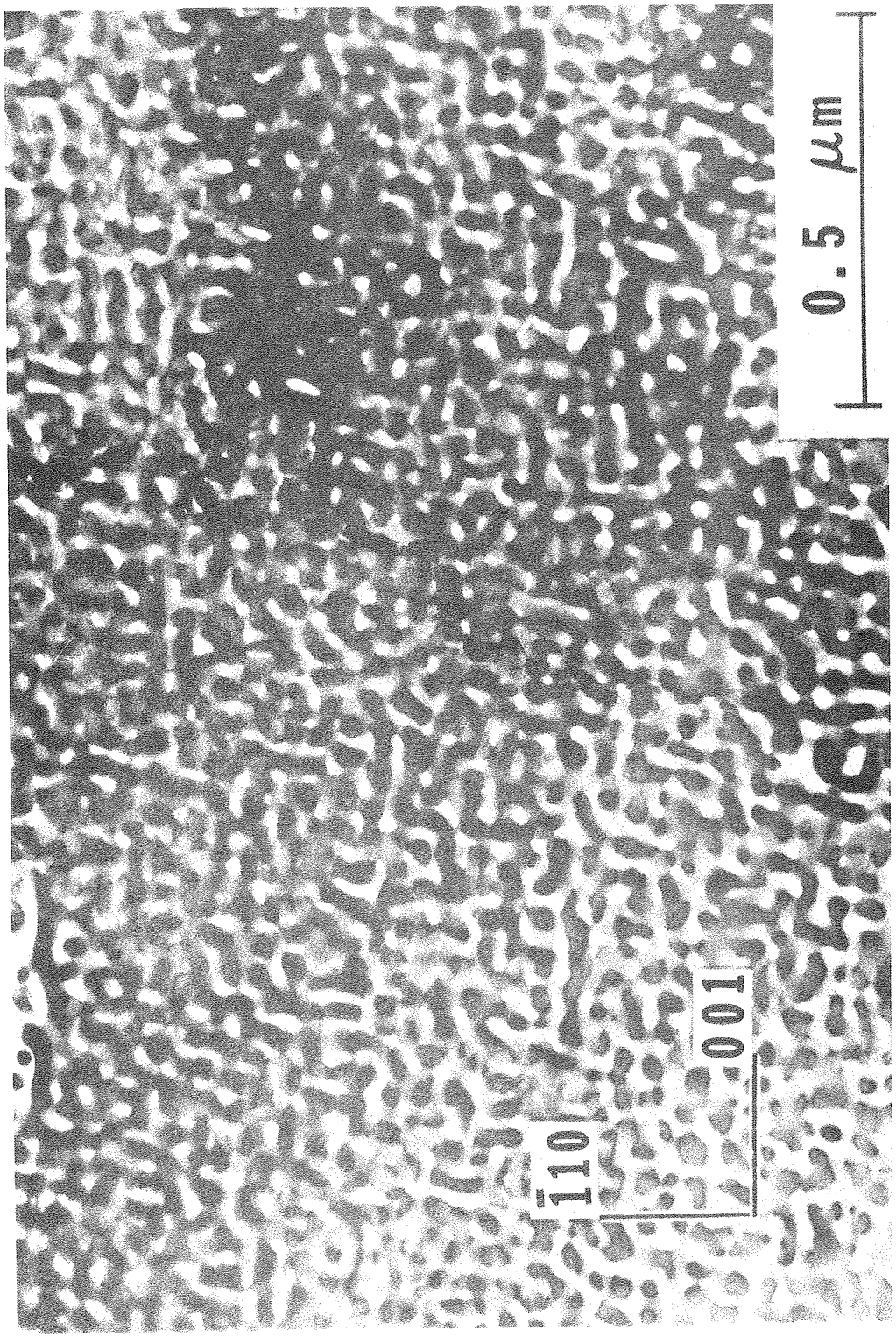

XBB 781-645

Fig. 36

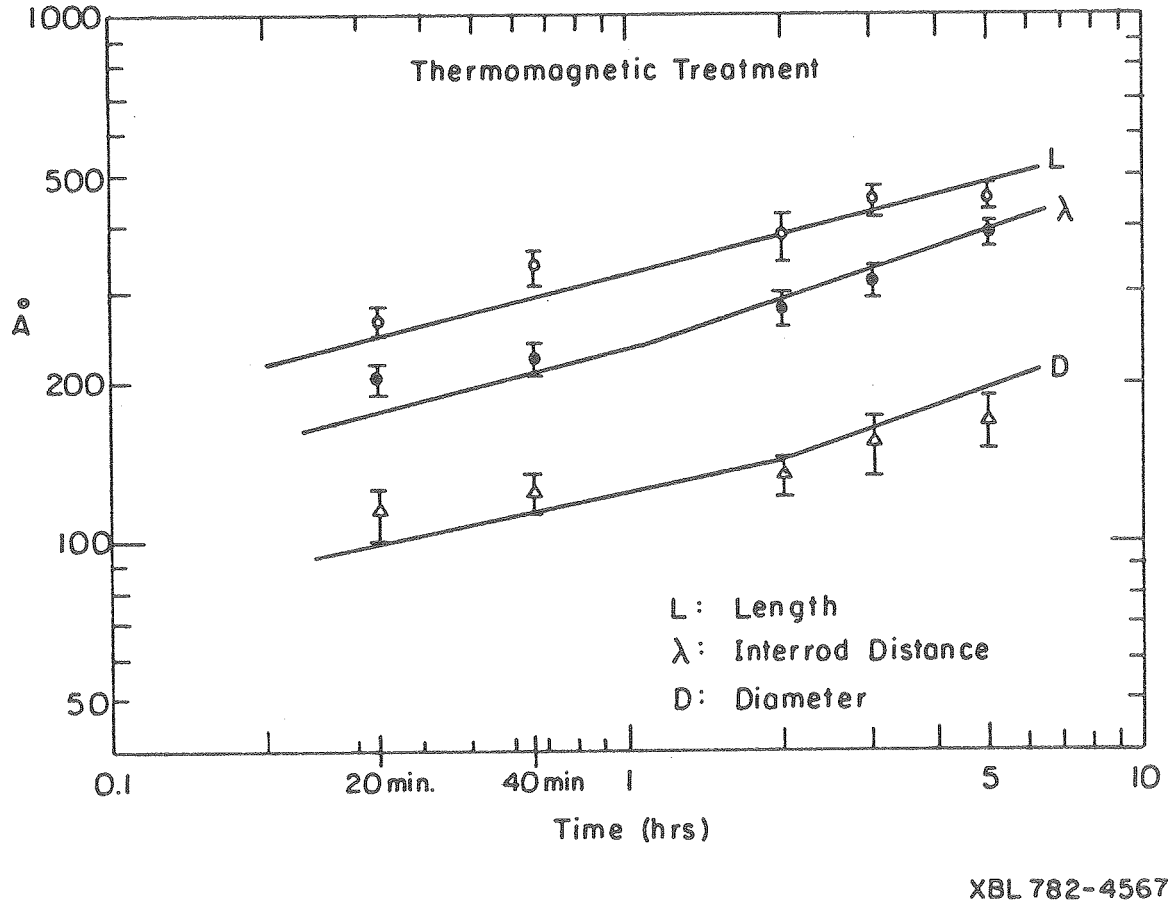
Thermomagnetic Treatment
1000
500
200
100
50
Å
L
λ
D
L: Length
λ: Interrod Distance
D: Diameter
0.1
20 min.
40 min
1
5
10
Time (hrs)
XBL 782-4567

Fig. 37

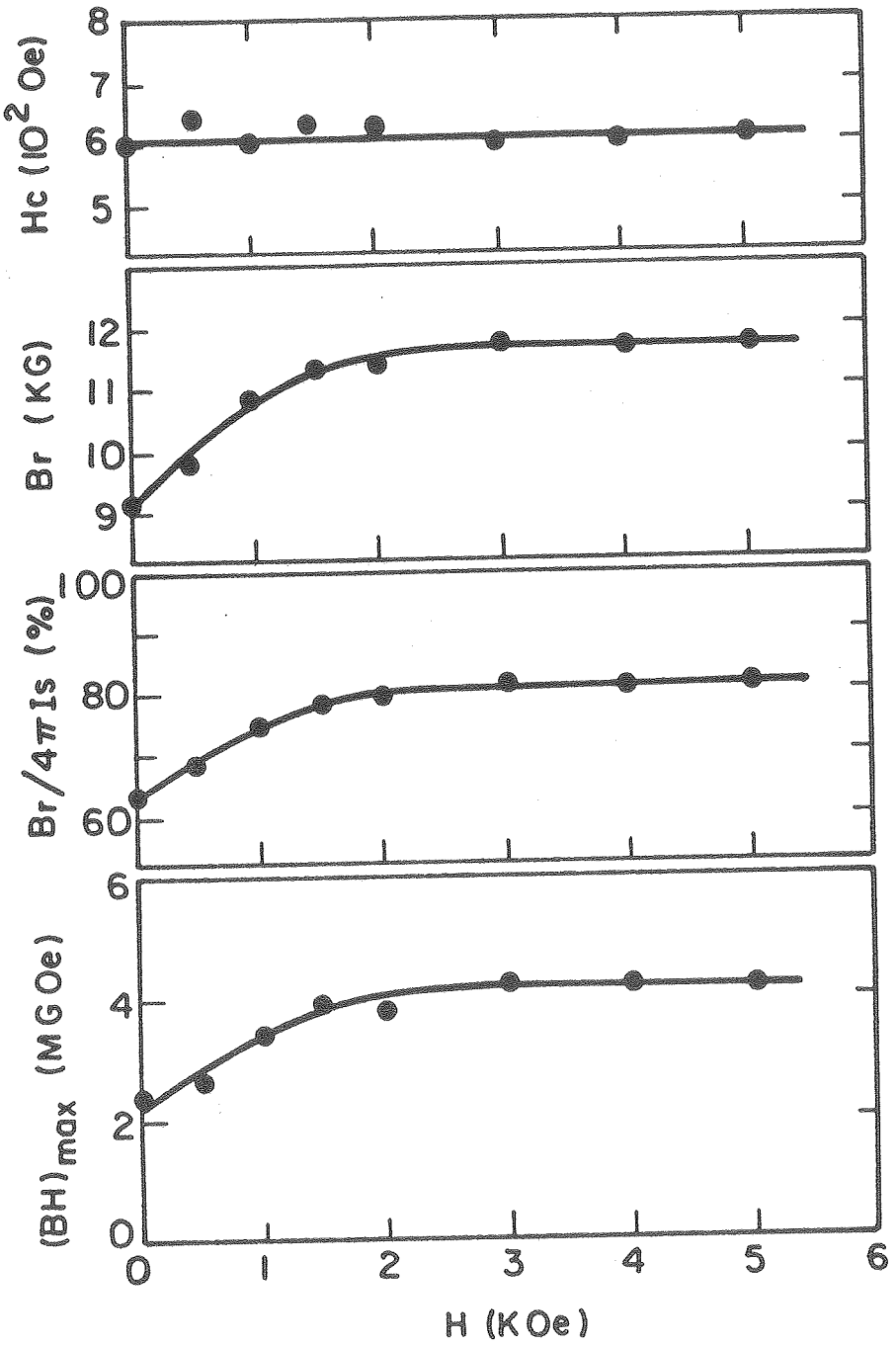
Hc (10² Oe)
8
7
6
5
Br (KG)
12
11
10
9
Br/4πIs (%)
100
80
60
(BH)max (MGOe)
6
4
2
0
0
1
2
3
4
5
6
H (KOe)
XBL784-4867

Fig. 38

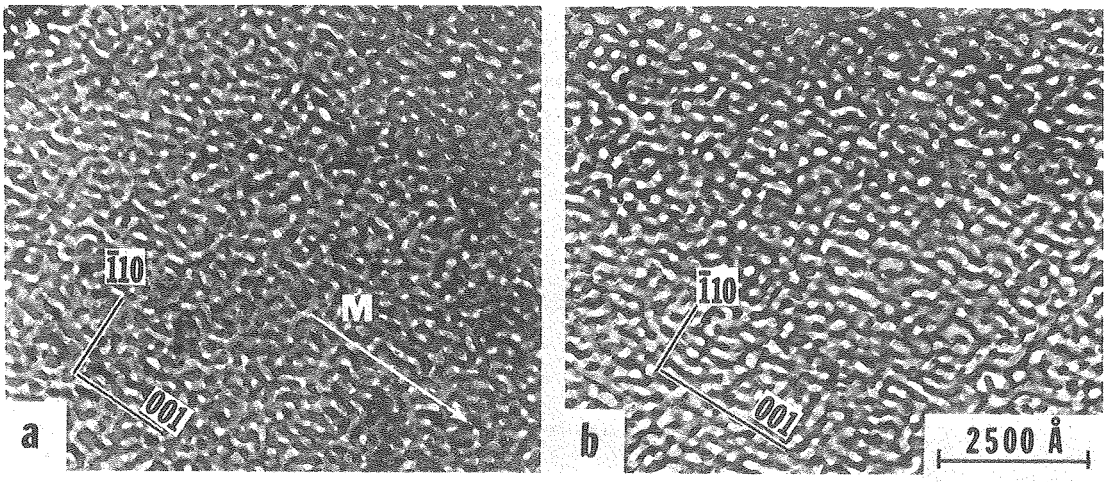

XBB 775-5210

Fig. 39

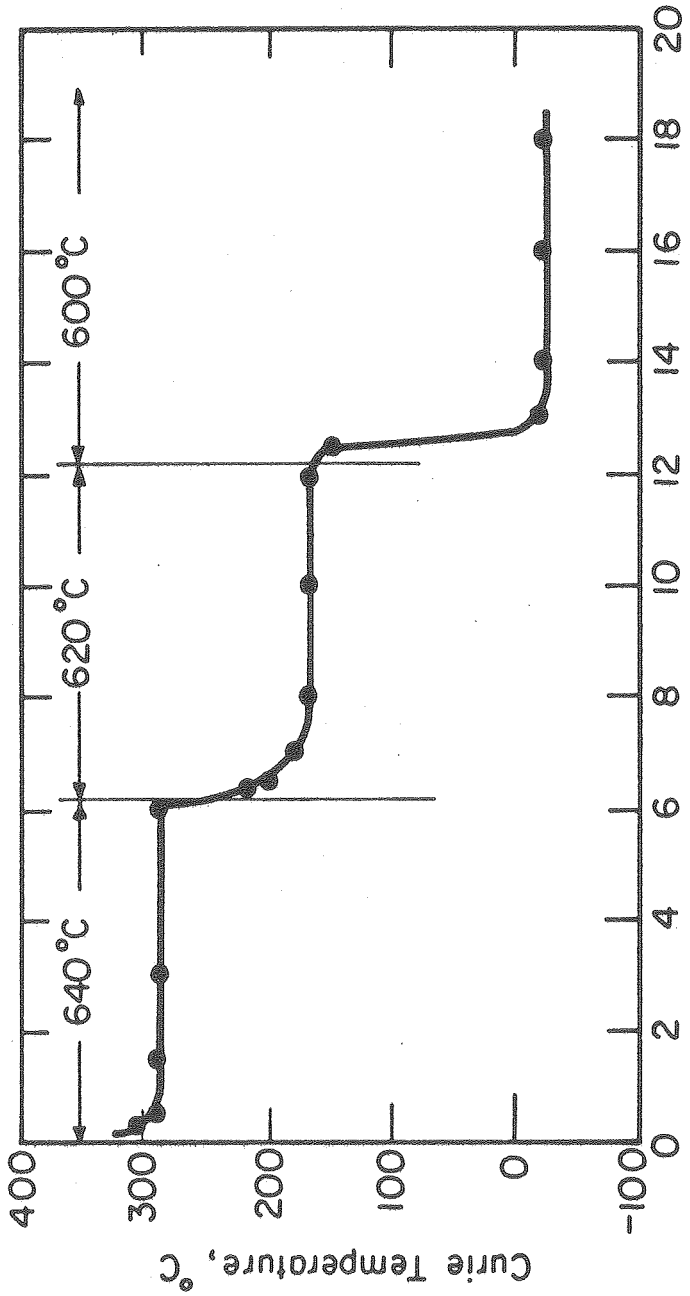

XBL 774-5376

Fig. 40

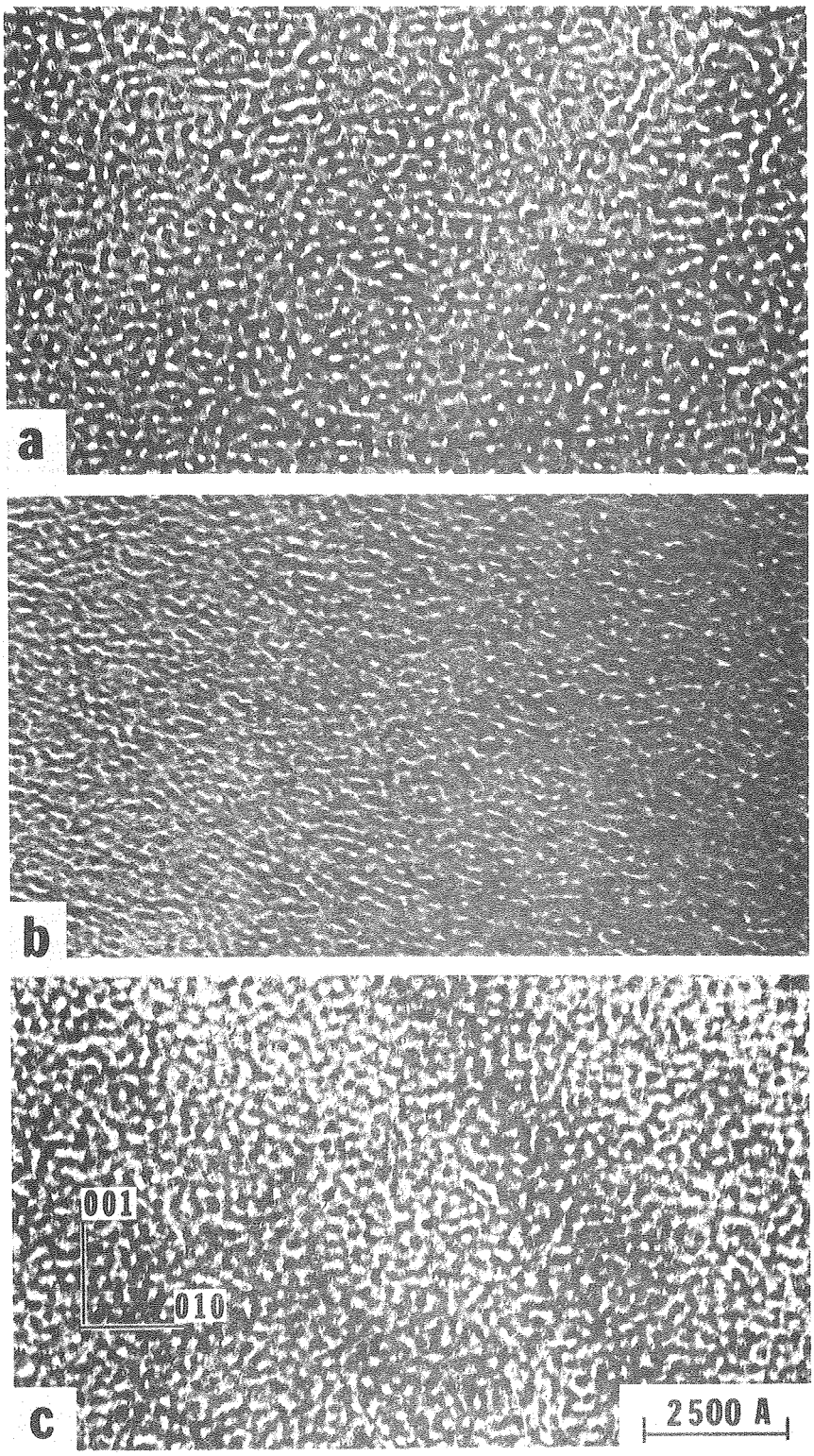

XBB 781-657

Fig. 41

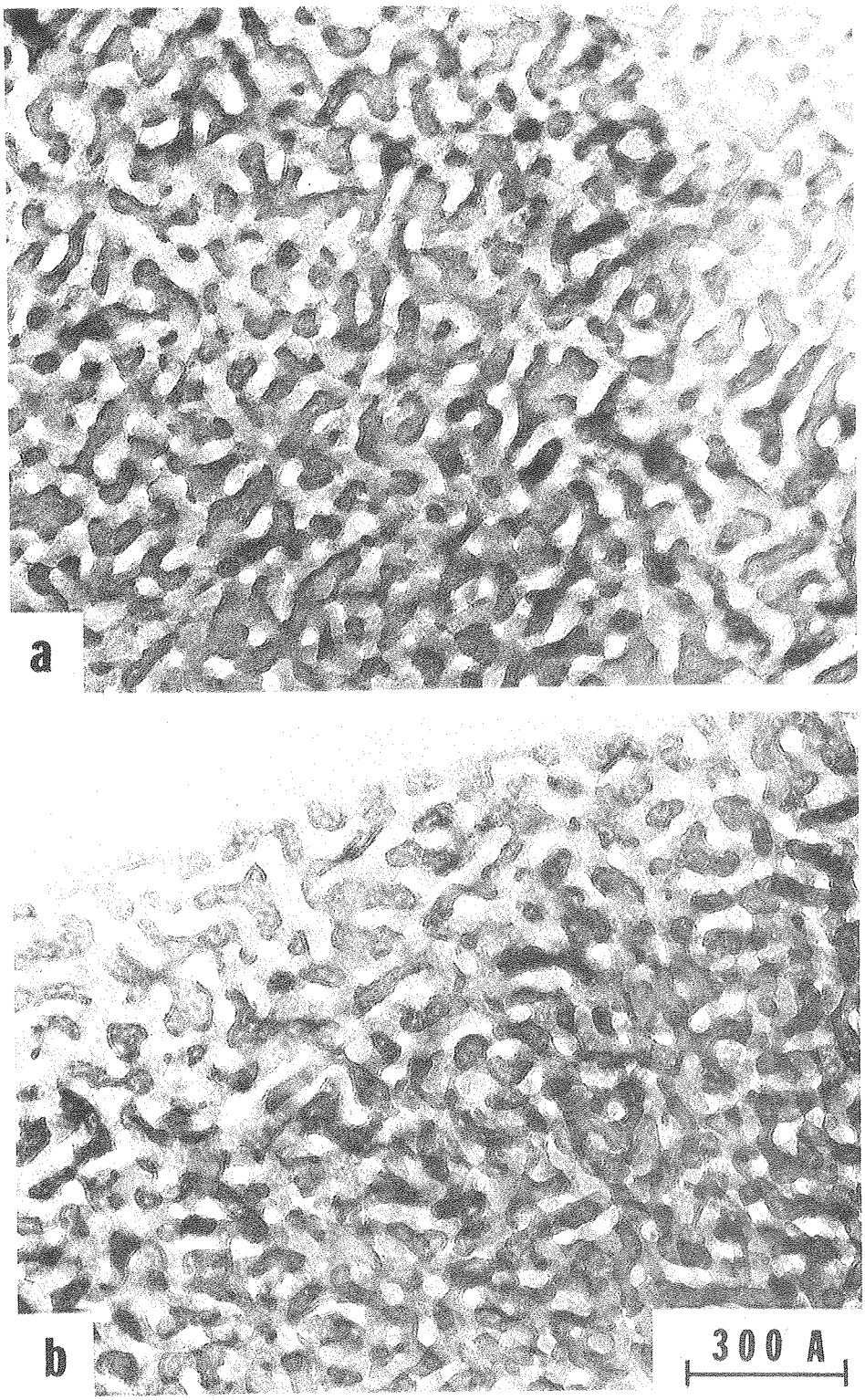

XBB 781-642

Fig. 42

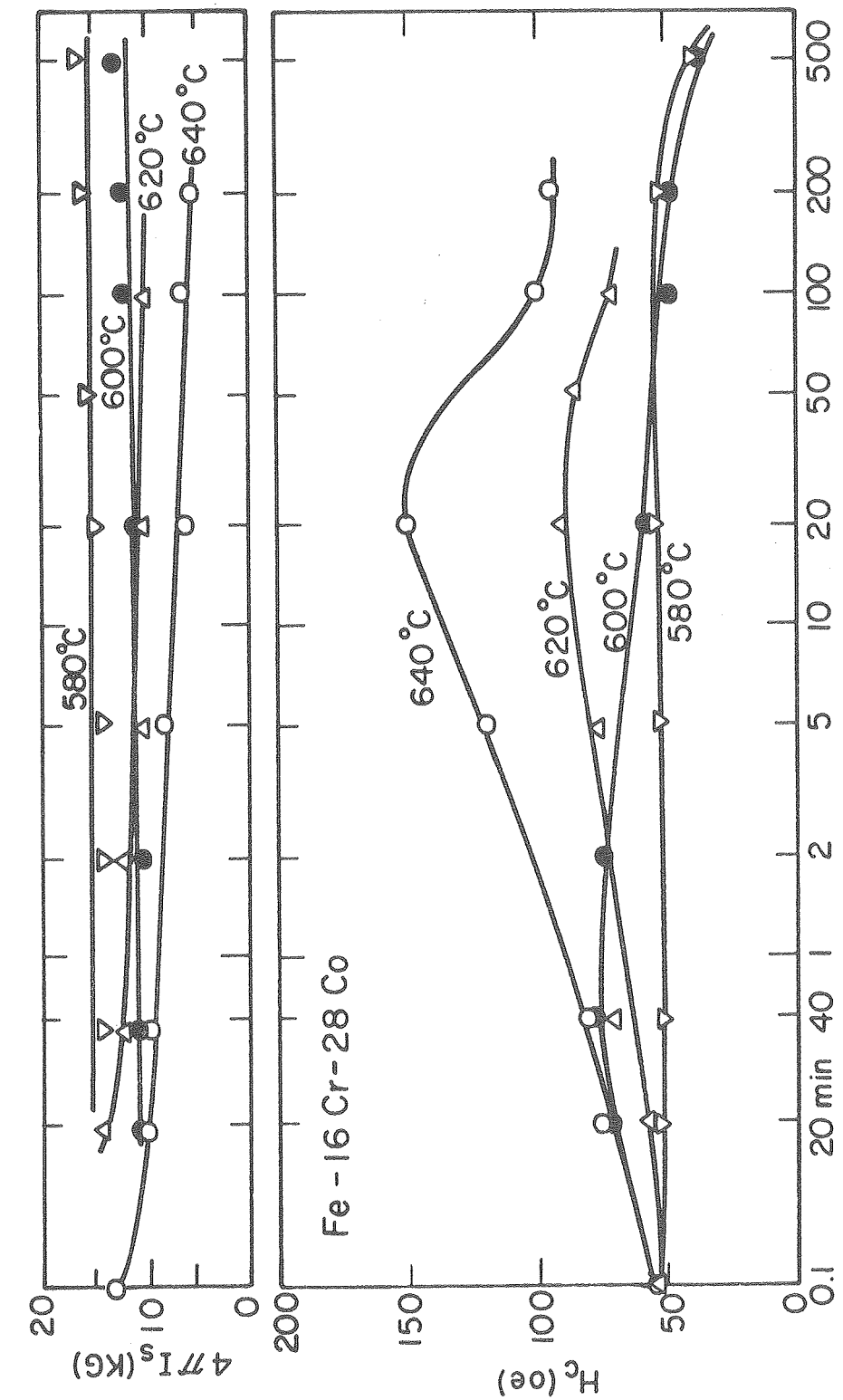

XBL7610-7642

Fig. 43

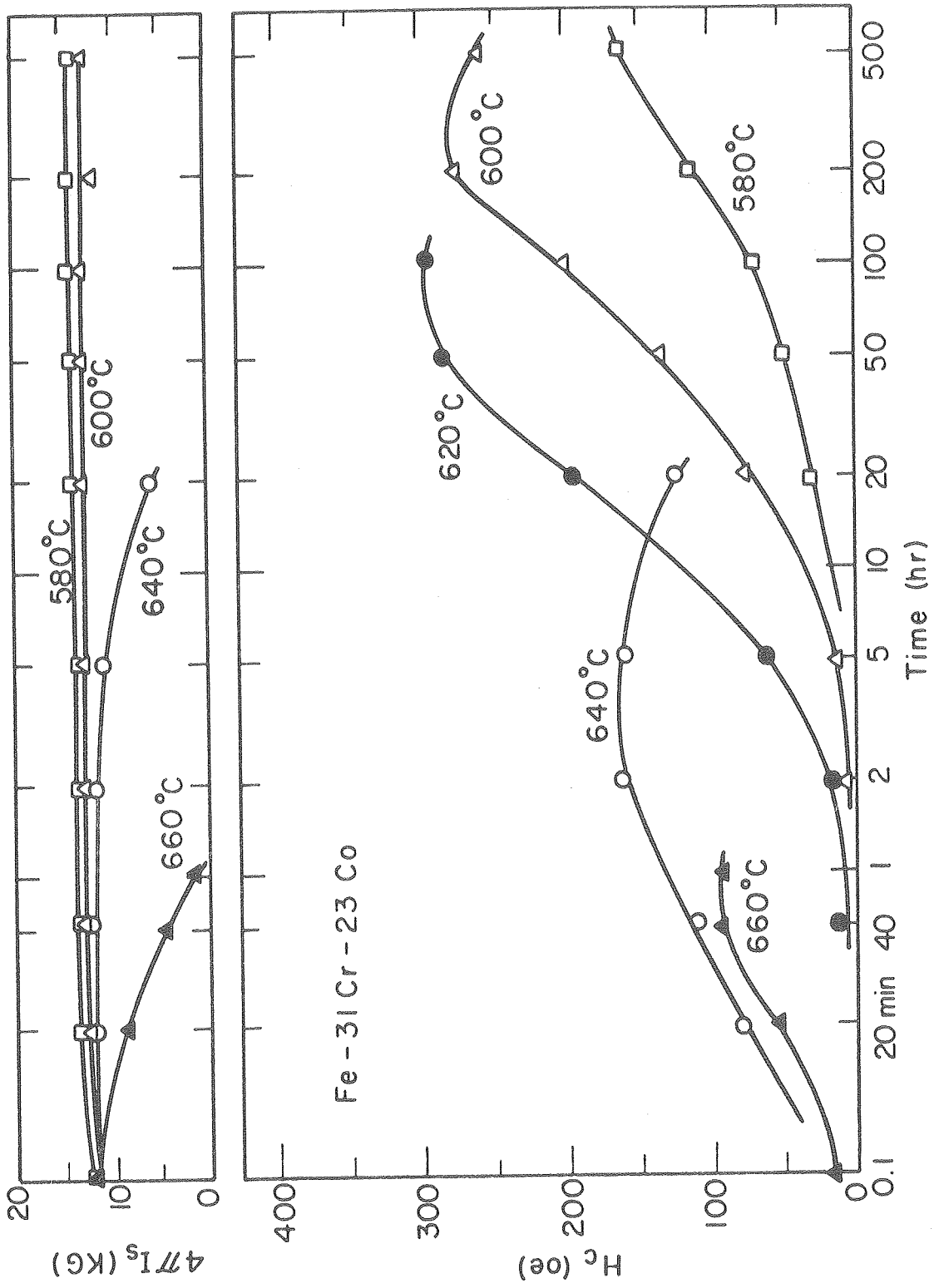

XBL 7610-7631

Fig. 44

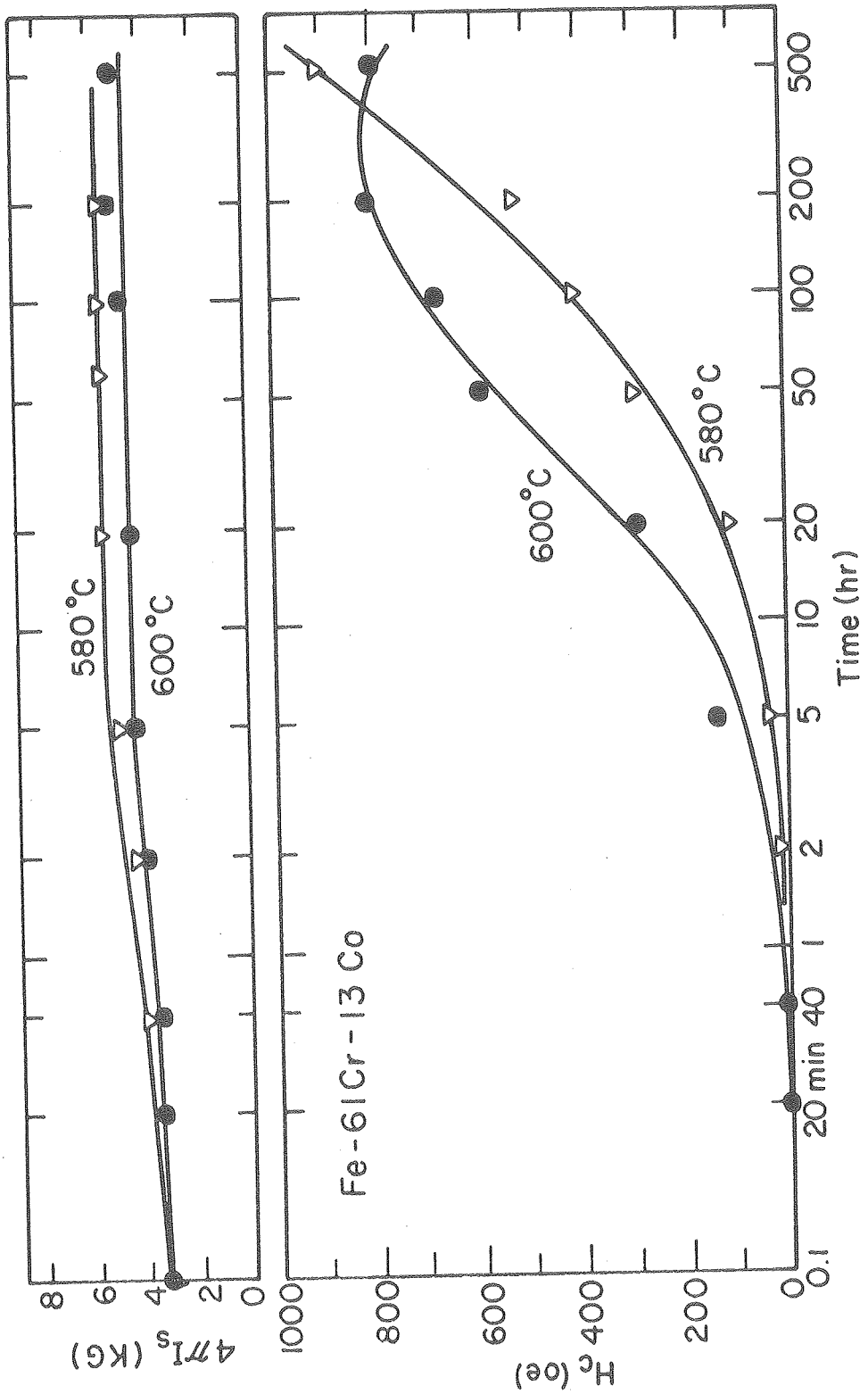

XBL 7610-7641

Fig. 45

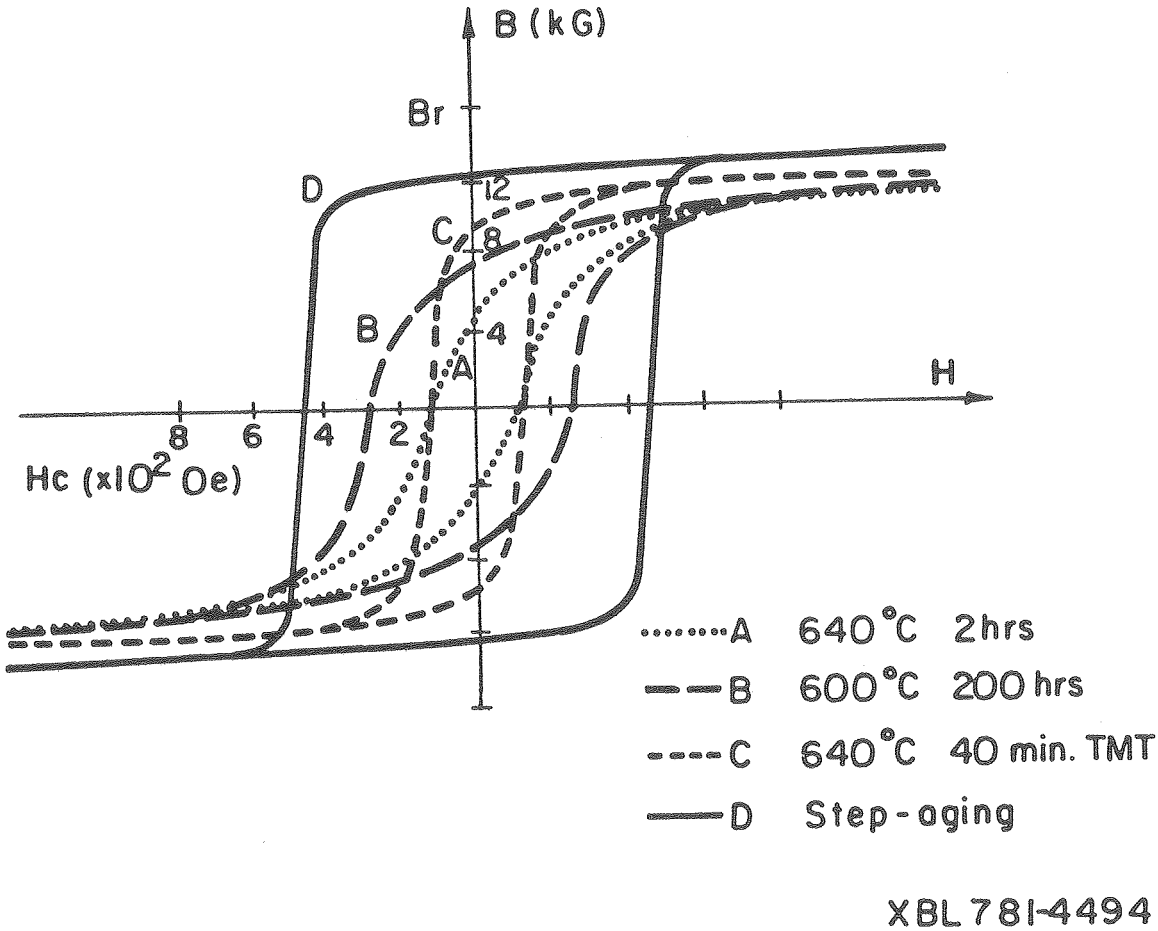
B (kG)
Br
D
C
B
A
12
8
4
H
8
6
4
2
Hc (x10² Oe)
A 640°C 2hrs
B 600°C 200 hrs
C 640°C 40 min. TMT
D Step-aging
XBL781-4494

Fig. 46

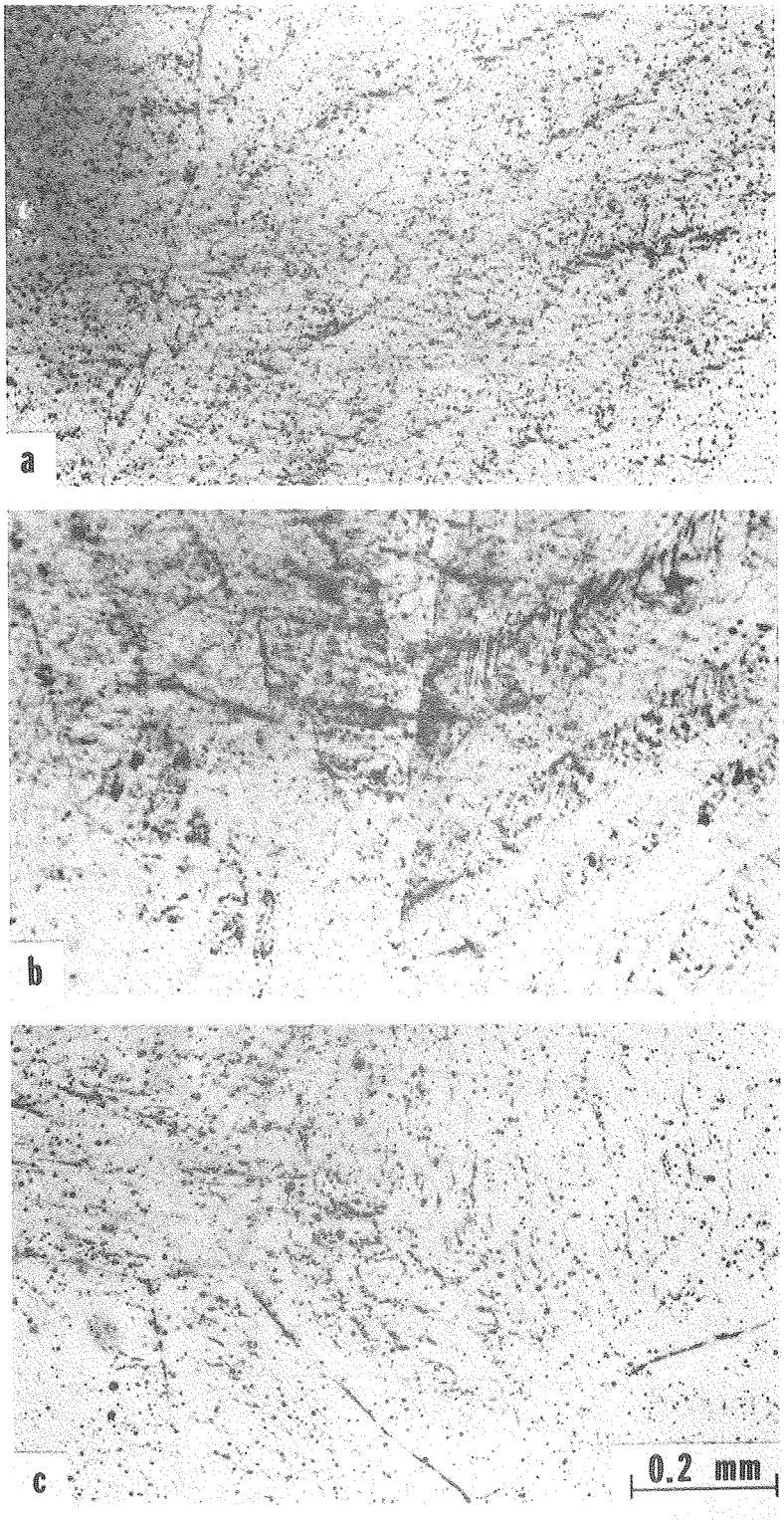

XBB 781-658

Fig. 47

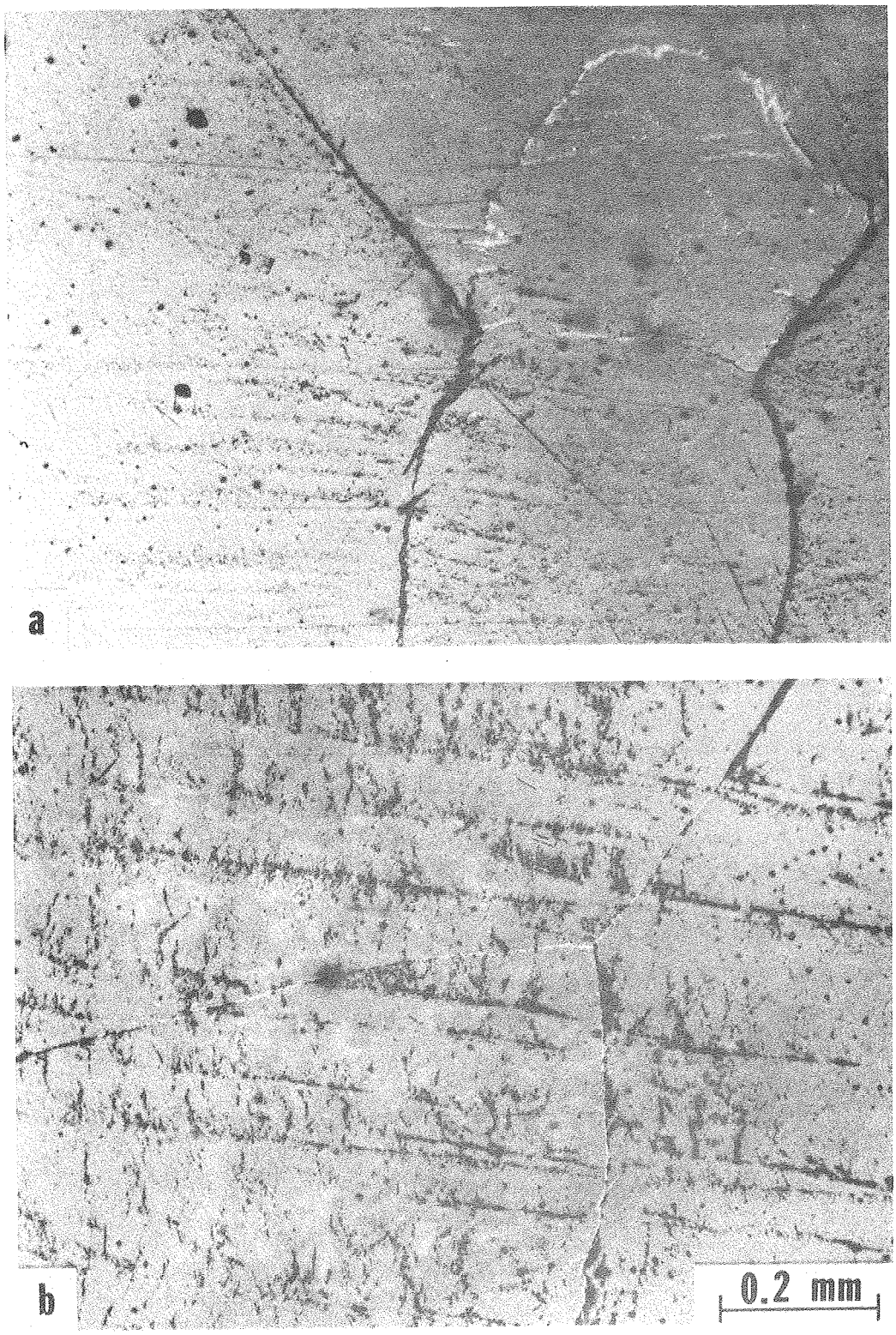

XBB 781-653

Fig. 48

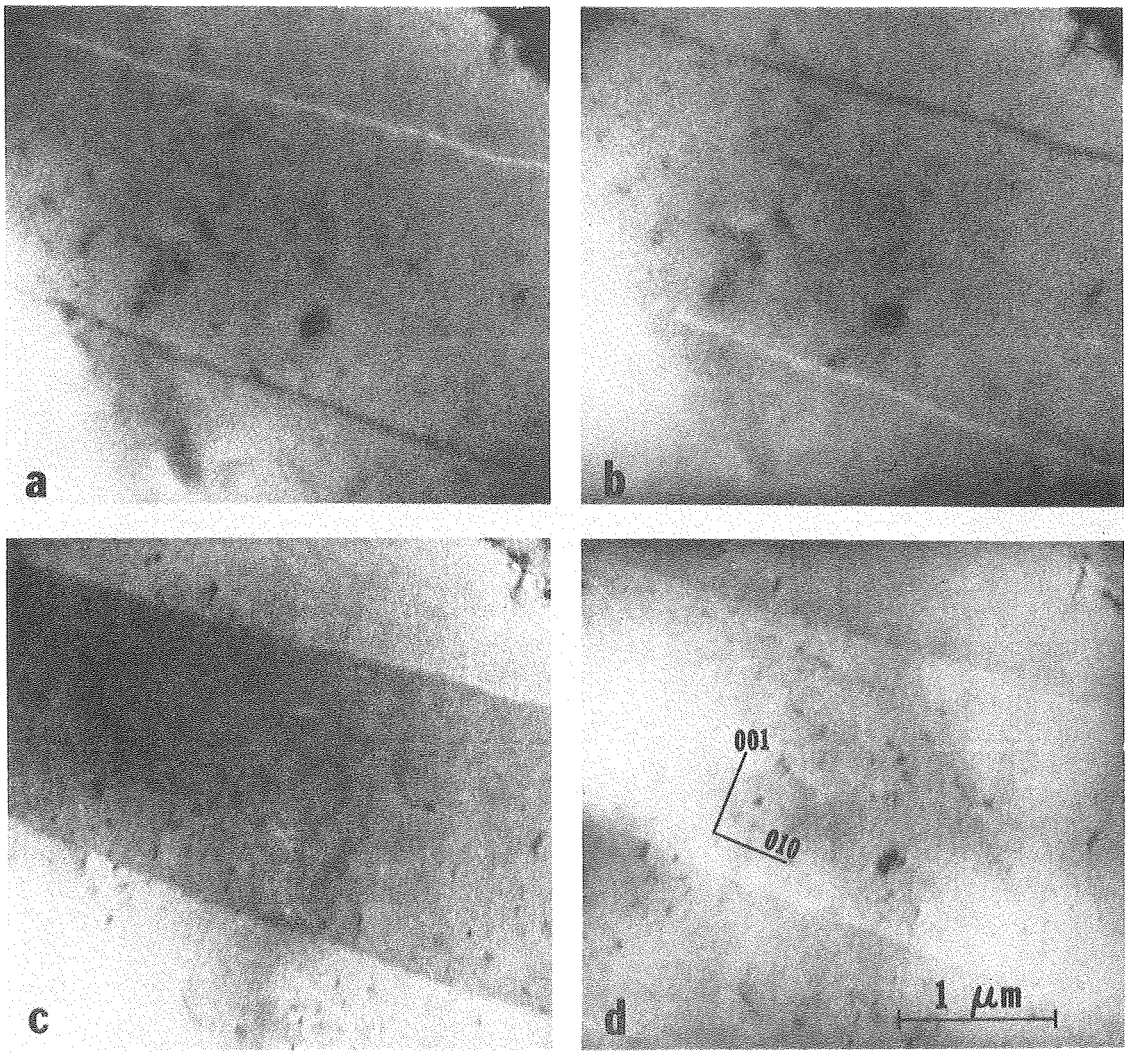

Fig. 49

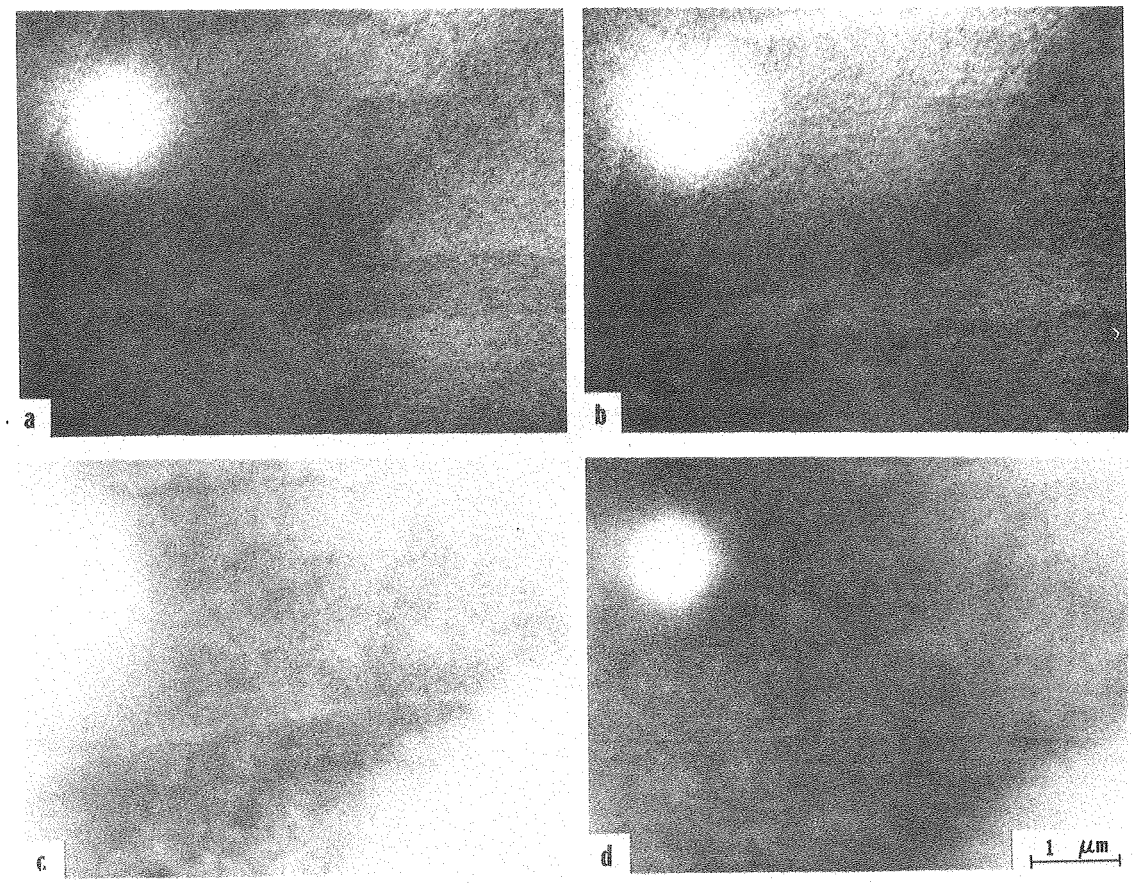

XBB 781-659

Fig. 50

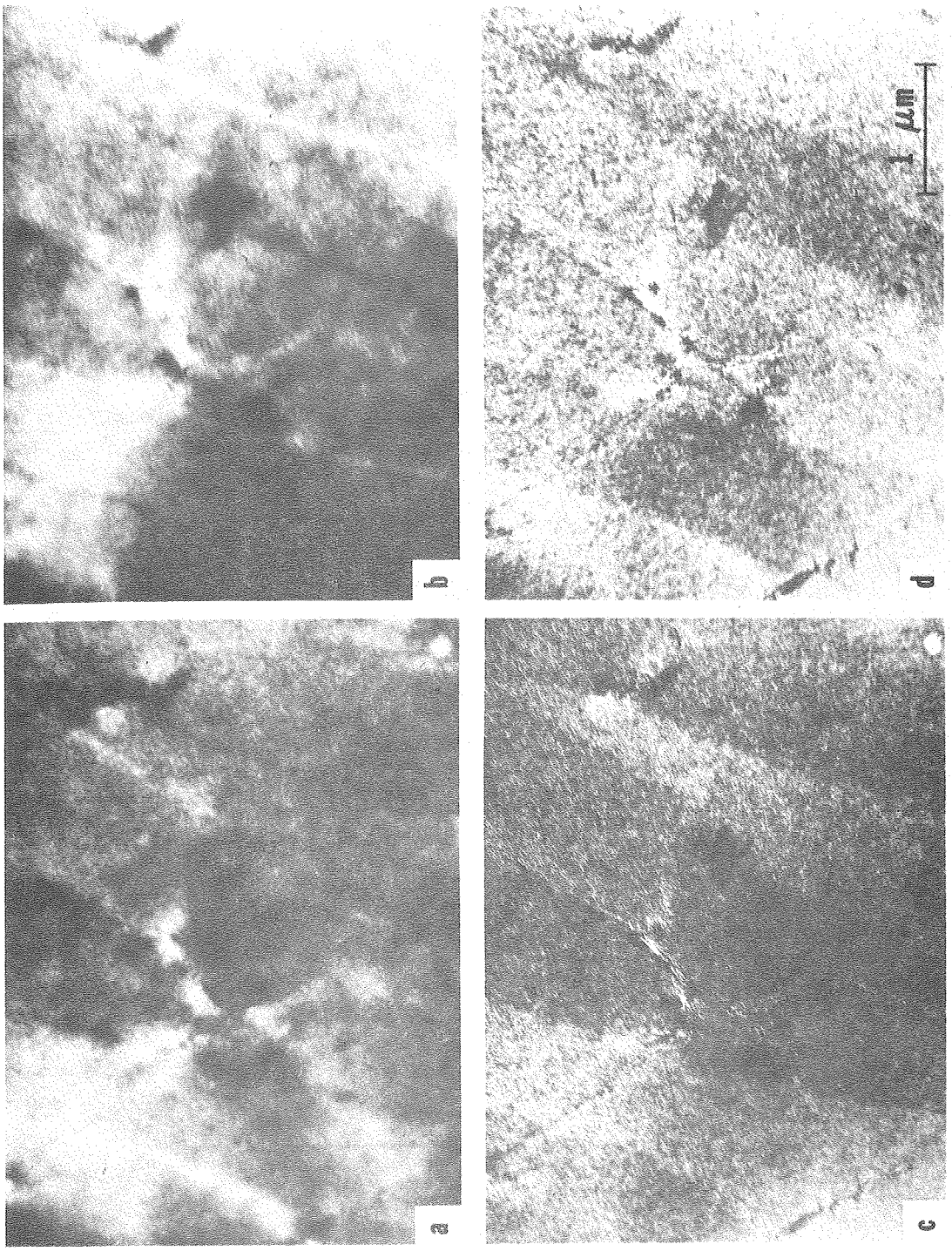

Fig. 51

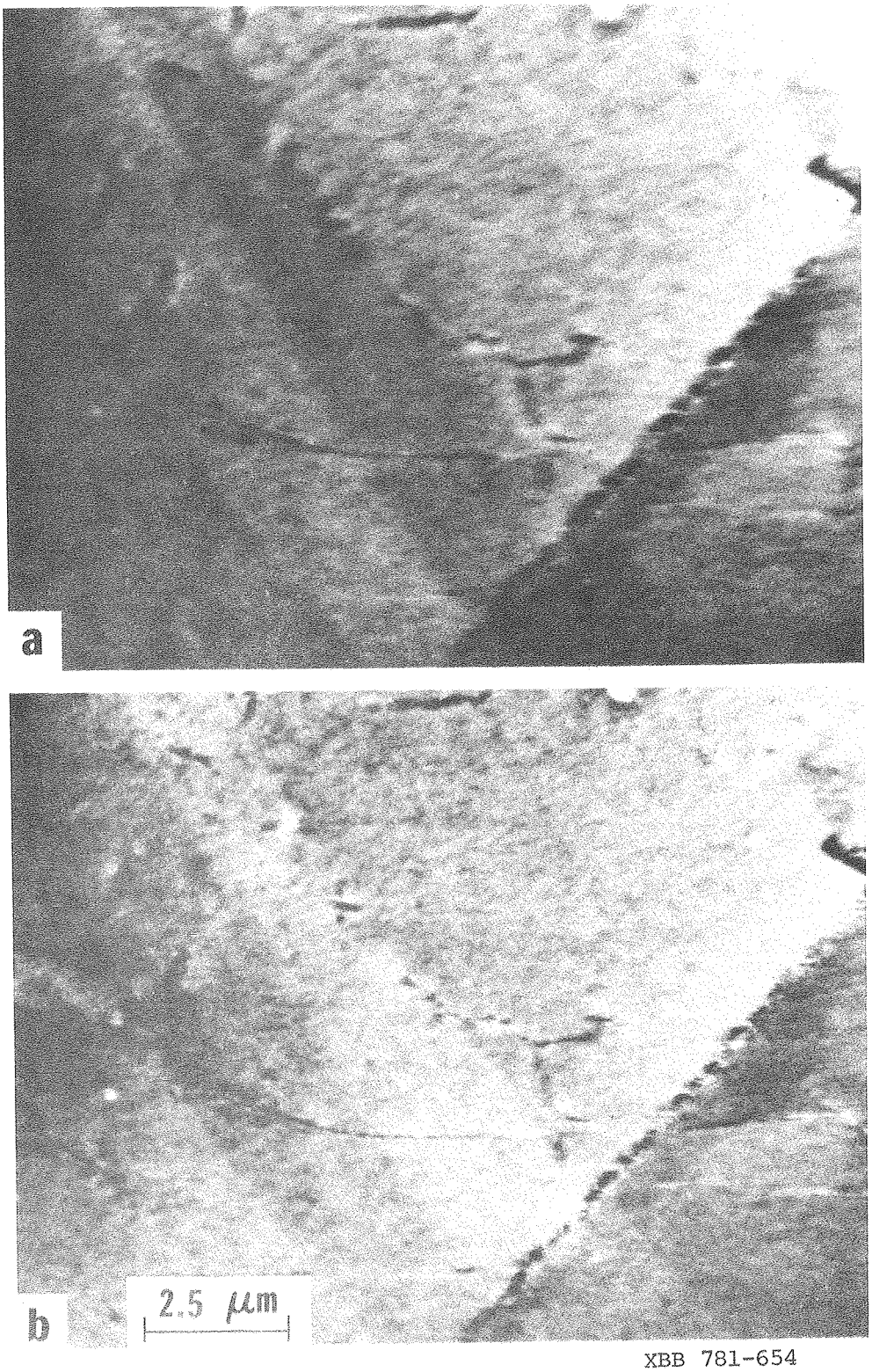

XBB 781-654

Fig. 52

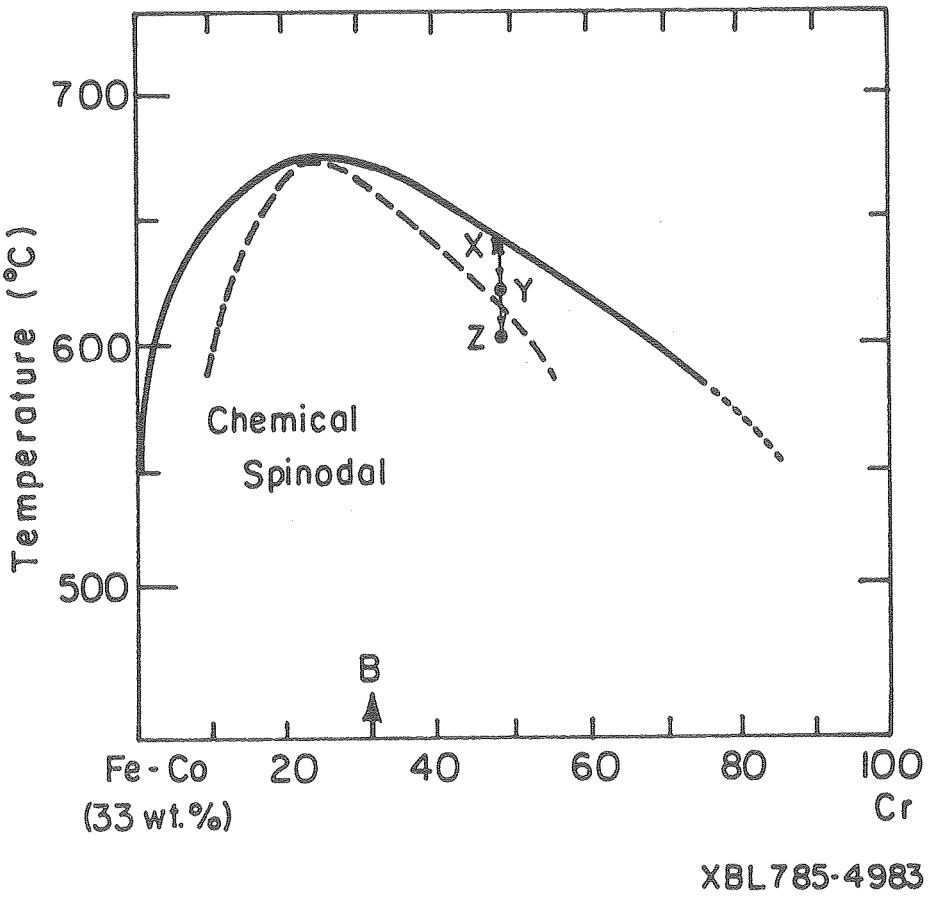
700
600
500
Temperature (°C)
X
Y
Z
Chemical
Spinodal
B
Fe-Co
(33 wt.%)
20
40
60
80
100
Cr
XBL785-4983

Fig. 53

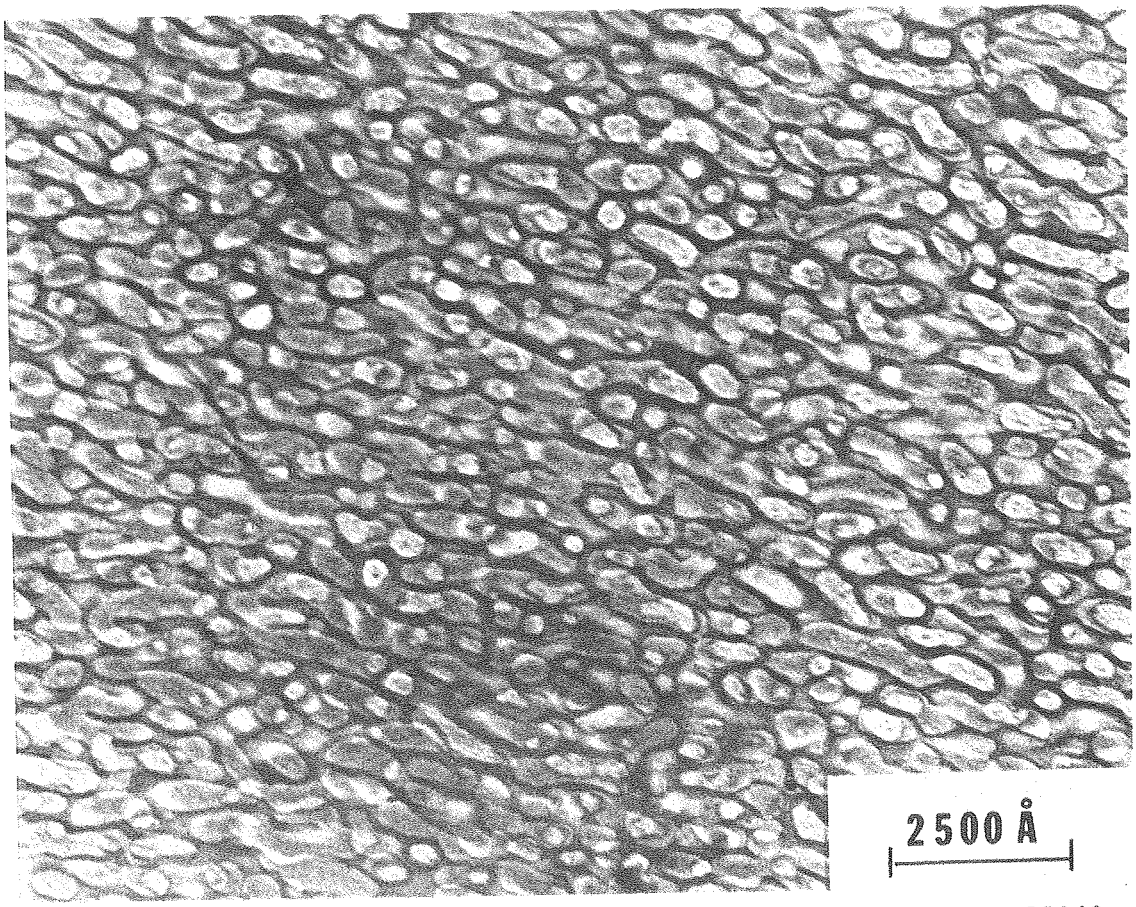

XBB 7612-11043

Fig. 54

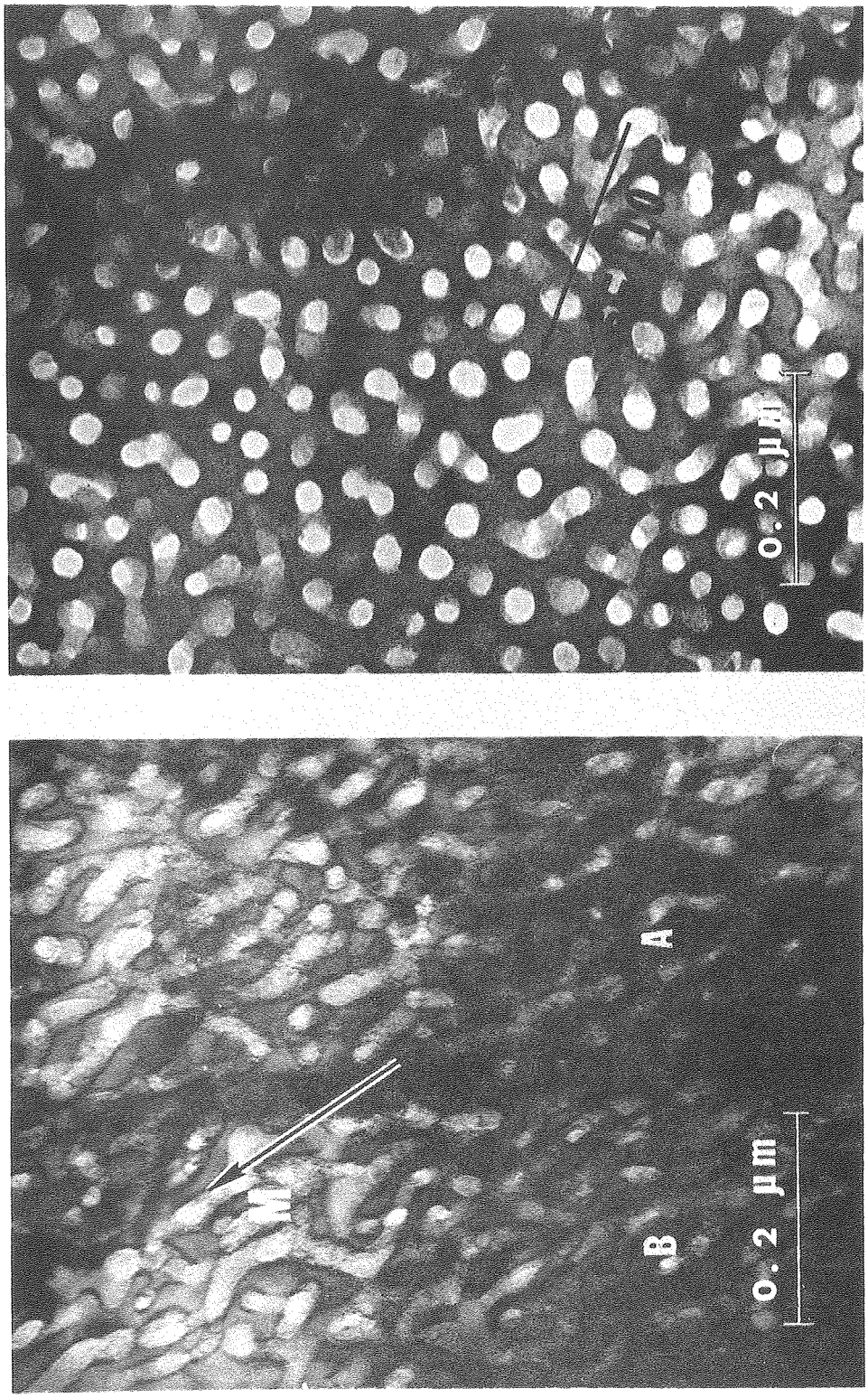

XBB 764-3253

Fig. 55

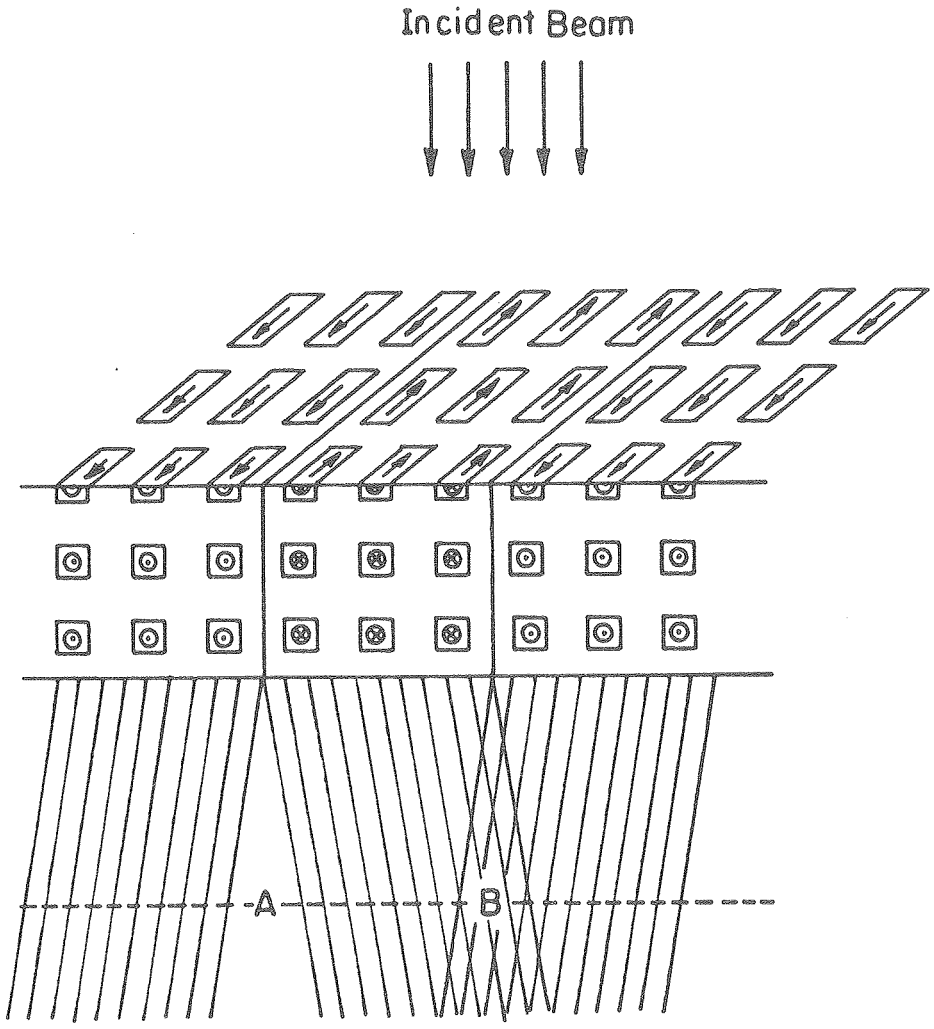

XBL 785-4985

Fig. 56

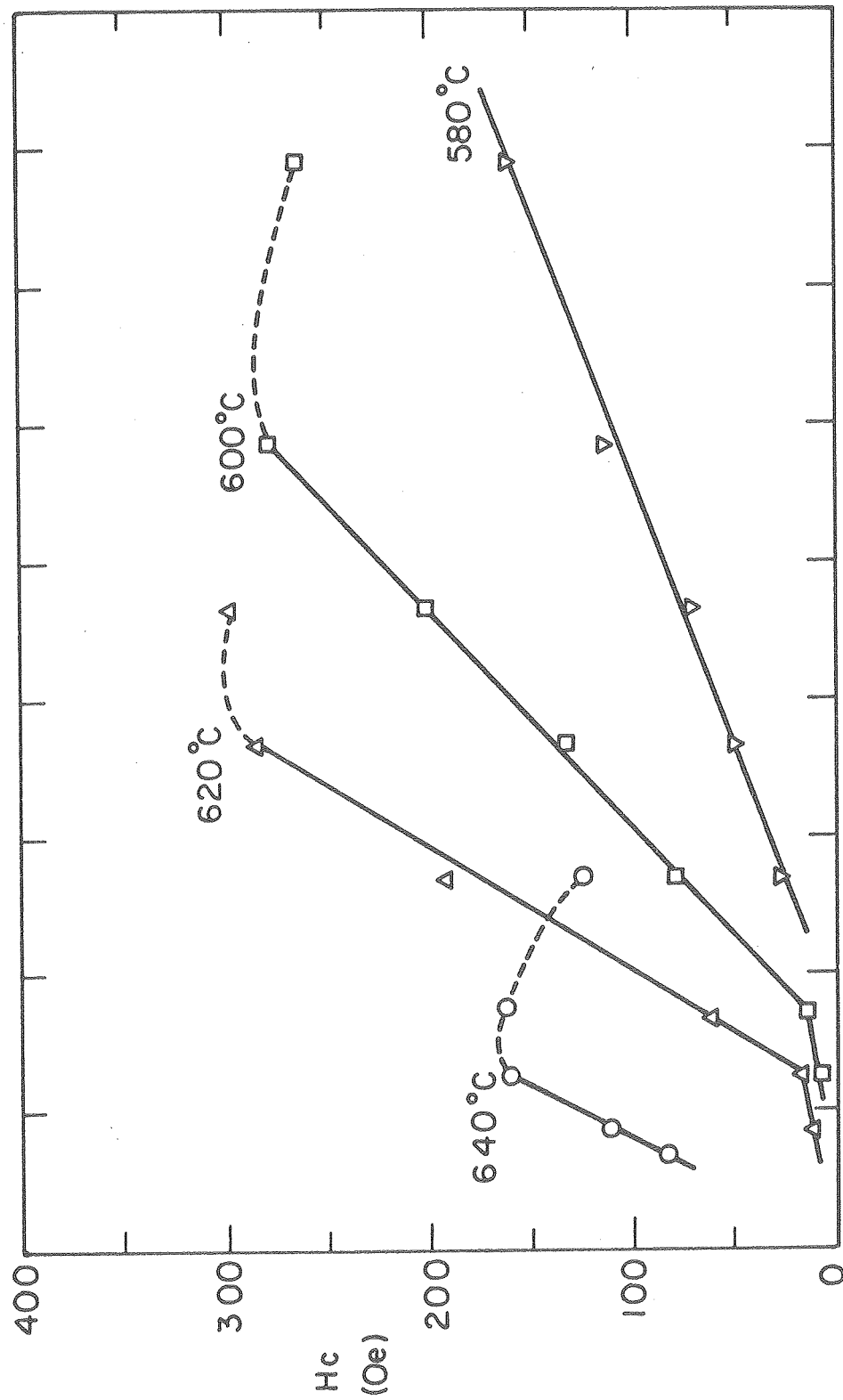

XBL 784-4866

Fig. 57

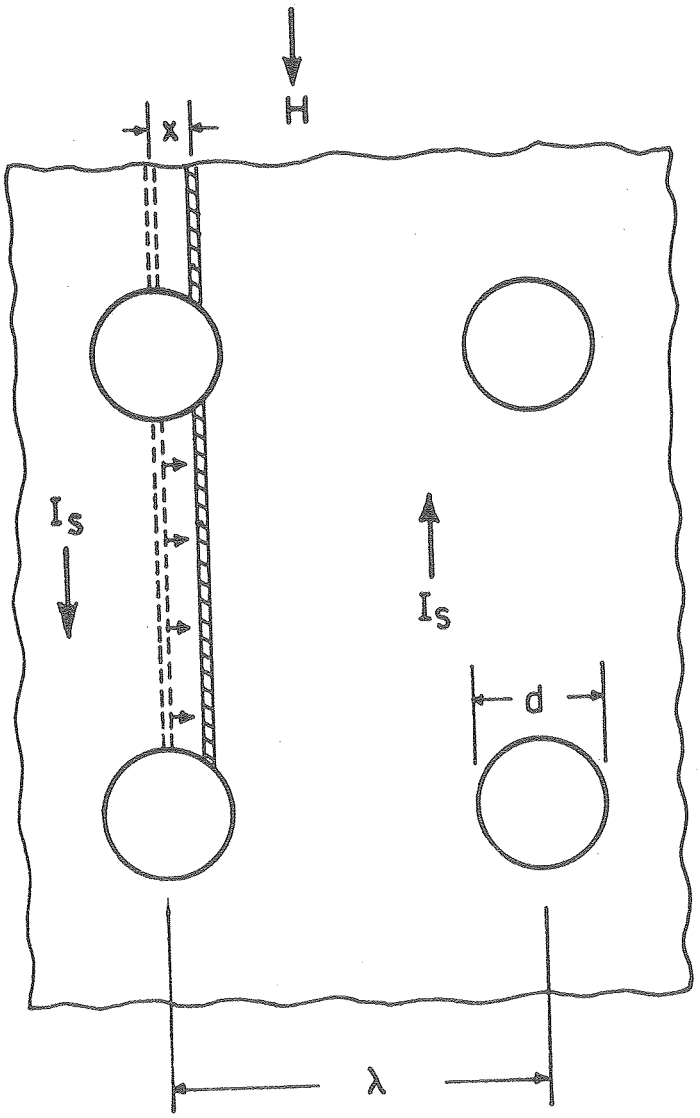

XBL 785-4987

Fig. 58

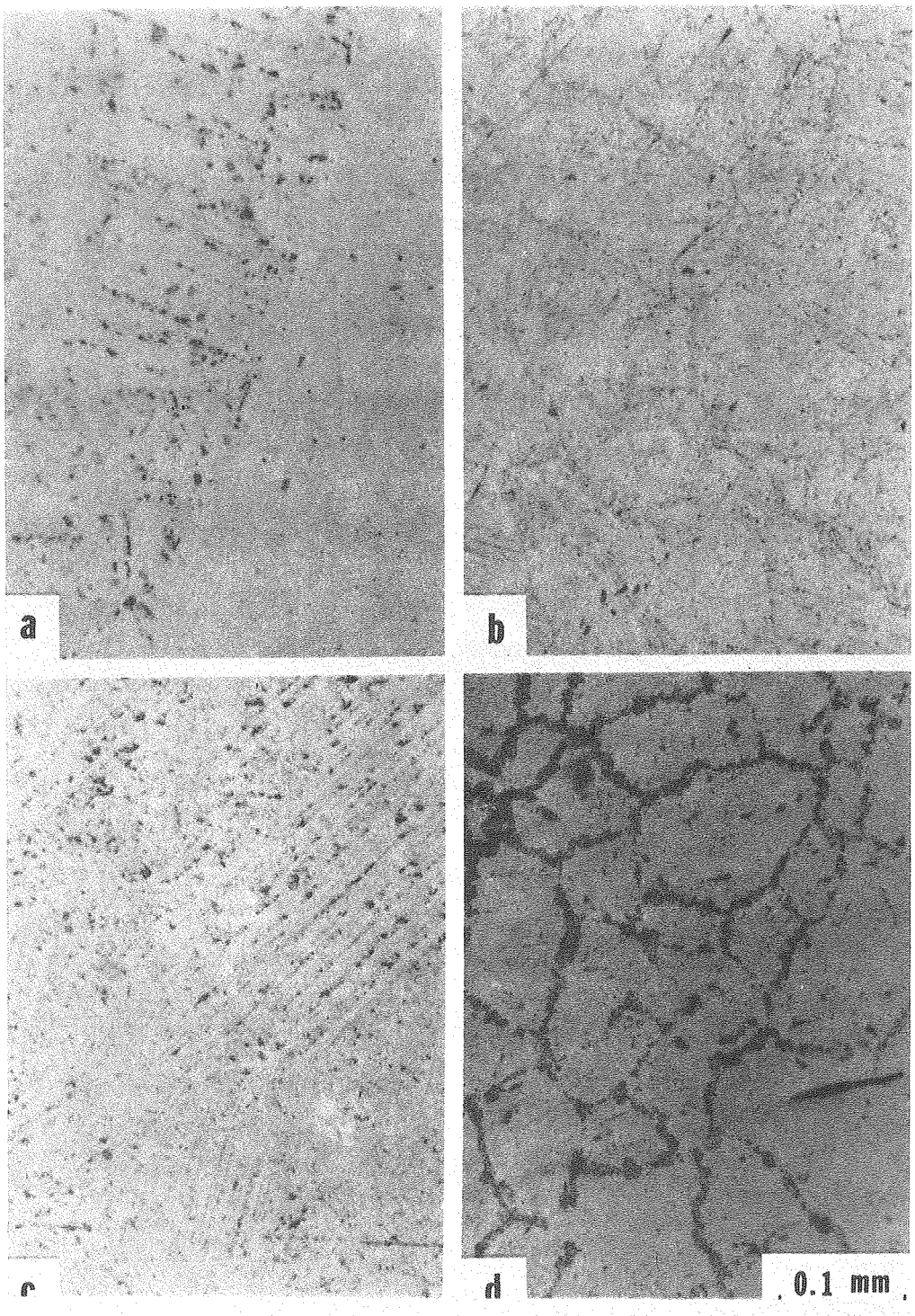

Fig. 59

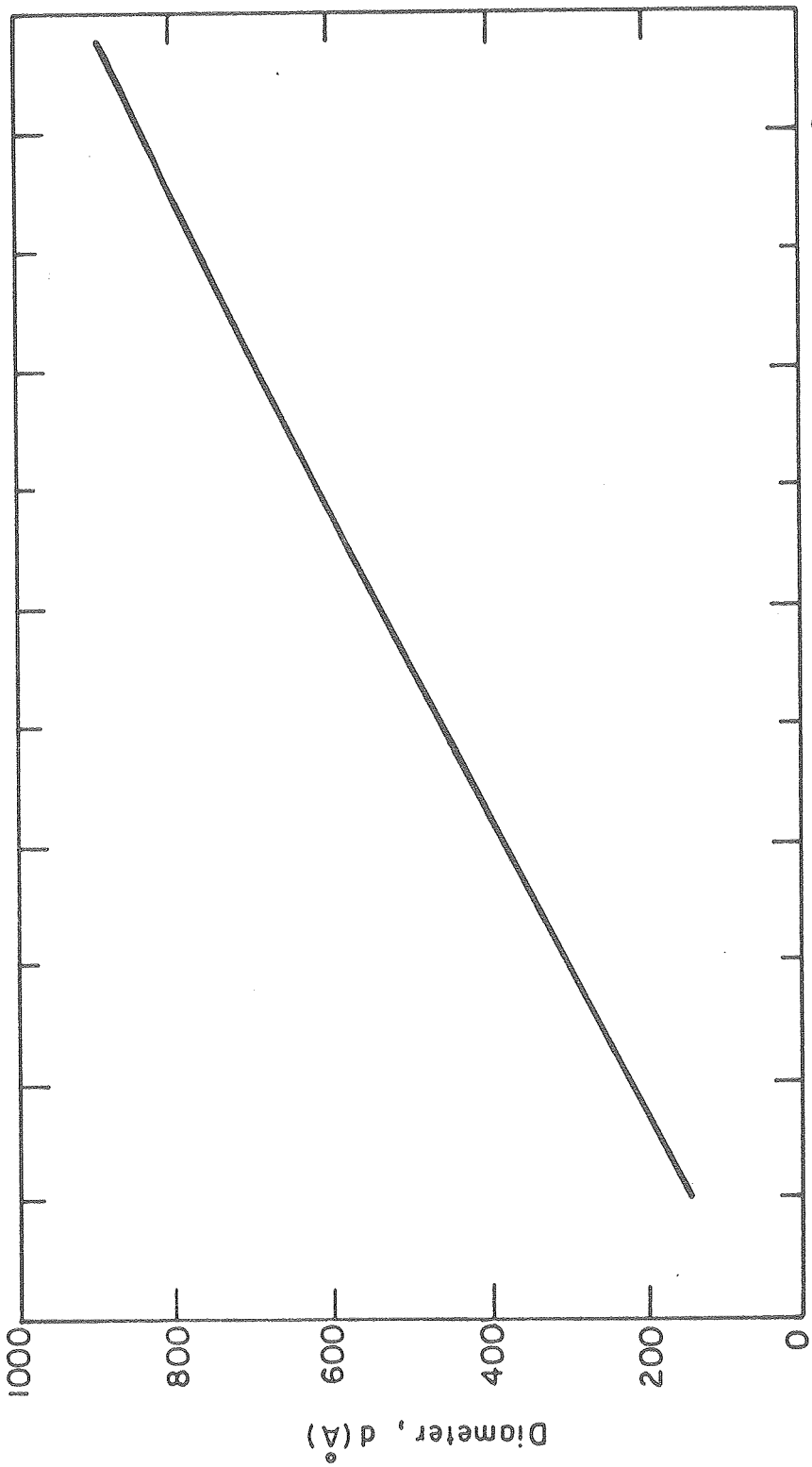

XBL785-4989

Fig. 60

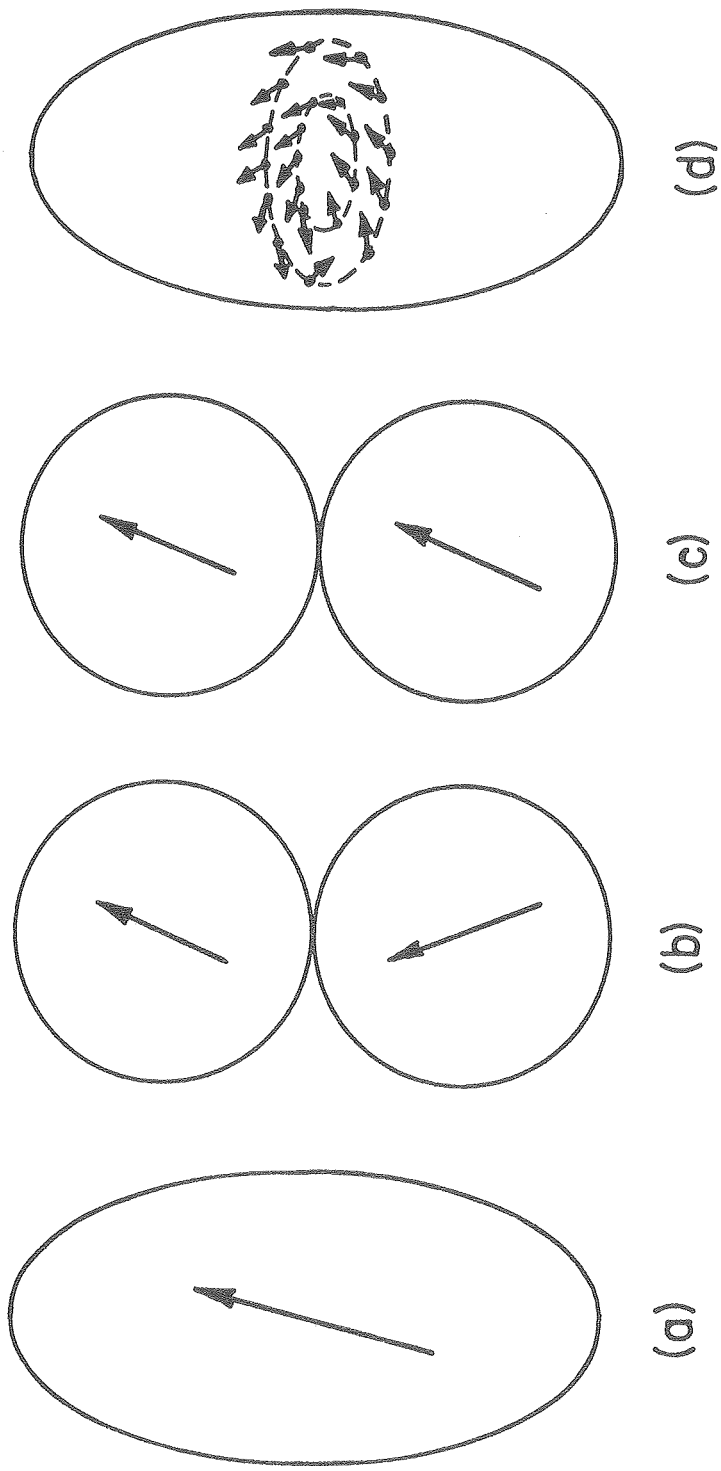

XBL785-4982

Fig. 61

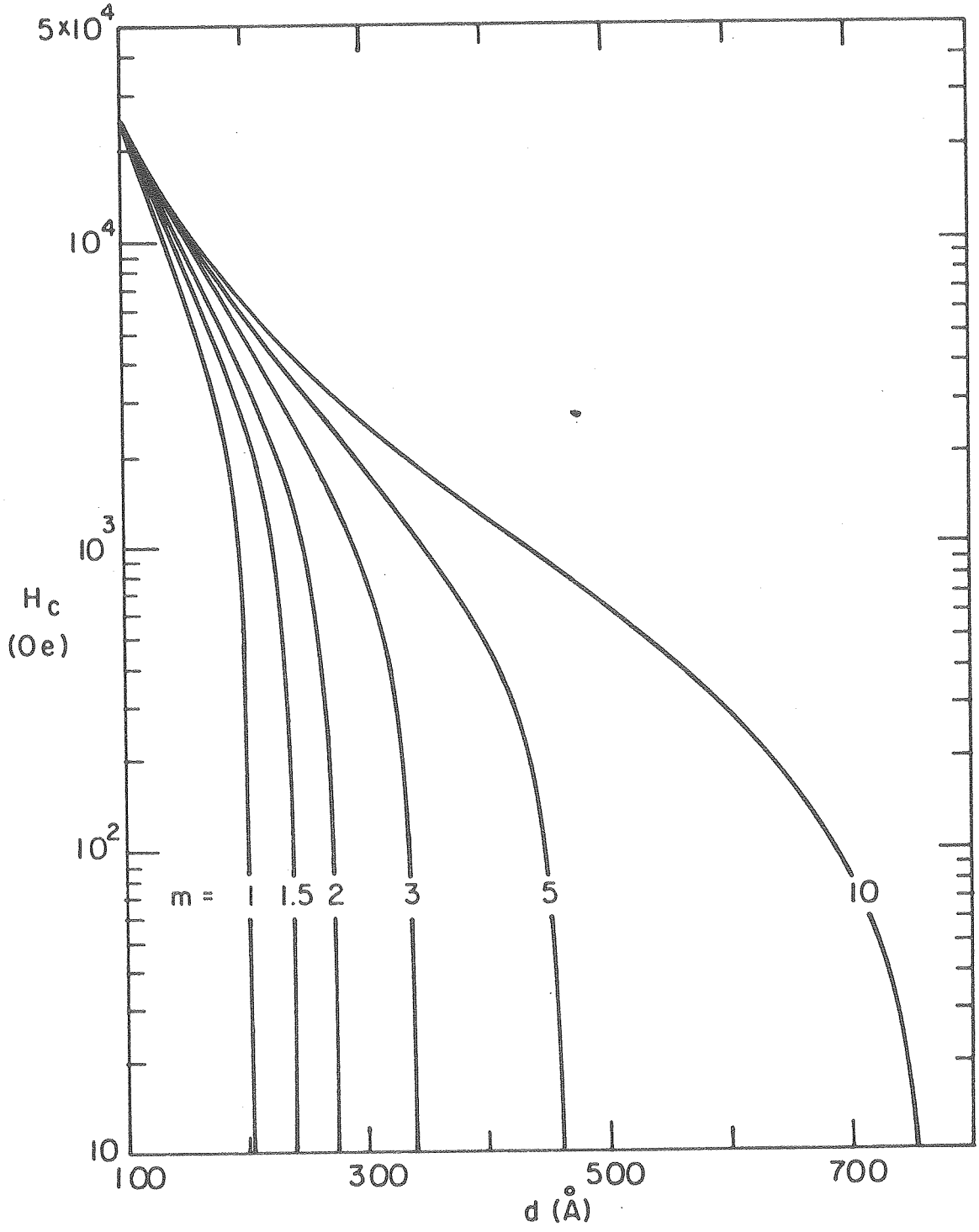
5x10^4
10^4
10^3
10^2
10
Hc
(Oe)
m = 1 1.5 2 3 5 10
100
300
500
700
d (Å)
XBL 785-4988

Fig. 62

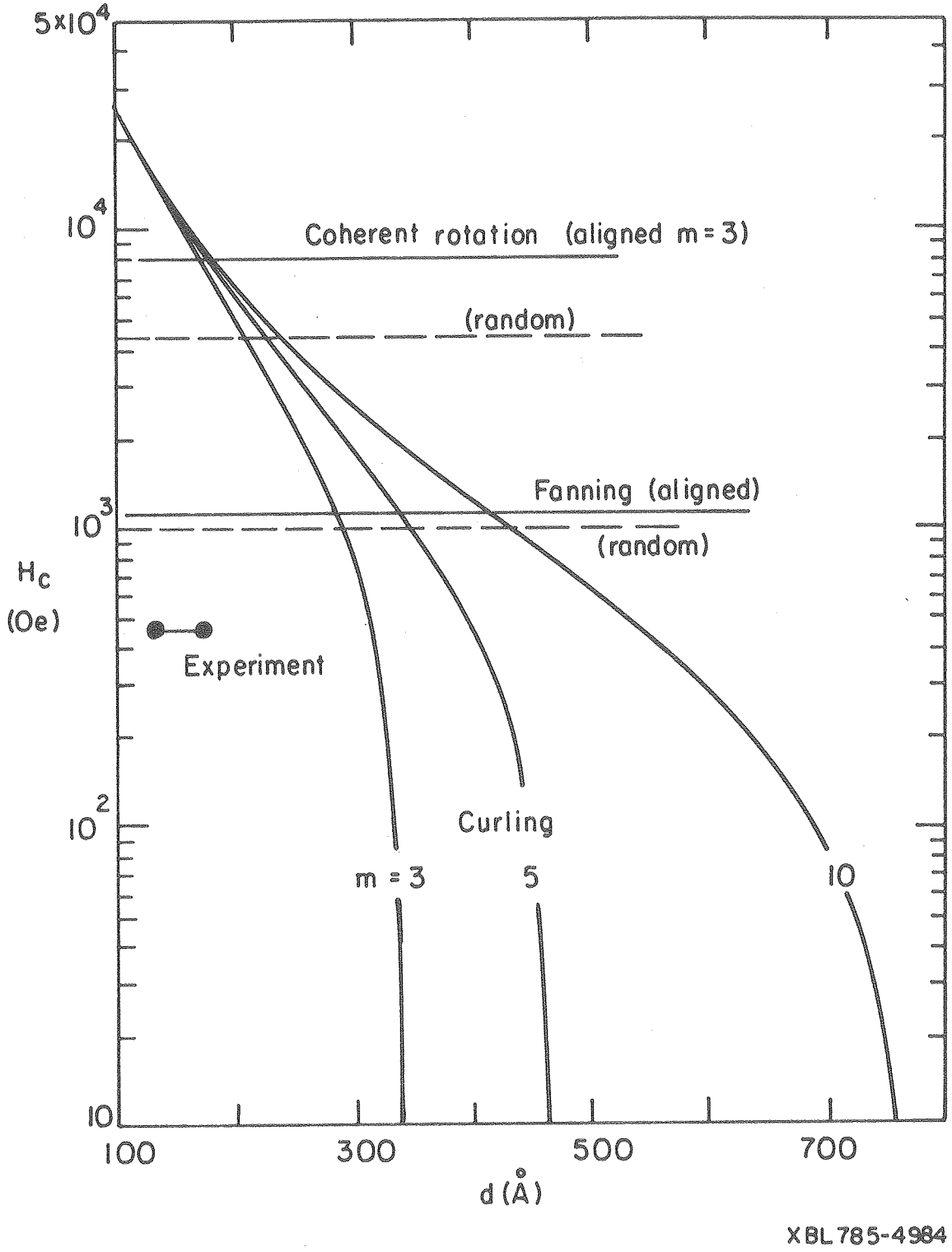
5x10^4
10^4
10^3
10^2
10
Coherent rotation (aligned m=3)
(random)
Fanning (aligned)
(random)
Hc
(Oe)
Experiment
Curling
m = 3
5
10
100
300
500
700
d (Å)
XBL785-4984

Fig. 63

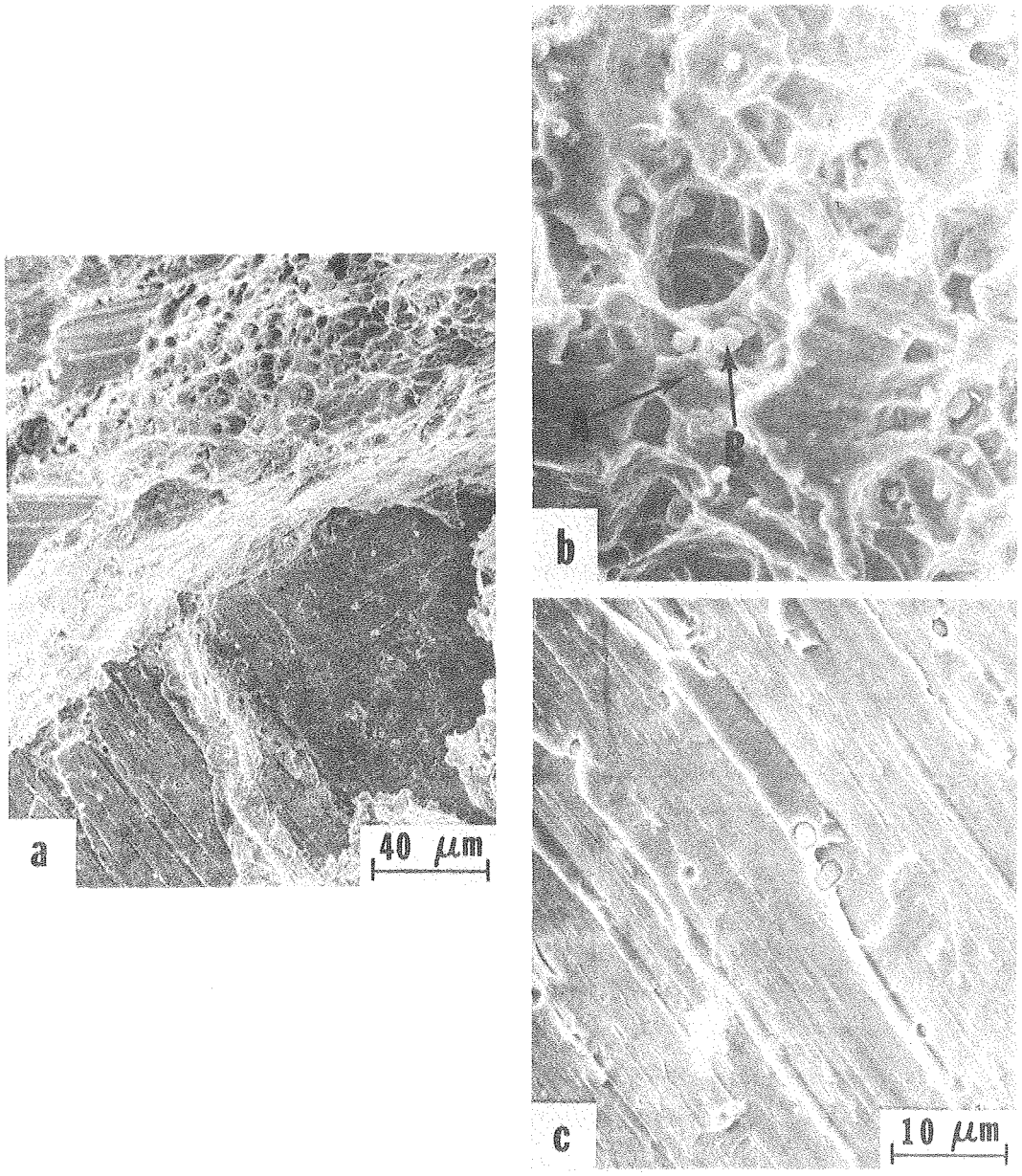

XBB 781-649

Fig. 64

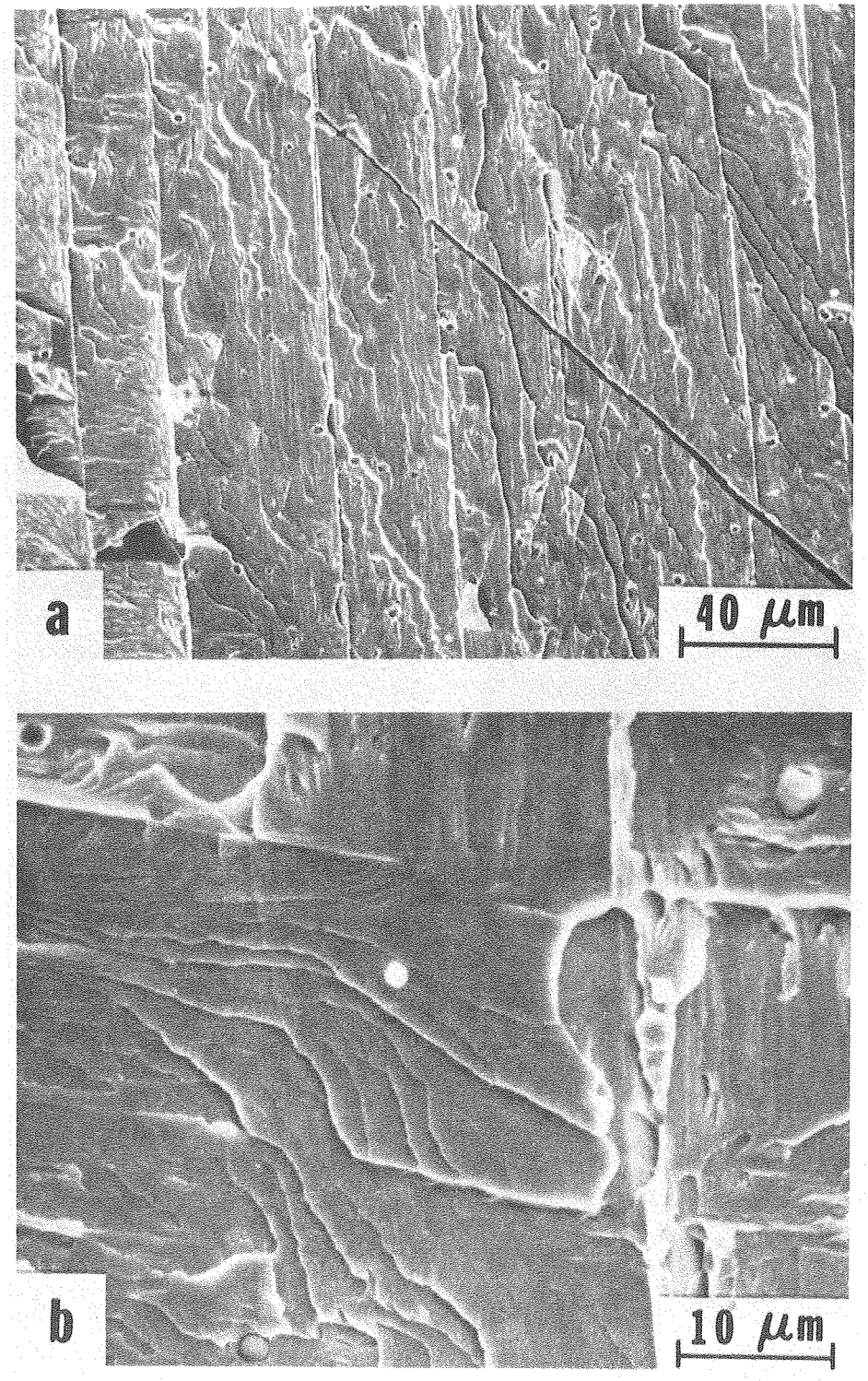

XBB 781-647

Fig. 65